Finite Element Modelling of Linear Friction Welded high strength steel chains

Pedro Santos da Graça Effertz, M.Sc.

DOCTORAL THESIS

to achieve the university degree of

Doctor of Technical Sciences

submitted to

Graz University of Technology

Supervisor:

Assoc. Prof. Dipl.-Ing. Dr. techn. Norbert Enzinger

Institute of Material Science, Joining and Forming - IMAT

Graz, February of 2019

Affidavit

I declare that I have authored this thesis independently, that I have not used other than the declared sources/resources, and that I have explicitly indicated all material which has been quoted either literally or by content from the sources used. The text document uploaded to TUGRAZonline is identical to the present doctoral thesis.

Date	Signature

Acknowledgements

My academic journey at the Technical University of Graz has been very stimulating and enriching. I would like to express my sincere acknowledgements to everyone whose input has proved invaluable in my endeavour. I begin by thanking my thesis advisor, Prof. Dr. Norbert Enzinger, without whose guidance and encouragement this work would not have been possible. Due to the incomparable knowledge and experience he has in bonding technology and processes, and kindly transmitted to me. Discussions always proved to be very educative and therefore I am grateful to him.

I would also like to thank to Prof. Dr. Christof Sommitsch for the thoughtful and insightful suggestions which have been very helpful in my research. I thank him for giving the opportunity of developing my work in the Institute for Materials Science and Welding (IMAT) in the TU Graz, and providing me all necessary tools to ensure the success of this research.

I express my sincere thanks to Dipl.-Ing. Franz Fuchs from pewag Engineering GmbH and intervening project partners from voestalpine Wire Rod Austria GmbH, for the incomparable knowledge transmitted regarding linear friction welding of chains and the follow-up he gave me throughout the development of this thesis.

To my colleagues and friends from the "Steyeregasse" my sincere acknowledgements for the important contributions in my work during my stay in the TU Graz. I owe them dept for their fruitful discussions and help, technical and otherwise. They were indispensable in making my academic journey very enjoyable being patient and accompanying me in all stages of this work. Moreover, to all unmentioned staff and colleagues from IMAT that somehow contributed to the developed work I would like to express my acknowledgements.

I am very thankful to Prof. Dr. Luísa Coutinho for the indispensable advice, support and friendship. She has instilled in me the motivation and confidence necessary, tutoring me to pursue a research and further career opportunities. I highly regard her for the great person and professional she is; as a true and undoubtful example of life achieving success.

I am endlessly grateful to my family, especially my parents and brother whose affection and constant encouragement has given me tremendous impetus in my academic pursuits.

Stephen Hawking once said *"if you are lucky enough to find love, remember it is there and don't throw it away"*. Finally, to my truly beloved wife for the faith and belief in me, embracing this challenge as if it was her own. Her support, dedication and love were key and motivation to my journey and success, and therefore I thank her greatly and with all my heart.

...à minha família

Kurzfassung

Lineares Reibschweißen (LRS) ist ein Festphasen-Fügeprozess, bei dem die Verbindung zweier Komponenten durch ihre relative Hin- und Herbewegung unter axialen Druckkräften erfolgt. Die an der Grenzfläche erzeugte Reibungswärme in Verbindung mit der aufgebrachten axialen Kraft und der relativen Bewegung bewirkt, dass sich eine plastifizierte Schicht bildet, die die stoffschlüssige Verbindung der beiden Teile fördert. Gegen Ende des Prozesses wird die Relativbewegung beendet und die Teile werden über das plastifizierte Material zusammen geschmiedet, wobei sich an der Fügestelle ein Wulst ausbildet.

Bis in die letzten Jahre wurde das Verfahren ausschließlich in der Luft- und Raumfahrtindustrie kommerziell zur Herstellung von Aeroengine-Blade-Scheiben aus Titanlegierungen (auch "Blisks" genannt) verwendet. Das Potenzial des Prozesses hat sich jedoch auch auf andere industrielle Anwendungen wie die Kettenherstellung, das zentrale Thema dieser Dissertation, ausgeweitet. Obwohl das Abbrennstumpfschweißen (ABS) nach wie vor das hauptsächliche Fügeverfahren für Ketten ist, wurde das lineare Reibschweißen als praktikables Verfahren beim Kettenschweißen eingeführt, da fehlerfreie und reproduzierbare Schweißnähte mit hervorragenden mechanischen Eigenschaften hergestellt werden können. Im Gegensatz zum ABS , bei dem es sich um ein Schmelzfügeverfahren handelt, treten beim LRS keine Schweißfehler wie Segregation oder Heißrissbildung auf. Zudem hat das ABS im Vergleich zum LRS relativ geringe Produktivität aufgrund zusätzlicher Schritte während der Herstellung, wie z. B. der Wärmebehandlung nach dem Schweißen als Folge der erheblich breiteren Wärmeeinflusszone.

Die in der vorliegenden Dissertation behandelten Themen sind Teil eines Folgeprojekts und behandeln im Wesentlichen die numerische Modellierung des LRS im Rahmen der Kettenfertigung. Daher wurden thermomechanisch gekoppelte Finite-Elemente-Modelle unter Verwendung der kommerziellen Software DEFORM entwickelt, um den Prozess zu verstehen und einige der dazwischen liegenden physikalischen Größen vorherzusagen, wie z. B. Temperaturverteilung, Gratbildung, axiale Verkürzung.

Die Modellierungsarbeiten wurden auf die bereits gut untersuchte *Hero* Kette mit einem Querschnitt von 22x24 mm angewendet, die für Schwerlastanwendungen (Fördern und Heben) eingesetzt wird. Zusätzlich wurden kleinere Stifte mit einem Durchmesser von 10 mm mit Hilfe der statistischen Versuchsplanung systematisch untersucht, um die Anwendbarkeit, Reproduzierbarkeit und Stabilität des Verfahrens zur Herstellung von Ketten für weniger anspruchsvolle Anwendungen zu beurteilen. Diese Untersuchung sah als primäres Ziel die Erreichung exzellenter mechanischer Eigenschaften vor, um die Anforderungen der Industrie zu erfüllen, was erfolgreich durchgeführt wurde. Der Schwerpunkt dieser Dissertation liegt jedoch auf der numerischen Simulation. Daraufhin wird ein eigener Entwurf vorgestellt, der experimentelle und numerische Ausgaben miteinander verbindet.

In beiden Fallstudien wurden Validierungsversuche durchgeführt, um die Angemessenheit der entwickelten Modelle zu bewerten, aus denen eine gute Übereinstimmung mit den relevanten Prozessergebnissen erzielt wurde. Dies ermöglichte die sichere Verwendung des Modellierungsansatzes zur Vorhersage von Daten, die experimentell verglichen werden können.

Schlüsselwörter

Linearreibschweissen von Kettenglieder
Numerische simulation
DEFORM

Abstract

Linear friction welding is a solid state joining process in which the bonding of two components is accomplished by their relative reciprocating motion under axial compressive forces. The mechanical energy applied in terms of dislocation and axial force is transformed into frictional heat dissipation and elastoplastic deformation. Then, the plastic deformation contributes as additional heat power source and generation of new chemically active surfaces. Towards the end of the process, the relative movement is ceased and the parts are effectively forged together with some plasticised material remaining at the weld interface.

Up until recent years, the process has been commercially used solely in the aerospace industry for the production of titanium alloy aeroengine bladed disks, also known as "blisks". However, the potential of the process has been spreading to other industrial applications, such as chain manufacturing, which is the central topic of this dissertation. Despite the fact that flash butt welding is still the main chain joining process, linear friction welding has been introduced as a viable process in chain welding due to the ability of producing clean and reproducible welds, with exceptional mechanical properties. Contrarily to flash butt welding which is a fusion joining process, welding defects such as, segregation or hot cracking are not prone to occur. Another contrasting characteristic is the relatively low productivity of flash butt welding compared to linear friction welding, due to additional steps during manufacturing, such as post-weld heat treatment as a consequence of the significantly wide heat affected zone.

The subjects discussed in the present dissertation are part of a follow-on project, and deal essentially with numerical modelling of the linear friction welding process within the scope of chain manufacturing. Thus, thermo-mechanically coupled finite element models were developed, using the commercial software DEFORM, to comprehend the process and predict some of the intervening physical quantities, such as temperature distribution, flash formation, axial shortening, among others.

The modelling campaign was applied to the already well investigated 22x24 *mm* cross-section *Hero* chain used for heavy duty applications (conveyor and lifting). Additionally, smaller cross-section pins with 10 *mm* in diameter were systematically investigated experimentally using *Design of Experiments* to assess the applicability, reproducibility and stability of the process for the production of chains to be applied in lesser demanding applications. This investigation envisioned as primary objective achieving excellent mechanical properties to meet industry's demands, which was successfully accomplished. However, the focus of this dissertation is toward numerical simulation, thence a dedicated design coupling experimental and numerical outputs will be presented and discussed.

Validation experiments were carried out in both case studies to evaluate the adequacy of the developed models, from which good agreement was obtained for relevant process outputs. This enabled the modelling approach to be confidently used to predict data which is able to be compared experimentally.

Keywords

Linear friction welding of chains
Numerical simulation
DEFORM

Contents

List of Figures

List of Tables

Nomenclature

Symbol	Description	Unit
Abbreviations		
ANOVA	Analysis of Variance	
BM	Base Material	
DoE	Design of experiments	
FEA	Finite Element Analysis	
HAZ	Heat Affected Zone	
LFW	Linear Friction Welding	
TMAZ	Thermo-Mechanically Affected Zone	
WZ	Weld Zone	
Greek symbols		
α	Thermal Diffusivity	m^2/s
β	Time integration factor	
Γ	Euler Gamma function	
δ	Extrusion thickness	mm
$\delta\pi$	Variation of functional π	
Δt	Time step	s
ε	Elongation or true strain	
ε_{eff} or $\bar{\varepsilon}$	Effective or Von-Mises strain	
ε_{ii}	Principal strain in the i direction	

ε_{ij}	Strain tensor	
$\dot{\varepsilon}_{eff}$ or $\dot{\bar{\varepsilon}}$	Effective or Von-Mises strain rate	s^{-1}
$\dot{\varepsilon}_{ii}$	Principal strain rate in the i direction	s^{-1}
$\dot{\varepsilon}_{ij}$	Strain rate tensor	s^{-1}
$\dot{\varepsilon}_{max}$	Maximum strain rate	s^{-1}
ξ_J	Simplified diffusion function	
ξ_m	Magee's martensitic transformation funcion	
π	Functional	Nm/s
ρ	Density	kg/m^3
$\bar{\sigma}$	Flow stress	MPa
σ_{eff}	Effective or Von-Mises stress	MPa
σ_{ii}	Principal stress in the i direction	MPa
σ_{ij}	Stress tensor	MPa
σ_y	Yield strength	MPa
σ_{UTS}	Ultimate tensile strength	MPa
ω	Angular frequency	rad/s

Latin symbols

a or A	Amplitude	mm
$A(t)$	Interface contact area	mm^2
b_0 or C	Burn-off	mm
b_0^*	Relative burn-off	

$\dot{b_0}$	Burn-off rate	mm/s
e	Engineering strain	
$erfc(x)$	Complementary error function	
E	Young Modulus	GPa
E_{ph}	Energy applied at the interface during a certain phase	Nm
$E\left(\dot{\varepsilon}_{ij}\right)$	Work function	N/m^2s
f or B	Frequency	Hz
F_{int}^0	Load due to inertial movement of LFW machine during a "dry-run"	N
F_{int}^{net}	Net in-plane load	N
F_{int}^{total}	Total in-plane load	N
h	Heat transfer coefficient	W/m^2K
$,i$	Differentiation in i-direction	
k	Thermal conductivity	W/mK
P_i	Surface traction	MPa
$\dot{q}^{"}$	Heat flux	W/m^2
r	Pearson's correlation coefficient	
S	Surface	m^2
S_F	Surface where traction is prescribed	m^2
T_i	Interface temperature	$^\circ C$
u_i	Velocity component	m/s
v_r	Rubbing velocity	mm/s

V	Volume	m^3

Chapter 1

Objectives

The aim of this thesis is to investigate process characteristics associated with the LFW process and increase the existing understanding via numerical analysis, namely the finite element method (FEM). The importance of a greater understanding of the process may enable on development and optimisation of the process for chain applications. To achieve these aspects the following objectives have been established:

- Understand and predict the relevant physical quantities related to the pewag *Hero* chain using an already optimized parameter combination; and the applicability and the gathering of knowledge of the LFW process to join chains with smaller cross-section.
- Improve the predictive ability of previously developed models with an innovative modelling approach. Validate the models envisioning their use to predict outputs non-amenable to experimental measurement.
- Establish a conceptually straight forward and physical based modelling approach to be integrated in chain manufacturing.

Chapter 2

Introduction

The history of the chain dates back to the Bronze Age (3^{rd}-1^{st} millennium B.C.) and was most commonly used for jewellery items, namely necklaces. Over time, it has been recognized that the chain could also be used for technical purposes. A chain is a serial assembly of connected pieces, called links, typically made of metal, with an overall character similar to that of a rope in that it is flexible and curved in compression but linear, rigid, and load-bearing in tension. A chain may consist of two or more links, and further categorized by their design, which is dictated by their use. Those designed for lifting, such as when used with a hoist; for pulling; or for securing, such as with a bicycle lock, have links that are torus shaped, which make the chain flexible in two dimensions (the fixed third dimension being a chain's length.) Small chains serving as jewellery are a mostly decorative analogue of such types. Moreover, those designed for transferring power in machines have links designed to mesh with the teeth of the sprockets of the machine, and are flexible in only one dimension. They are known as roller chains, though there are also non-roller chains such as block chain[2,3].

The pewag group is one of the oldest chain manufacturers in the world and has become one of the leading chain manufacturers. Its history dates back to 1479 with first documented references of a forging plant in Brückl. In 1787 a chain forge was founded in Kapfenberg and few years later another one was founded in Graz, in 1803. Approximately 30 years later an iron casting plant was established in Brückl but it was not until 1912 that the first snow chain in the world was produced. After 10 years, the plants in Graz and Kapfenberg were merged and the name "pewag" was created. In the 1970s a sale company was established, both in Germany and the United States. In 1994, exactly one year after the foundation of pewag Austria GmbH, the first subsidiary was established in the Czech Republic. In 1999 the Weissenfels Group was acquired, although an early separation was issued four years later. In 2005 the group was reorganiyed into Schneeketten Beteiligungs AG, which is producing snow chains, and pewag Austria GmbH, which is manufacturing technical chains. In 2009 Chaineries Limousines S.A.S. was acquired[4].

In 2006 the cooperation between the pewag group and the Institute of Materials Science, Joining and Forming (IMAT) - TU Graz began within the scope of the project JOIN (2006-2010); followed by JOIN 4+ (2010-2014) and metalJOINing (2014-2018), in which this dissertation is inserted. The subject of interest is related to basic research of chain welding, with special interest over feasibility studies, machine design, parametric design and advanced modelling.

2.1 Reading guide

This section aims to describes the various subjects covered in the chapters of this dissertation.

The **Linear Friction Welding - State-of-the-art** presented in chapter 3, will support and framework the study described in this report. The literature study is divided in eight distinct parts: 1) An introduction - the basic principles of the process are introduced along with the industries where LFW is already a well established technology. 2) History of LFW - overview of historic elements related to the process such as, origin of the first existing patents, research dissemination around the world and companies pioneering the successful implementation the process. 3) LFW operation - the elementary principles behind LFW machines and its principles. Furthermore, the sequence of operations from clamping until release phase are described. 4) Welding parameters - the intervening parameters in the welding process are listed and analysed in terms of their influence in the mechanical and metallurgical behaviour of linear friction welded joints. 5) Characteristics of LFW - An overall discussion on the microstructure of various linear friction welded alloys is presented. Moreover, a follow-up is given on the mechanical properties achieved throughout various studies, in terms of tensile strength, hardness, fatigue testing, and residual stresses. 6) Process modelling - An overview on the analytical and numerical efforts is carried out. 7) Advantages and disadvantages of LFW - The major benefits in using LFW as a rapid, repeatable and flexible manufacturing process are presented, as well as the main shortcomings of the process. 8) A new era in chain manufacturing - the leading research developments within the scope of chain production using LFW is covered.

The **Model description** is reported in chapter 4 provides the explanatory remarks regarding the developed of the FEM models; and is composed by twelve subchapters: 1) Introduction - introductory remarks and highlights on the modelling case studies covered by the present thesis are presented. 2) Modelling strategy - . 3) Components of the model - comments on the components used to build-up the thermal and thermo-mechanical models. 4) Geometries - Geometrical detailing on the components assessed in the previous point concerning the case studies in hand. 5) Meshing characteristics - explanatory remarks on the choice of mesh for the 2D and 3D models. 6) Mathematical formulation - constitutive equations which describe the thermal and thermo-mechanical problems. 7) Energy input analysis - describes the methodology used to substitute a friction model by a power model at the weld surface. 8) Material model - . 9) Loads and boundary conditions - mechanical load and movement, thermal dissipation and initial conditions are prescribed to 2D/3D thermal and thermo-mechanical models. 10) Solving strategy - the computational solvers used to resolve the numerical problem are described. 11) Mesh control and distortion - time step choice to keep the mesh in check under severe distortion. 12) Model limitations - the main shortcomings of the developed models are discussed.

The **Procedure implemented for numerical validation** chapter given in chapter 5 is divided in four parts, providing procedural details carried out to assess the adequacy of the developed models. 1) The RSM-1 machine - a brief introduction to the LFW research-purpose machine, installed at pewag GmbH facilities in Kapfenberg, is made. 2) Thermal measurements - thermocouple apparatus is described to validate the thermal histories yielded by the models. 3) Residual stress measurements - the experimental procedure around the installation of the hole-drilling strain gauges is described, as well as their positioning. 4) Mechanical and metallurgical characterization - the equipment and methods used in the mechanical and metallurgical characterization of the process are bestowed in this subchapter.

Chapter 6 is the prominent section of this thesis dealing with the **Results and discussion**, and comprises 2 main subjects: 1) Numerical analysis of LFW applied to pewag *Hero* chain - highlights the results obtained

for the commercially used *Hero* chain under different perspectives using 2D/3D modelling approaches; namely on thermal histories, flash formation mechanisms and morphology, burn-off rates, mechanical and thermo-metallurgical analysis. 2) Numerical analysis of LFW applied to small cross-section - the statistical results towards the influence of process parameters on several experimental and numerical outputs is discussed. Moreover, the validity of the yielded statistical models is appraised.

Finally, the **Summary** in chapter 7 gathers the relevant remarks on the performance and major findings of the developed models and some future challenges that might traduce in added value to the subjects covered in this dissertation.

Chapter 3

Linear Friction Welding - State-of-the-art

This literature study aims to provide an up-to-date review of the published works on the linear friction welding so that the current "state-of-the-art" may be identified and the process better exploited. The basics of the process will firstly be described followed by a description of the workings of linear friction welding machines and their operation. The typical microstructure characteristics of LFW joints are discussed, along with mechanical properties, such as tensile strength, hardness measurements and fatigue life assessment. Additionally, residual stresses, welding defects, followed by tooling effects on the properties of LFW joints are identified. Next, the work on process modelling is discussed in terms of analytical and numerical analysis. In the latter analysis, the main modelling approaches and validation campaigns are described. Finally, a dedicated section to the main developments of LFW employed specifically to chain manufacturing is presented.

3.1 Basic fundaments

Linear friction welding (LFW) is a solid state joining process[5] consisting of two parts where one them is stationary and forced against another that is reciprocating in a linear motion in order to generate frictional heat[6]. The heat combined with force perpendicular to the weld interface, causes the material to deform, plasticise and expelled from the weld interface in the form of flash, ultimately causing the workpieces to shorten (burn-off)[7]. In the flash, the initial surface-oxides along with other impurities are extruded, allowing a clean metal-to-metal contact between the parts and subsequently form a joint[8–10]. The expulsion of such artefacts are of utmost importance as they affect mechanical properties[11,12].

LFW is an established technology for the manufacture of titanium alloy integrated bladed disks (blisks) for aero-engines[13]. However, owing to the many benefits of the process, the opportunity to use this process to manufacture components in aluminium and steel alloys is receiving active consideration within industries, such as automotive[8] and chain manufacturing[14,15].

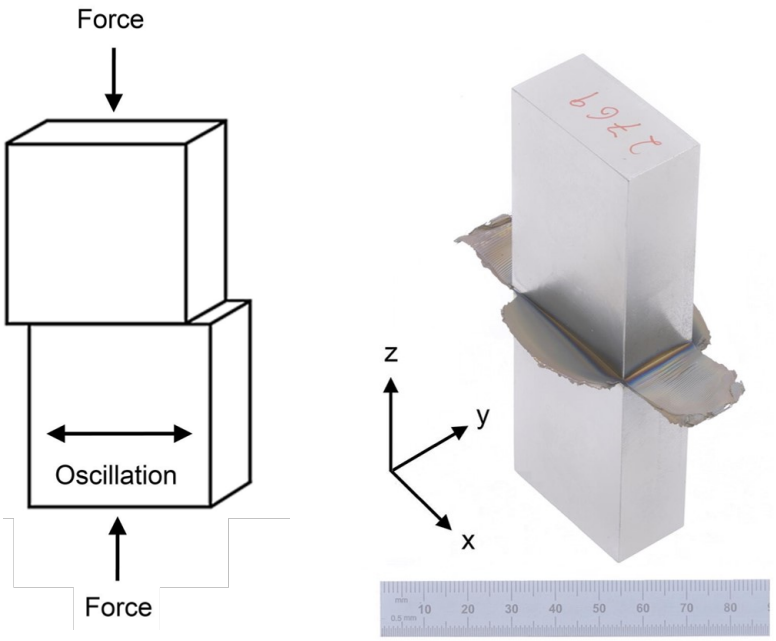

(a) (b)

Figure 3.1: (a) LFW process schematic and (b) a completed weld showing the expelled flash, with oscillatory motion in the x-direction (based on McAndrew et al.[16]).

3.2 History of LFW

The first existing patent describing the LFW process appeared in 1929 by Walther Richter (Germany)[17,18]. However, no actual application or research activity was developed as the description of the reciprocating motion was very vague and the process was labelled as "very doubtful" by Vill (Russia) in 1959[5,19]. In 1969 The Caterpillar Tractor Company (Peoria, IL, USA) filed a patent describing a machine capable of reproducing the reciprocating motion required for the process[20]. The process was studied more systematically in the UK in the 1980s at The Welding Institute (TWI), the University of Bristol and Rolls-Royce plc. Despite the reduced availability of research machines and the high costs required for industrial machines, some industrial countries have research groups which produced an increasing number of research papers.

In Europe, particularly in the UK, TWI and Rolls-Royce plc play an important role in research and information dissemination on LFW, through university based research from mathematical modelling to microstructural investigation in Cranfield, Herriot-Watt, Bristol, Birmingham, Manchester and Cambridge. In Italy the universities of Bologna and Palermo have contributed actively for the research in LFW with several publications. ACB (Cyrill Bath) in France designs and manufactures LFW machines for research and production purposes[21].

In Asia, the Northwestern Polytechnical University (NPU) has contributed for research advances for the last decade having built and operating its one LFW unit. Also, the Beijing Aeronautical Manufacturing and Technology Research Institute (BAMTRI) performs research on the process.

In the USA, companies, such as Manufacturing and Technology Inc. (MTI) and the ACPI Company have

been investing on development and design of LFW machinery[21].

Although the LFW process has been available for three decades, the commercial applications of the process are vastly reduced to titanium alloy "blisks" for aerospace engines, in firms such as Pratt & Whitney, Rolls-Royce, MTU Aero Engines and General Electric. This arrangement allows considerable weight savings when compared to conventional "fir-tree" blade-disc assemblies[22]. Boeing Company proposed a concept of near-net-shape using the LFW process allowing structures to be assembled from simple shaped parts (figure 3.2)[23]. Note that if the part from figure 3.2 were to be machined from a solid part either time and material would be wasted; and near-net-shape forgings on the other hand would be very expensive for most applications. Moreover, LFW traduces in a material cost saving of up to 90% when compared to traditional machining operation and a promising method for low volume near-net-shape component manufacturing[21].

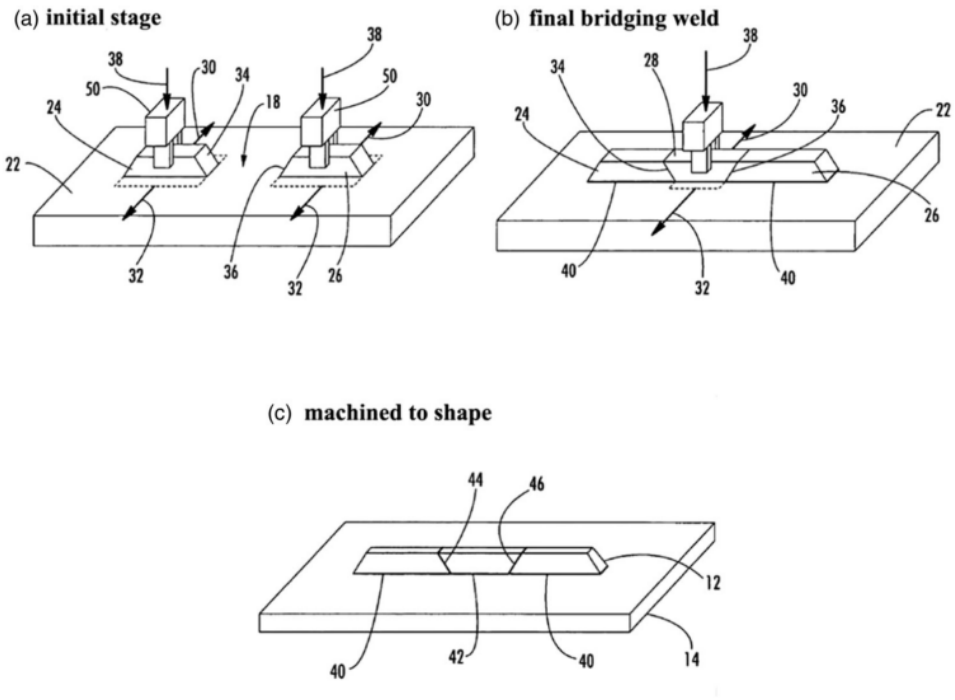

Figure 3.2: Near-net shape components manufactured with LFW a-c[23].

3.3 LFW operation

The elementary principle of LFW machines involve two mechanisms: one responsible for the oscillatory movement of one of the workpieces and a further mechanism that allows the remaining workpiece to be pushed against the oscillating one. The force application is dealt by means of a hydraulic ram, whereas oscillation is either through mechanical or hydraulic means.

3.3.1 Machine variants

Figure 3.3 shows a basic schematic diagram of the oscillating mechanism of an hydraulic-type linear friction welding machine. The components of the system consist on: a pump, which supplies high pressure hydraulic

fluid into a stack of accumulators; a valve, which allows the high pressure fluid from the accumulators to be alternately transferred into each end of the hydraulic cylinder and piston assembly creating the reciprocating motion[24].

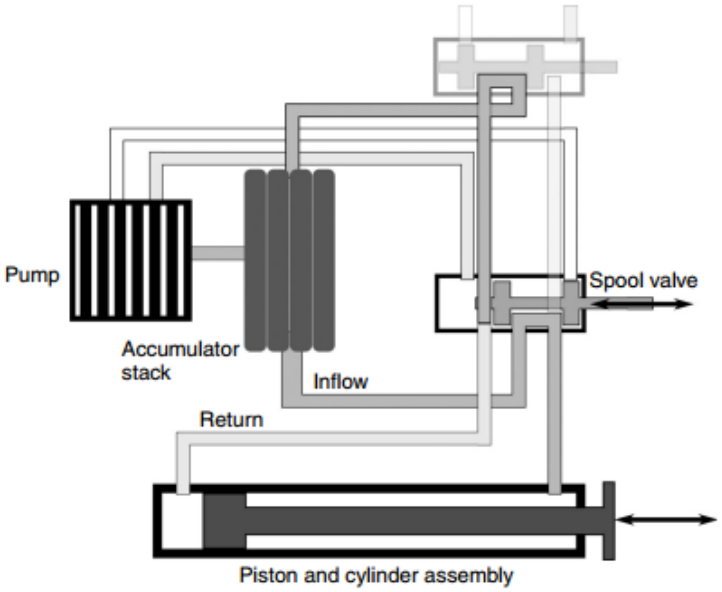

Figure 3.3: Schematic diagram of the oscillation mechanism of a hydraulic-type LFW machine. The spool valve in the figure oscillates in and out, which allows hydraulic fluid to be alternately forced into the top and bottom of the cylinder and piston assembly, which in turn creates the reciprocating motion. The tooling to hold the parts to be welded is attached to the piston[24].

For the mechanical variant schematically shown in figure 3.4, a common assembly involves a drive motor, which rotates two shafts that are linked to one another. The crankshaft closest to the drive motor is solid, while the one furthest is hollow and has a mechanism that allows it to be phase shifted with respect to first crankshaft. To each of the crankshafts a crank is attached, and a whipple beam is in turn attached to the cranks. The cranks are connected to the whipple beam by way of flexible elements and the tooling to hold the reciprocating part is attached to the whipple beam. The flexible elements are weighted with balance weights to help stabilise the reciprocating motion. It is necessary that parts used in the machine are either machined from solid or are forged as they are subjected to cyclic loads, and these loads can be high when the machine is used at high frequencies and amplitudes[24].

The maximum stroke of the cranks, and the maximum amplitude achievable by the machine is reached when the two crankshafts are rotated in phase. When the crankshafts are rotated 180° out of phase the whipple beam rocks so that its centre remains stationary, giving an amplitude of zero. To obtain an amplitude the phase between the two shafts must be less than 180°, or greater than 0°. The oscillation frequency is dependent on the rotational speed of the crankshaft[24].

The tooling for the reciprocating part is attached to the centre of the whipple beam. The left-hand image shows the crankshafts moving in phase so that the centre of the whipple beam reciprocates at the maximum amplitude. The right-hand image shows the crankshafts moving 180° out of phase so that the centre of the whipple beams remains stationary, giving a zero amplitude. The assembly also has four flywheels to stabilise the motion of the crankshafts[24].

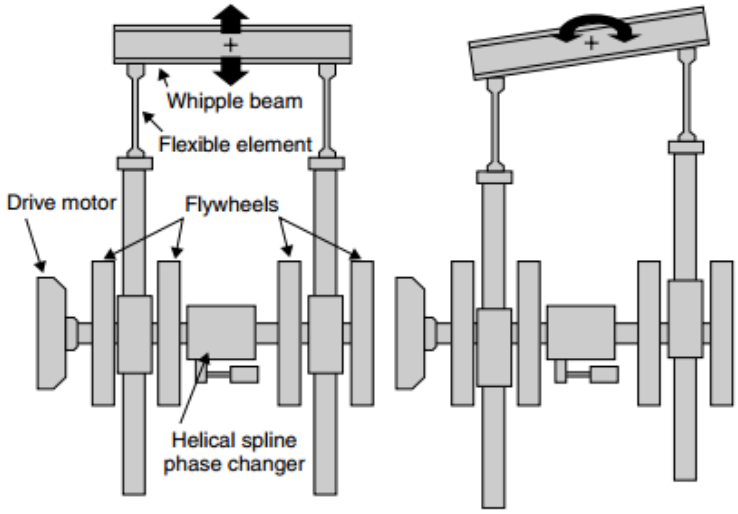

Figure 3.4: Schematic diagram of the oscillating mechanism of a mechanical-type LFW machine[24].

3.3.2 Sequence of operations

Linear friction welding is a process where the frictional heat is produced as one component is moving in a direct reciprocating manner relatively to another under pressure. The process can be divided in the six following steps.

1) Part Clamping

The parts are held using a clamping system designed to withstand the forces experienced during the process. Specimen and tooling preparation is critical to the process in order to guarantee a tight fit needed between the tool and specimen. Hence, the tooling must be custom built to accommodate particular specimen geometries[6,21].

2) Initialization and retract

The machine starts the reference point acquisition by bringing the clamped parts together under a small compressive force, thus setting the machine datum to zero. Subsequently, the apparatus retracts slightly, leaving a small separation between the workpieces. At this point positioning and machine calibration are done and the actual process ready to start[6,21].

3) Conditioning phase

The oscillatory motion of one of the workpieces is increased and and stabilized very quickly and the parts are brought together under a small force for a predetermined time. This phase is within the period comprising the ramp-up time, delimited by ***A*** in figure 3.5[6,21].

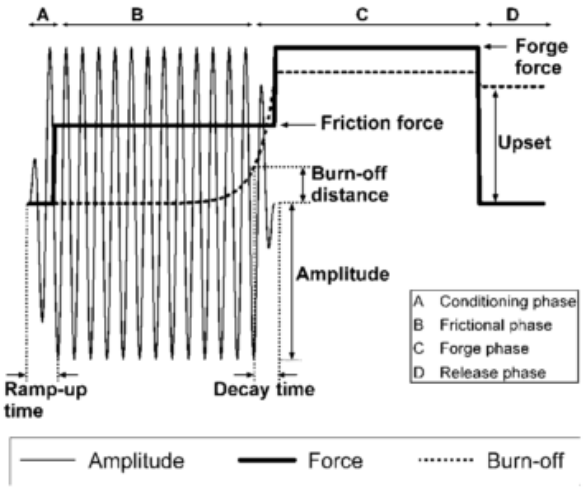

Figure 3.5: Schematic diagram of the parameter traces that are obtained during the linear friction welding process[6].

4) Frictional phase

The frictional phase (***B*** in figure 3.5) can be categorized in three sub-phases which are determined by the material behaviour, as depicted in figure 3.6[25,26].

Phase I, the initial phase: The two parts are brought in contact under pressure and heat through friction is generated. The rubbing of the two parts causes the asperities from the surface to wear out, increasing significantly the contact area. There is no axial shortening of the workpieces at this phase. The compromise between rubbing speed and axial load should be spot on in order to generate enough heat to compensate for the losses in conduction and radiation. If not, the lack of heat will lead to insufficient thermal softening and the following phase will not occur[25,26].

Phase II, the transition phase: If sufficient heat has been generated from the previous phase to soften the material, particles submitted to large wear are expelled from the interface. Also, the heat affected zone expands from the interface to the bulk material. The true contact area is considered to be 100% of the cross-sectional area and plastic deformation starts to occur since the soft plasticized layer formed between the two surfaces can no longer withstand the axial load[25,26].

Phase III, the equilibrium phase: Axial shortening of the workpieces begins as a result of the expelled material in the interface. The heat generated as a result of breaking and formation of new bonds is conducted away from the interface and a plastic zone develops. The stress state on the plasticized layer at the interface combined with the oscillatory movement causes the material to be extruded in the form of flash.

Instabilities may occur at this stage due to uneven temperature distribution, i.e. if temperature increases excessively away from the centreline of oscillation, the plasticized layer becomes thicker in that region, causing more plastic material to be extruded. This can result in rotation of the interface from the original plane. This might be due to initial misalignment of the specimens[25].

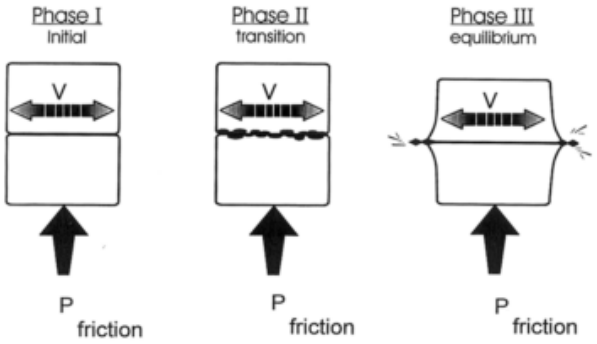

Figure 3.6: Frictional phases of the LFW process[25].

5) Forge or deceleration phase

The relative motion is stopped abruptly, in a predetermined time to ensure the correct alignment of the workpieces. Thereafter, a forge force is applied and held for a set time to consolidate the joint, given by ***C*** in figure 3.5. The forging force can either be the same or higher than the friction force[6].

6) Release phase

The forging load is stopped and the joined parts are released from the clamps and removed from the machine. When releasing the component from the clamps there is a slight decrease in upset due to elastic recovery. These features are presented by ***D*** in figure 3.5.

3.4 Welding parameters

The mechanical and metallurgical structure/appearance in a LFW joint is determined by several parameters[6,7,25,27]. The main input variables are:

- ***Oscillation frequency***: represents the number of sinusoidal oscillations (of the reciprocating part) completed in one second.
- ***Oscillation amplitude***: defined as the maximum displacement of the oscillating sample in relation to the reference position, i.e. the displacement between the oscillating and stationary parts are zero (fully aligned).
- ***Ramp-up time***: the time required for the welding parameters to reach steady state levels (see figure 3.5).
- ***Friction pressure***: the pressure applied perpendicular to the weld interface, during the frictional phase of the process. Pressure is obtained using the nominal area of contact at zero amplitude.
- ***Burn-off***: the shortening of the workpiece in the direction of the applied force. This factor, along with ***time*** or ***number of cycles*** are used to control the progress of the process in the equilibrium phase and trigger the forging phase.

- ***Decay time***: the time required to bring the amplitude to zero at the beginning of the forging phase.
- ***Forge pressure***: pressure applied during the forging phase of the process.
- ***Forge time***: the amount of time that the forging pressure is applied.

However, there are other important variables which result from the main input variables and cannot be easily changed through the variation of the main variables. These are[6,21]:

- ***Upset***: the total loss of length throughout the process. The upset exceed the burn-off distance mainly because of the loss in length due to the forging force.
- ***Shear (or in-plane) force***: the force parallel to the oscillatory movement.
- ***Burn-off rate***: the rate of shortening, i.e. the gradient of the burn-off curve.
- ***Welding time***: the total amount of time to weld a specimen.

Many author consider the oscillation frequency, oscillation amplitude and friction pressure to be the process inputs of primary importance, as their are related to the amount of heat input provided to the weld[28–31]. Although the frequency and amplitude of oscillation are two separate process inputs it has been shown by McAndrew et al.[32,33] that they may be considered as a single input – an average rubbing velocity – as varying either while keeping the average rubbing velocity constant has relatively little effect on the results. The average rubbing velocity v_r is defined as:

$$v_r = 4 \cdot a \cdot f \tag{3.1}$$

where a and f are the amplitude and frequency, respectively.

3.4.1 Effects of welding parameters

Various authors studied the effect of the process parameters in the properties of linear friction welded joints.

When studying the effect of friction time on the flash formation shape and axial shortening of linear friction welded C45 steel, Li et al.[34] concluded that sound welds could be achieved if the friction time stays above $3s$. Also, the axial shortening increases exponentially with the increase in welding time.

The same author reported in[30] that as the oscillation frequency increases, the interface temperature reaches more quickly up to a high temperature and the axial shortening also increases to a larger value at a faster rate. The same holds for the increase of both amplitude and friction pressure. These effects do not act independently, instead they can be integrated into one factor of heat input.

In the work conducted by Bhamji et al.[35] to AISI 316L austenitic stainless steel, an analysis was undertaken into the effects of welding parameters on weld microstructure. In particular the variation of weld line δ-ferrite fraction was observed with different welding parameters, and it was shown that at higher burn-off rates a lesser amount of delta ferrite was formed at the weld interface. This was attributed to the quicker expulsion of hot plasticised material from the weld, which did not allow enough time at temperature for large amounts of delta ferrite to form. Conversely in low burn-off rate welds a slow moving layer of hot plasticised

material was present which did allow time for delta ferrite formation and therefore much greater amounts than in the parent material were present at the weld line. The highest burn-off rates occurred at mid-range frequencies and amplitudes and high pressures as shown in figure 3.7. These findings contradict literature and are believed to be associated to the fact that this material essentially lubricates the joint and is very hard to remove, which causes the low burn-off rate.

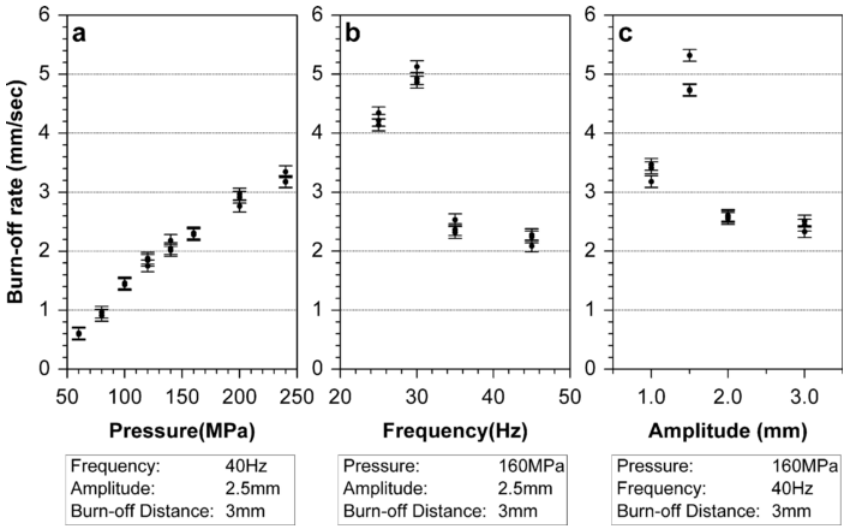

Figure 3.7: Effects of pressure, frequency and amplitude on burn-off rate[35].

Romero et al.[36] acknowledged, due to evidences in the microstructure and residual strain in Ti-6Al-4V, that an increase in welding pressure led to "colder" welds in comparison with lower pressures. Although the increase in pressure might suggest an increase in power input, it also resulted in a decrease in welding time and acceleration of material flow, which could lead to a decrease in total thermal exposure.

Wanjara and Jahazi[12] investigated the influence of four process parameters, namely, frequency, amplitude, friction pressure and axial shortening on the size of recrystallised β grains in the WZ of Ti-6Al-4V. This work gives a good insight as to how the interface temperature varies as welding parameters are changed, as the β grain growth will be dependent on it. According to figure 3.8(a) and (c), an increase in frequency or pressure increases the size of the prior b grains. This is believed to be associated with the increase in power input, along with an increase in frequency or pressure, leading the temperature at the interface to be greater. However, the increased prior β grain size could also be related to low cooling rates when high parameters were used. Furthermore, an increase in oscillation amplitude results in a reduction in the prior β grain size probably due to the fact that large amplitudes expose a considerable amount of materials to the surrounding atmosphere, resulting in increased convective heat dissipation.

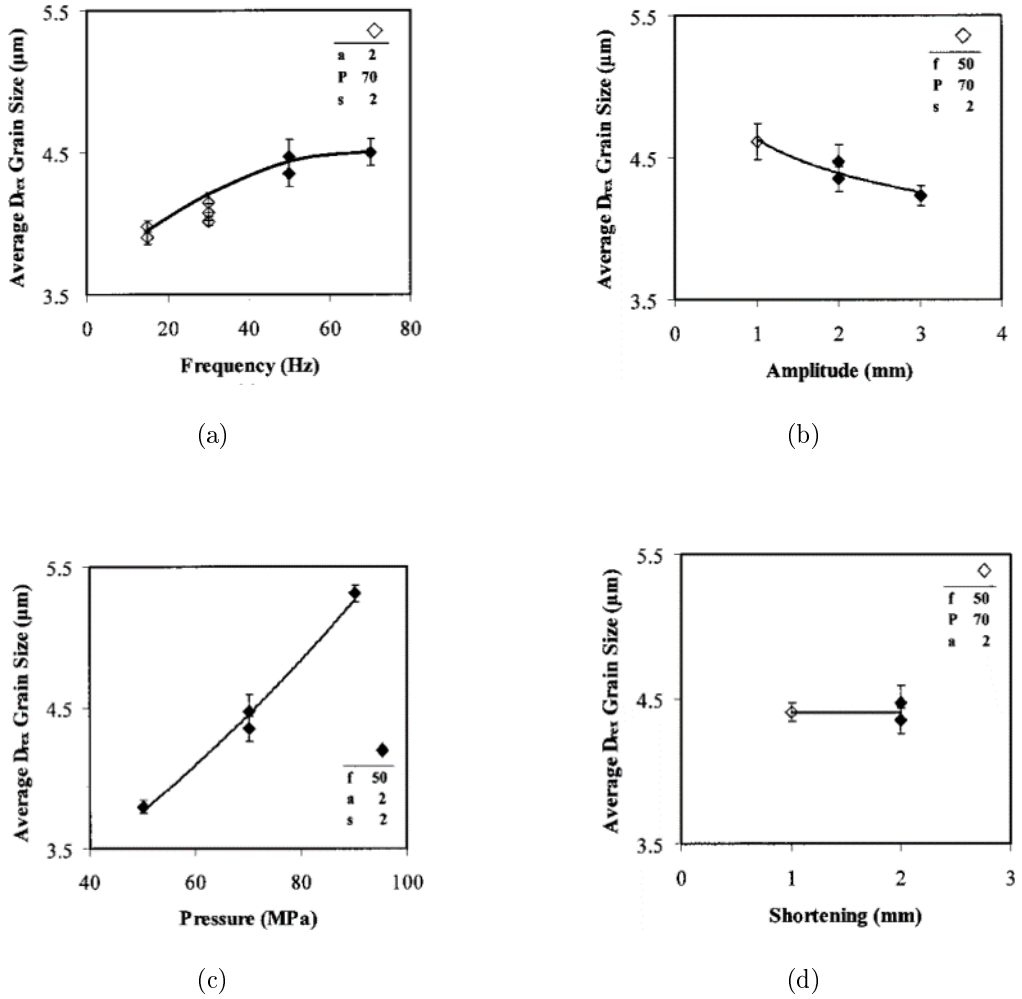

Figure 3.8: Effects of (a) frequency, (b) amplitude, (c) pressure and axial (d) shortening on the average β grain size in the WZ Ti-64 linear friction welds[12].

These parameter studies clearly demonstrate that the welding temperature can be controlled, to some extent, through the control of welding parameters. Minimising the peak welding temperature is an important objective, particularly when attempting to join highly dissimilar materials (e.g. aluminium to copper) by LFW. In such cases, the formation of intermetallics is usually a major obstacle. Therefore, minimising the welding temperature aims at avoiding the formation of detrimental intermetallic phases at the weld line[6].

3.5 Characteristics of LFW

The action of rubbing mating surfaces on one another is of a molecular and mechanical nature. The molecular action is a result of the attraction of two parts to one another; the mechanical action is generated by the pieces entering one another as they rub together[9]. As result, these two effect combined dictate the microstructural and mechanical characteristics of linear friction welded joints.

3.5.1 Microstructure

The temperature at the interface during LFW is not expected to exceed the melting temperature of the material. However, the peak interface temperature is very high and can be close to the solidus temperature[37], thus, along with the high pressures involved in the process, significant microstructural changes occur close to the weld interface. To characterize the different microstructural regions, the widespread nomenclature of friction stir welding was adopted[38].

The base material (BM) is at some distance form the weld line, and is characterized for suffering no plastic deformation, nor alteration in the microstructure since it is not subjected to the weld thermal cycle[38,39].

The heat affected zone (HAZ) lies closed to the weld line and experiences the effect of the weld thermal cycle, responsible for modifying the microstructure of the material and its properties. Withal, there is no optically visible plastic deformation[38,39].

In the thermo-mechanically affected zone (TMAZ) moderate plastic deformation and thermal cycle are responsible for the microstructural changes in this region, although recrystallisation does not occur. The grain is more elongated and highly deformed when compared to those in the HAZ and phase transformations can also occur, in some materials. Changes in this region are in general more evident than in the HAZ[38,39].

In the immediate vicinity of the weld line, in the weld zone (WZ) the material is subjected to intense plastic deformation and high temperatures due to heat generated by friction. These conditions lead to dynamic recrystallisation of the material, which produces a region consisting of very fine equiaxed grain and often an order of magnitude smaller than those of the BM[38,39].

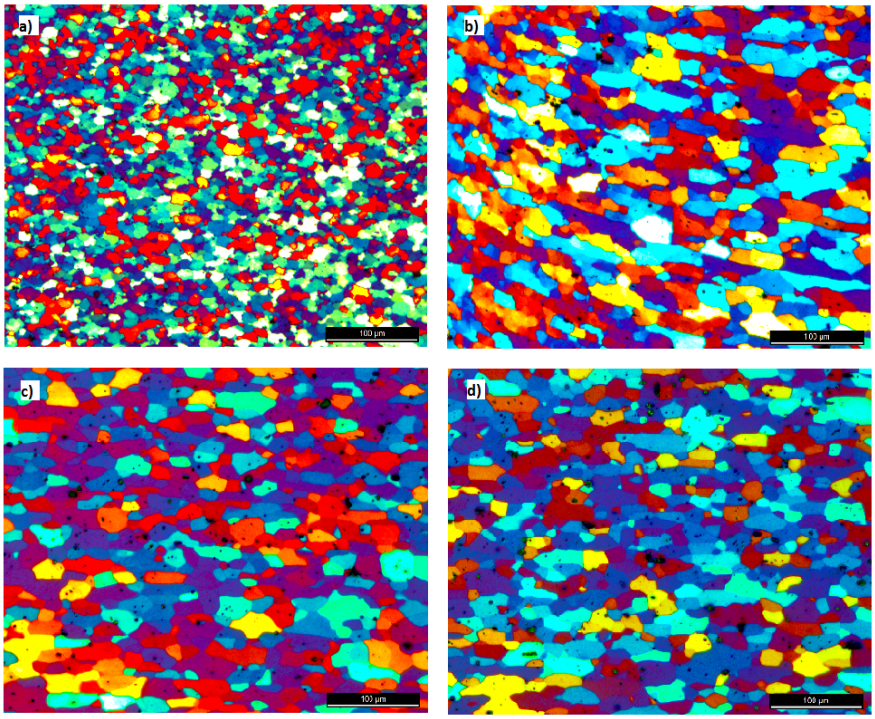

Figure 3.9: Micrographs of the different weld zones: a) WZ; b) TMAZ; c) HAZ; and d) BM[39].

3.5.1.1 Titanium alloys and aluminides

Microstructure investigations of linear friction welds in bimodal α and β structures titanium alloys, as shown in figure 3.10(a) and (b), has been carried out by several researchers[12,40–42]. It is evident that during LFW the material adjacent to the weld line surpasses the β-transus temperature, transforming the α-grains into β-grains. A fine grained structure is expected in this region, which is related to the material being exposed to high temperature and strain resulting in dynamic recrystallisation[43–45]. The fully β-transformed microstructure cools rapidly after the oscillatory phases of the process, preventing β-grain coarsening, resulting in a Widmanstätten microstructure[46] of α and β plates delineated by prior b grain boundaries, as shown in figure 3.10(c), or even Martensitic microstructures[47]. The difference, according to Ahmed and Rack[48], is due to the rate of cooling from the single β-phase. If the weld cools at a rate faster than $410°Cs^{-1}$then a diffusionless transformation occurs resulting in Martensite.

In the non-recrystallised TMAZ, the β-transus temperature is not reached, as fragments of the α-grains from the parent material are still present, although deformed, elongated and reoriented towards the direction of oscillation[49,50] (see figure 3.10(d)). Titanium wleds do not display a prominent HAZ, thus a direct transition from TMAZ to BM is possible[12].

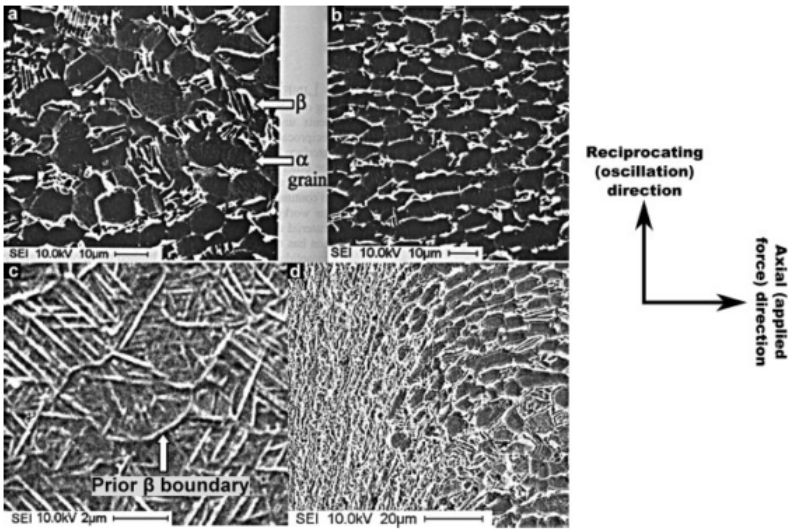

Figure 3.10: Microstructure of Ti-64 linear friction weld: (a) and (b) BM; (c) Widmanstätten microstructure in the WZ; and (d) non-recrystallised region of TMAZ showing deformation of the base microstructure[12].

Successful linear friction welded joints were obtained for α_2 titanium aluminides[51]. At high cooling rates, the relatively slow β to α transformation causes a microstructure of retained β, which has low notch toughness, or α_2 martensite, which is very brittle. To avoid such undesirable microstructures very low cooling rates are needed. Hence, welding parameter optimisation was suggested, with a regime of low forces and amplitudes and high frequencies. Despite these difficulties crack free welds have been produced in α_2 titanium aluminide.

3.5.1.2 Steel alloys

The microstructure of LFW C45 steel, from the weld centre to the parent metal, were determined as

superfine ferrite(α) + perlite (P) in the weld centre, deformed fine $\alpha + P$ in TMAZ, tempered sorbite (TS) in HAZ, tempered troostite (TT) in HAZ, tempered martensite (TM) in HAZ, respectively. Coarse $\alpha + P$ was obtained in the flash. The fine $\alpha + P$ structures were formed through the recrystallization of the deformed grains at the friction interface, while the coarse $\alpha + P$ structures in the flash were attributed to the grain growth because of the relatively long time at high temperatures. Moreover, the microhardness of the joint decreased gradually from the parent metal (789 ± 23 HV0.2) to the weld centre (248 ± 5HV0.2) and is attributed to the microstructure evolution throughout the joint experiencing different thermal histories during the process[52].

Successful welds were obtained for AISI 321 stainless steel. Via phase fraction maps it was possible to acknowledge that ferritic phases were no longer present on the WZ. This is, on the one hand, because the ferrite in the WZ is broken after extrusion and deformation, thus forms dispersed microstructure; on the other hand, part of ferrite decomposes into γ (austenite) and σ phase during the process[53].

3.5.1.3 Nickel based superalloys

The presence of oxide particles in LFW IN718 aligned around the weld interface were reported by Mary and Jahazi[37]. Their concentration and distribution, varying with process parameters, affect the weld integrity. The TMAZ characterised by a global loss of strength (from 334 HV to 250 HV) is associated with temperatures exceeding 800°C and causing $\gamma^{'}$ and $\gamma^{''}$ dissolution.

This dissolution effect of strengthening precipitates at the weld line of linear friction weld was also found for other nickel alloys[54]. Effects of crystal orientation on weldability and microstructural evolution occurring during linear friction joining of single crystal nickel-base superalloy to polycrystalline nickel-base superalloy were studied. The materials were easiest to weld when the primary slip system of the single crystal was favourably orientated to give a high Schmid factor. Other than this orientation the LFW process proved to be unsuccessful.

3.5.1.4 Aluminium alloys

During LFW process of AA2139, heating combined with plastic deformation can lead to change in the phase composition at the expense of dissolution or precipitation of different phases. As a result microhardness reduces by 30 HV on the average during transition to the TMAZ and weld centre zone[55]. A similar behaviour was reported when joining Al-Fe-V-Si 8009 aluminium alloy which showed a decrease in strength at the WZ compared to the BM due to overaging or dissolution of hardening particles[56].

3.5.2 Mechanical properties

Linear friction welding is particularly suitable for joining materials that have high heat resistance and low thermal conductivity. The high heat resistance allows a high frictional heat to be generated while the low thermal conductivity helps to concentrate the heat around the weld. These characteristics allow welded joints of titanium and nickel alloys to be made with low power input. In order to weld materials such as aluminium, which have a low heat resistance and a high thermal conductivity, a high power input is necessary. Ultimately this leads to a limited parameter window in which good welds are possible[57].

Table 3.1 summarizes the results of the tensile strength of the linear friction weld joint and welded joint efficiency factor of different alloys. The joint efficiency indicates the ratio of the tensile strength of the weld to the tensile strength of the BM, e.g. weld factor 1.0 means that the weld is warranted to have the same strength as the BM.

Material		σ_{UTS} of BM (MPa)	σ_{UTS} of the weld (MPa)	Efficiency
Titanium	Ti-64[12]	1030.6	1078.6	1.05
	Ti17[58]	1120.2	1079.3	0.96
	Ti-5553[59]	1108.2	1058.4	0.95
Aluminium	AA2024-T4[60]	469.7	434.6	0.93
	AA8009[56]	469.3	404.9	0.86
	AA2124-T4[61]	659.1	542.5	0.82
Steel	21Mn6[62]	530.4	592.1	1.11
	C45[34]	698.3	718.1	1.03
	AISI 316L[35]	602.5	610.8	1.01
Nickel	Waspaloy (PWHT)[11]	1374.8	1342.1	0.98

Table 3.1: Tensile strength and joint efficiency for different materials.

Hardness and microhardness investigations of linear friction welded joints have been performed by a number of researchers, mostly in Ti-64[36,41,63,64].

The investigation of the microhardness of linear friction welded Ti-64 alloy is shown in figure 3.11(a). The observed symmetry in the hardness profile, starting from the centre of the weld, indicates that the joining partners are thermo-mechanically influenced in the same way during the process, irrespective of whether it is the stationary or movable joining partner. An identical course of hardness could be confirmed in several works concerning this alloy, with the highest hardness values always occurred in the weld zone. This was attributed to the phase transformation and grain refining induced by recrystallization in this zone. The weld pressure had a very significant effect on the width in which the material seems to have exceeded the β-transus during welding, and the width of the TMAZ/WZ. In addition, the internal stresses in the weld zone also contribute to the increase in hardness[36].

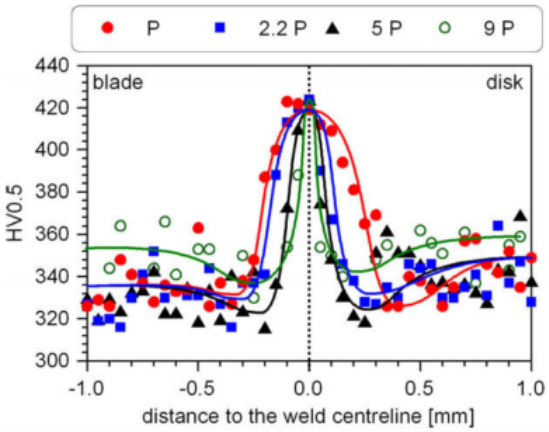

Figure 3.11: $HV_{0.5}$ hardness profiles as function of the distance from the weld line considering different weld pressures[36].

Regarding aluminium matrix alloy a contrary behaviour was acknowledged with a decrease in the welded zone by approximately 10% in respect to the BM. An important role is played by the concurrent effect of severe plastic deformation, recrystallization and presence of Cu–Mg co-clusters, which explain the lower hardness in the weld centre in respect to the TMAZ. The local strain hardening of severely deformed material, on the other hand, could be the reason of the hardness fluctuations in the joint, especially in the TMAZ[61].

The fatigue behaviour of linear friction welded joints has been investigated for a number of stress amplitudes in either low cycle fatigue (LCF) and high cycle fatigue (HCF)[50,61,65].

Stinville et al.[50] performed fatigue life assessment at nine different stress levels corresponding to maximum stresses of 550, 600, 650, 700, 725, 750, 800, 925 and 1000 MPa, covering the LCF and HCF domains. Coupons were machined with special attention given to their orientation in the as-received rolled plate of Ti–6Al–4V. Specifically, 50% of the blocks were machined with their length along the rolling direction (RD) and the other 50% with their length along the transverse direction (TD) of the hot-rolled bar. Under the conditions in this work, crack nucleation never occurred in the WZ or TMAZ, regardless of the frictional pressure and the maximal stress level applied. The location of crack nucleation depended on the applied stress level. For an applied stress higher than or equal to 725 MPa, all tested specimens failed on the RD side. In contrast, all specimens tested at a maximum stress equal to or lower than 700 MPa exhibited crack nucleation sites on the TD side.

Rotundo et al.[61] investigated the HCF life of silicon carbide particle reinforced (25 vol. % SiC) aluminium alloy. Fatigue strength at 10^7 cycles was equal to 289 MPa with a 50% probability of failure, which is 78% in respect to the fatigue strength of the base material, tested at $R = 0.1$. The high resistance was attributed to the absence of welding defects. Furthermore, failure was located in the TMAZ. The crack initiation mechanisms of metal-matrix composites (MMCs), in the HCF regime, are usually associated with imperfections in the material, such as porosities, reinforcement clusters or weak interface.

Little work was reported regarding impact toughness (IT) of linear friction welded joints. Ma et al.[49] investigated a total of five blocks of the Ti-6Al-4V. The same welding parameters were used for all five samples: amplitude 4 mm, frequency 33 Hz, friction force 17.9 kN, friction time 8 s, forging force 36.8 kN and compression time 4 s. The axial shortening is thus dependent on the aforementioned combination. Standardized U-notch specimens in the centre of the weld were made and tested destructively at room temperature.

Table 3.2 summarizes the results of the experiments for the tested samples. The results yielded an average value of 61.3 ± 5.8 J/cm^2. Sample 2 exhibited the lowest value and crack initiation in the BM, due to the lower toughness of the base material. On the other hand, Sample 3 reached the highest value. In this case, the crack initiated from the WZ, via the TMAZ, into the BM, finally fracturing at the BM. It has been reported that the fracture behaviour of Samples 1, 4 and 5 is similar to that of Sample 3.

Sample no.	1	2	3	4	5
IT	60.1	52.0	67.1	62.4	64.9

Table 3.2: Impact toughness values of LFW Ti-64 specimens[49].

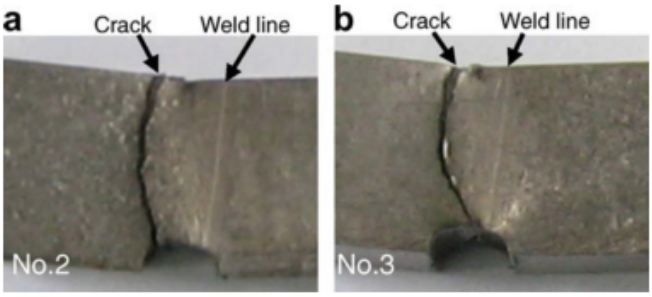

Figure 3.12: Macrographs of the fractured samples after impact test. (a) Sample 2; and (b) Sample 3[49].

3.5.3 Residual stresses

The residual stresses are generated via two mechanisms: plastic deformation experienced by the workpieces at elevated temperatures[66,67]; and thermally induced strain[29], which results from the difference in thermal expansion and contraction of the material during heating and cooling. The primary mechanism is due to the thermally induced strain that occurs during the post-oscillatory motion cooling[29].

Residual stress measurements were carried out mainly for titanium alloys using either high energy synchrotron X-ray or neutron diffraction, and each relies on calculating strains and stresses from changes in lattice parameter[22,36,66,68]. The results of these investigations are in close agreement and show tensile stresses in all three directions, close to the weld line. The tensile stresses were highest in the transverse direction (z-direction), i.e. in the welding plane perpendicular to the direction of the vibration, and smallest in the axial direction (y-direction), as illustrated in figure 3.13.

The development of the residual stresses shown in these studies may have an adverse effect on the overall life, permanent deformation and especially on the fatigue strength. In[22,68] it was successfully demonstrated that by using a suitable post weld heat treatment (PWHT), the residual stresses in a linear friction welding joint can be reduced by 75-90%. An important dependence of residual stress relief on specimen size has been reported in Ti-64[69]. Hence, on small laboratory scale linear friction welded sample evidenced negligible residual stresses after PWHT, unlike a full scale "blisk", where significant tensile stresses were still present after a comparable PWHT.

It has also been suggested that residual stress development can be minimised by optimising welding parameters, namely higher frictional and compressive forces leads to a considerable reduction of residual stress. The low residual stresses in the welded joint were explained by the lower peak temperature, which occurs during welding with high forces[70].

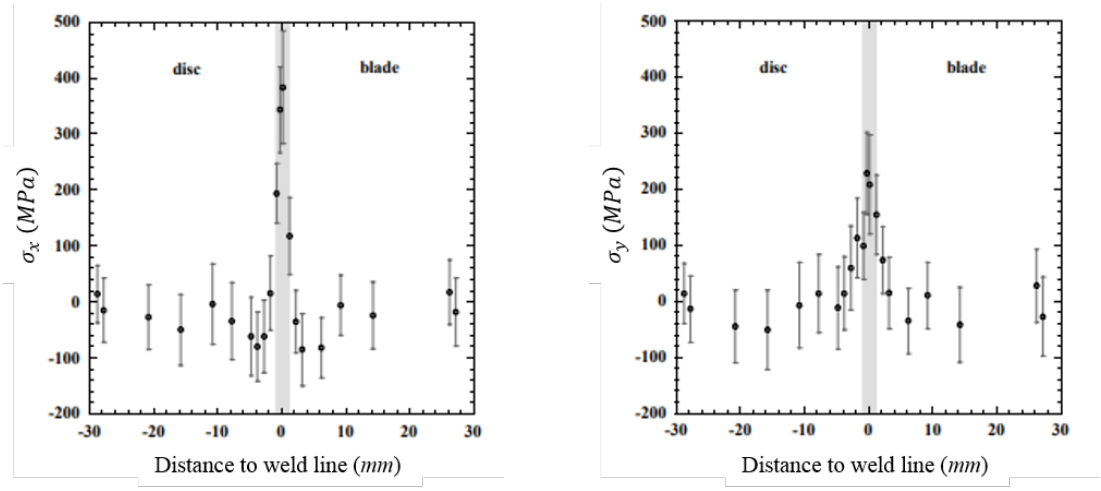

Figure 3.13: Stress as a function of position along the weld line: (a) x stress, (b) y stress, and (c) z stress. The shaded band centred at $y = 0$ represents the nominal HAZ[66].

3.5.4 Welding defects

In general linear friction welded structures comprise a repeatable, high quality joint, although some defects may occur. One of the most common area for defects is in the extremities of the weld, as these areas experience greater heat loss due to convection, relative to the central region, and are exposed to the atmosphere when the oscillating part is reciprocated.[71].

For welds with bifurcated flash lack of bonding can be found running from the flash towards bulk along the weld line. However, this lack of bonding usually only penetrates small distances and can be sorted as they are within machining tolerances. For extreme cases, particularly when brittle materials are welded, the lack of penetration can reach larger distances, as depicted in figure 3.14(a). Moreover, cracking in the heat affected zone can also occur if the amplitude is decayed too quickly at the end of the welding cycle, as illustrated in figure 3.14(b)[71].

Corner defects caused by a lack of flash extrusion from the corners of the welds can also occur, affecting drastically the mechanical properties. These features were observed when welding Ti-64[13,21]. The unbonded regions can be eliminated with a burn-off increase, since the heat from the flash and interface conducts into the corners causing them to soften and plastically deform. This results in the corner material merging with the rest of the interface[72].

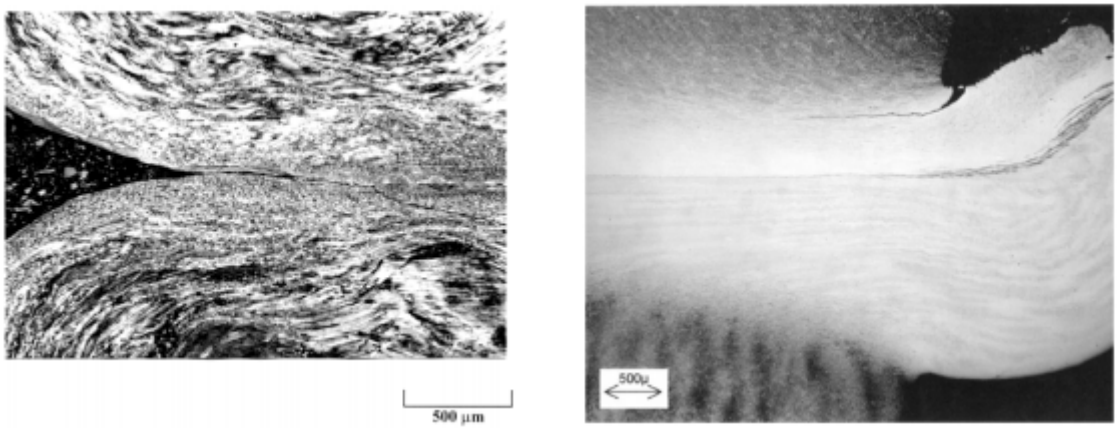

(a) (b)

Figure 3.14: Defects in linear friction welds: (a) weld in Ti-48Al-2Cr-2Nb showing a crack penetrating into the parent material geometry from the flash; and (b) weld between a martensitic (top) and stainless (bottom) steel showing cracking in the heat affected zone of the martensitic steel as a results of rapid amplitude decay[71].

3.5.5 Tooling effects

The effect of LFW tooling, namely the clamping system has been scarcely investigated on the processing of linear friction welds. However, during a recent LFW experiment, Li et al.[73] identified through high-speed photography that the reciprocating specimen does not move rigidly in the oscillation direction, but has a "micro-swing" relative to the oscillation plane, as shown in figure 3.15.

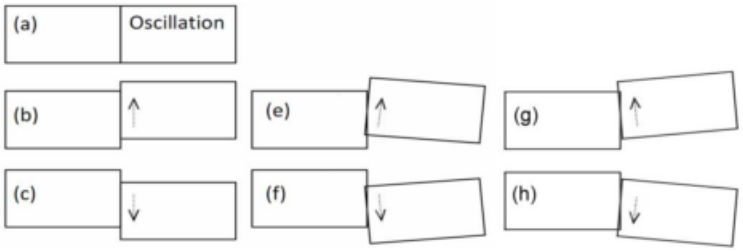

Figure 3.15: Movement of the oscillating workpiece (a); (b) and (c) ideally without; and (e)-(h) in reality with micro-swing[73].

Consequently, a model was created to investigate the effect of different swinging angles on the flash formation and temperature fields, and concluded that the burn-off rate increased with larger angles of micro-swing, which was due to one workpiece digging further into the other and extruding more material per cycle.

On the other hand, the different micro-swinging angles had negligible effect on the interface temperature histories.

The positioning of the clamp in relation to the weld line proved to have a significant effect on heat generation and, as a consequence, temperature distribution[74]. Whilst comparing Ti-64 and AA2024, a change in the fixing height by 2 mm gave large qualitative and quantitative differences in the temperature and stress field. For the titanium alloy fixation at 10 mm of free length was preferable to avoid gradients in the middle of the contact zone and to provide symmetry in the stress and temperature fields which will produce a uniform output of flash. The aluminium alloy is more forgiving allowing a wider range of fixing height, 6 to 15 mm, for a uniform distributions of temperature along the contact line.

3.6 Process modelling

Experimental observations can be of limited use in LFW due to non-linear effects in a narrow weld zone, such as the variation of thermo-physical properties under high temperature gradients and the change of mechanical properties with deformation conditions (temperature and strain rate). The very complex thermo-mechanical nature of LFW makes it difficult to reveal the bonding nature and predict various properties of the joints. Numerical analysis using advanced computational tools can therefore play an indispensable role in providing insight into the rapidly evolving nature of the process[19,29,30]. This section divides the modelling efforts of the process into analytical and numerical.

3.6.1 Analytical modelling

Despite its importance, the number of papers presented on the subject of mathematical modelling of LFW is limited, as is the progress made in constructing satisfactory analytical models[9,75]. Reason for this are the simplifications involved, such as constant material properties and 1D heat flow[27,28]. Moreover, In most of the papers, sliding friction at the rubbing interface has been used to model heat generation. As this occurs during the early stage of the initial phase, the material close to the interface gradually softens and heat is generated not only through sliding friction but by mechanical dissipation throughout the plasticised material[76]. Therefore, sliding friction is not suitable to model all stages of the process.

Although the literature related to analytical modelling of LFW is sparse when compared to experimental and numerical investigations, the key finding are reported below.

3.6.1.1 Thermal modelling

Vairis and Frost[27] proposed a heat generation model for LFW (see figure 3.16). The heat generation rate per unit interfacial area (q) is written as:

$$q = \tau\nu = \frac{F_S}{A}\nu = \frac{\mu F_N}{W\left(L - a\sin\left(\omega t\right)\right)} a\omega \left|\cos\left(\omega t\right)\right| \tag{3.2}$$

where τ is the shear stress, ν the sliding velocity, μ is the coefficient of friction, F_S is the shear force, F_N is the normal load, a is the amplitude of oscillation, ω is the angular frequency, t is the time instant, L is

the length and W the width of the specimen (weld area = $L \cdot W$). The contact area term $W\left(L - \alpha \sin\left(\omega t\right)\right)$ changes with time to reflect the true area of contact[18].

The average heat generation rate can be determined by integrating equation 3.2 over a cycle, or as the oscillatory motion is symmetrically cyclic, integrating four times a quarter of the cycle

$$q_0 = \frac{1}{T}\int_0^T q dt = \frac{4}{T}\int_0^{T/4} q dt = \frac{4}{T}\int_0^{T/4} \mu P_N \nu dt = \frac{4}{T}\int_0^{T/4} \mu P_N a\omega \cos\left(\omega t\right) dt = \frac{2}{\pi}\mu P_N a\omega \tag{3.3}$$

where P_N is the constant friction pressure and T is the oscillation cycle period.

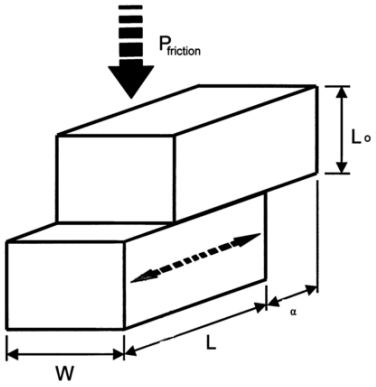

Figure 3.16: Analytical model: α amplitude of oscillation; L specimen length; L_0 overhang of specimen from specimen holder; $P_{friction}$ friction pressure; and W specimen width)[27].

To yield the temperature at the initial phase, Vairis and Frost[27] employed a 1D thermal model based on the "heat flux being applied to a solid bounded by two parallel planes" approach, described by Carslaw and Jaeger[77]. This allowed for the temperature T_i, at any distance back from the interface x, as a function of time t, to be determined, according to equation.

$$T_i = \frac{2^{m+1} q_0 \alpha^{\frac{1}{2}} t^{\frac{m+1}{2}} \Gamma\left(\frac{1}{2}m+1\right)}{\alpha} \sum_{n=0}^{\infty} \left\{ T_{i-1}^{m+1} erfc \frac{\left(2n+1\right) L_0 - x}{2\left(\alpha t\right)^{\frac{1}{2}}} + T_{i-1}^{m+1} erfc \frac{\left(2n+1\right) L_0 + x}{2\left(\alpha t\right)^{\frac{1}{2}}} \right\} \tag{3.4}$$

where α is the thermal diffusivity, Γ the Euler gamma function, L_0 is the overhang of the workpiece, m is a constant, q_0 is the heat flux, T_{i-1} is the temperature from the previous iteration, and the term $erfc(x)$ is the complementary error function.

This model involved simplifications, such as 1D heat flow, heat loss to the surroundings was neglected, coefficient of friction linearly increased as a function of time from 0.25 to 0.55, true contact area was linearly increased with time from 0% to 100%, and the model is static, hence no traverse movement was considered. The results of the model, with linear (constant) and non-linear (temperature dependent) material properties, were compared with thermocouple recordings. Constant material properties did not yield a satisfactory result as the temperature deviated significantly in the first 2 s. For non-linear material properties, on the other hand provided a better temperature prediction[27].

Although this effort is suitable for thermal modelling in the initial phase, questions of applicability must be raised regarding the equilibrium phase, since the model does not account for burn-off. The latter is an

important asset regarding the self-regulatory properties of the process. Wen et al.[78] proposed a phenomenological approach that accounts for the constant axial shortening in the equilibrium phase and allows to back calculate the interface temperature via two known temperatures elsewhere, for dissimilar LFW of Ti17 and Ti11. The following one dimensional Fourier heat conduction equation was solved:

$$\alpha \frac{d^2T}{dx^2} - v\frac{dT}{dx} = 0 \tag{3.5}$$

where α is the thermal diffusivity and v is the burn-off rate. Solving equation 3.5:

$$T = \frac{\alpha}{v} K_1 \exp\left(\frac{v}{\alpha}x\right) + K_2 \tag{3.6}$$

where K_1 and K_2 are constants. The constants are easily computed since the temperature results at distinct positions are known from the thermocouple measurements. The obtained results were comparable to the experimental ones and the highest temperature reached at the weld interface was 1280°C.

3.6.1.2 Material flow modelling

Vairis and Frost[25] adapted an already existing rotary friction welding mathematical model from Midling and Grong[79] to predict the material flow at the interface of linear friction welded Ti64. The model predicted that the strain rates appeared to be largest at the weld interface in the direction perpendicular to the reciprocating movement, decreasing further back as depicted in figure 3.17. Furthermore, the strain rates seem to decrease with the increase in the frequency of oscillation, however, the computed peak values are much lower when compared to the ones predicted by numerical models[80,81].

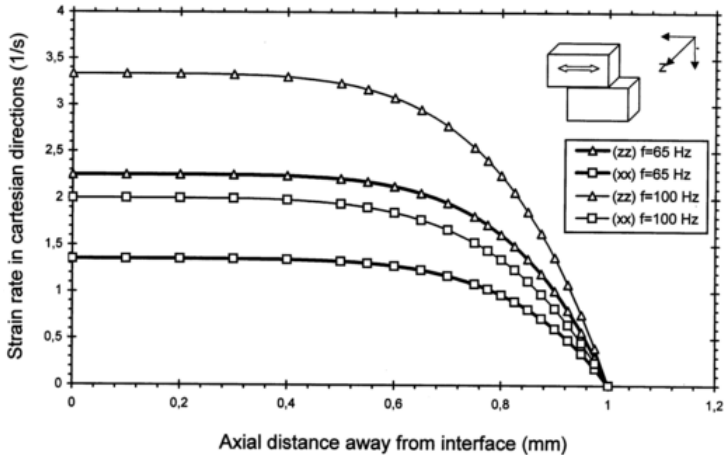

Figure 3.17: Predicted HAZ strain rate distribution during linear friction welding of Ti-6Al-4V for different oscillation frequencies (amplitude of oscillation: 0.92 mm; and friction pressure: 25.9 MPa)[25].

3.6.2 Numerical modelling

Analytical models often employ many simplifications, such as constant material properties and one dimensional heat flow[82]; thus affecting the accuracy of the information provided, specially in complex process

situations[9,83]. Finite element analysis (FEA) is therefore used for welding simulations as it discretises complex problems into more manageable sub-problems, approximated at finite time steps[84,85].

Modelling has been used to characterise various welding outputs, such as thermal fields[28,30,33,80,81,86–88], flash morphology and formation rates[28,30,33,80,81,86], contaminant expulsion[33,89], microstructural characterisation[90], residual stresses[29,91–94] and strain rates[33,80,81].

Several FEA packages have been used to model the LFW process, such as Abaqus[95], Ansys[96], DEFORM[97], Elfen[27] and Forge[80].

3.6.2.1 Modelling approaches

Various authors developed 2D and 3D computational models[5,27,30,33,80,91,95,97–100]. Despite this, 2D modelling has been of preference for the majority of published work, regarding the fact that it provides considerable information on LFW process, without the significant computational effort drawback experienced in 3D modelling. Hence, being more suitable for parametric studies. Nonetheless, 2D models are unable to replicate the flash formation in the direction perpendicular to the oscillation direction[33]. As a result, significant effort has been done in recent years to develop 3D models as they provide important insight into the full multi-directional flow behaviour of the process. This is particularly useful to understand the material flow and thermal cycles at the corners of the workpieces[16].

According to literature the LFW process can be modelled by three different approaches, as shown in figure 3.18.

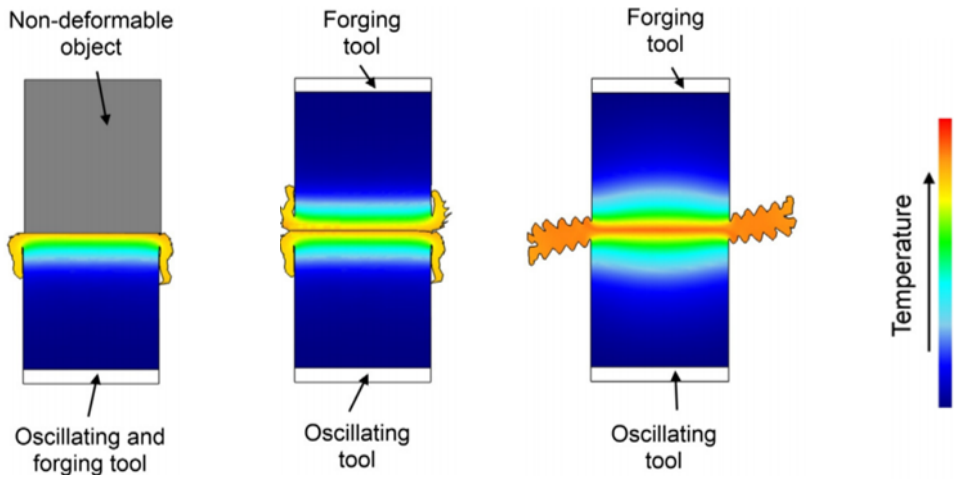

Figure 3.18: Modelling approaches: (a) one plastic workpiece and a non deformable tool; (b) two plastic workpieces; and (c) a single body representing two workpieces[33].

The first approach consists in modelling a single plastic workpiece that oscillates against a non-deformable object, as presented in figure 3.18(a)[27,30,99,101]. Nevertheless, the friction coefficient needs to be known in order to reproduce accurately the thermal aspects in the initial phase of the process. In addition, due to only one workpiece being modelled, it is impossible to model the flow behaviour after the two workpieces merge to each other.

The second approach is a result of the increase in computational power. Thus, many authors expanded on the early approach to create a model composed by two plastic workpieces[30,74,90,91,95,102–105], as depicted in figure 3.18(b). Once more, this approach requires information on the friction conditions on the interface and additionally does not consider mechanical mixing expected in transition and equilibrium phases.

The third approach depicted in 3.18(c), was developed by Turner et al.[80], who noticed that prior to the workpieces merging there is negligible macroscopic plastic deformation. Once a viscous layer is formed a single body representing two workpieces can be considered, since sticking friction takes place and 100% of true contact at the interface. A temperature profile needs to be put onto the single body that accounts for the heat generated by sliding friction. The high temperatures in the interface results in high viscosity of the material in the weld interface of the model. By considering the continuity in this region, the model is able to account for the joining of the separate workpieces. Thus, better modelling of the flash formation and its morphology is achieved[28,33,72,80]. However, the limitations inherent to this approach have to do with the fact that all stages prior to sticking conditions are not able to be modelled.

The type of modelling analysis can be selected between purely thermal, thermo-mechanical and thermo-metallurgical. For the last two analysis, elastic-plastic or plastic properties can be prescribed[16]. The purely thermal analysis neglects the elastic and plastic effects, thus requiring very little computational time. The elastic-plastic analysis allows for the inclusion of the elastic and plastic effects, therefore providing greater accuracy and insight, however considerable computational time is added. Purely plastic models neglect the elastic effects and assume incompressible flow, which is generally an adequate assumption when significant plastic deformation occurs[106]. As a result, purely plastic models require less computational effort than elastic-plastic analysis. Several authors[33,80,86] have demonstrated that the use of a purely plastic analysis is accurate to capture the experimental trends of the process during the oscillatory phase. However, according to Turner et al.[29] elastic-plastic analysis has to be used during the post-oscillatory motion cool down period if the residual stress formation is to be modelled. Metallurgical aspects must also be taken into account when dealing with residual stresses.

3.6.3 Validation

Validation is a critical task that has to be performed in order to assess the validity of a model[107]. Thus, successful validation to a range of outputs enables the predicted data from the models to be trustworthy concerning other outputs which are not measurable experimentally.

3.6.3.1 Analytical modelling

The Fourier heat conduction equation used by Wen[78] to mathematically estimate the temperature history of the joint during LFW and given by equation 3.5, was validated using two thermocouples 2 mm and 4 mm from the weld interface. The calculated and the measured curves of the WZ have a similar profile, with calculated values being a little higher than measured ones, as the temperature obtained by the infrared thermometer was the flash surface temperature and not that of the weld interface. Nevertheless, calculated temperature was comparable to recorded values.

3.6.3.2 Numerical modelling

Some efforts on numerical modelling include thermal history[28,30,33,80,86,88], flash morphology[80,81], burn-off history, shear loads, residual stresses, and microstructural grain radius and spatial distribution. Some validation results are presented in figures 3.19 to 3.21, demonstrating the ability of some models to capture experimental trends.

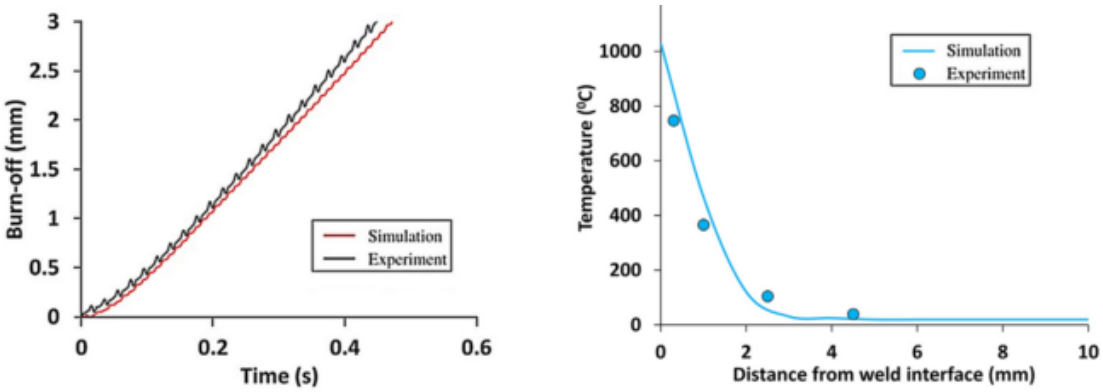

(a) (b)

Figure 3.19: Modelling validation displaying: (a) burn-off histories for Ti-6Al-4V workpieces[81]; and (b) thermal profile at the end of the initial phase for a Ti-6Al-4V weld[32].

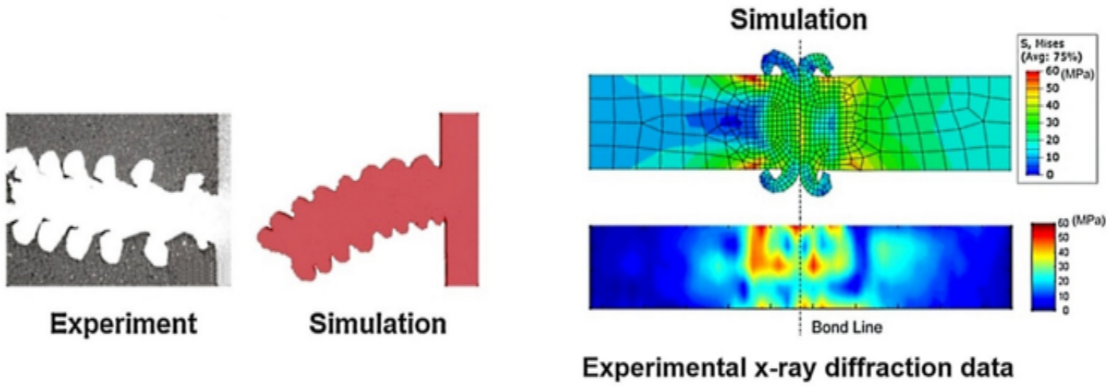

(a) (b)

Figure 3.20: Modelling validation displaying: (a) flash morphology for a Ti-6Al-4V weld[80]; and (b) residual stresses in an aluminium alloy weld[91].

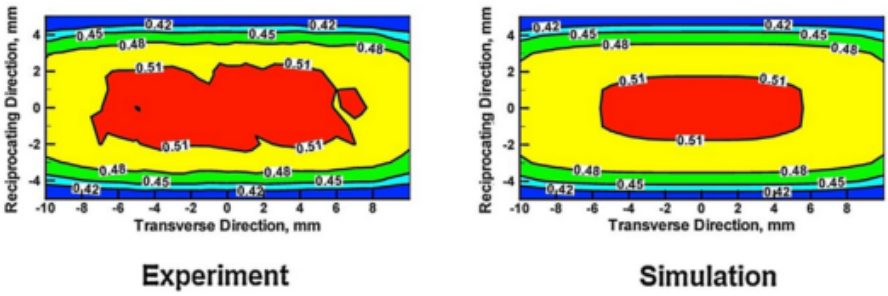

Figure 3.21: Modelling validation displaying the spatial distribution of the precipitate mean radius (in microns) over the mid-plane/contact surface of the LFW joint in a Carpenter Custom 465, H1000[98].

3.7 Advantages and disadvantages of LFW

Linear Friction Welding provides a rapid, repeatable, and flexible fabrication process for manufacturers in many industrial markets who produce parts with a variety of geometric shapes. Here are some reasons why:

- ***Superior joint quality***: the properties of any friction welded joint, including linear, are superior to traditional fusion based welded methods since the friction welding process does not actually melt the parent material. Melting causes a drastic change in a material's properties in the WZ. The HAZ of a linear friction welded joint is narrow and fine grained with a smooth transition to the unaffected base material.

- ***Quick welding process***: the LFW process is at least twice – and up to 100 times – as fast as other welding techniques[108].

- ***Minimal joint preparation***: Joint preparation is not as critical in the LFW process – machined, saw-cut, and even sheared surfaces are weldable. Less joint preparation also lowers overall cycle time, allowing greater throughput in a production process.

- ***Energy & Cost efficient***: the process is energy efficient and power requirements for an LFW machine are as much as 20% lower than those for conventional welding processes. Additionally, using LFW to join near net shape parts with geometries designed to use expensive material only where needed provides a faster, much less expensive alternative to machining parts from solid blocks[108].

- ***Ecologically friendly***: LFW is an ecologically clean process that requires no consumables, flux, filler material, or shielding gases to run, like conventional welding methods. It also does not emit smoke, fumes, or gases that need to be exhausted on the back end[9].

However, the following disadvantages have been recognized:

- ***Heat conductivity***: materials with high heat conductivity end up demanding a higher energy consumption from the machine, in order for it to provide the necessary heat at the interface to enable an acceptable joint.

- ***Low portability***: the maximum weld size is limited by the size of the machine and is typically limited to several hundred millimetres square. The greater the weld size, the bigger the machine to ensure rigidity, compromising its portability for *in loco* service.

3.8 LFW in chain manufacturing

Steel chains have been manufactured with the same methodology since the beginning of the 20^{th} century. This involves cutting steel wire or bar, bending them into the desired link shape and welding them together with energy intensive processes like resistance or flash butt welding (FBW). Most commonly, FBW for higher diameters. In flash-butt welding, the components to be joined are brought together end-to-end and a flashing voltage is applied. Where small contacts are made between the components, there is a high current density and the material resistance heats, melts and blows out of the joint in a shower of melted particles, giving the characteristic flashing action. This flashing progressively introduces heating and a softened zone at the component ends, while eliminating oxides and contaminants from the interface. After a pre-set burn-off length of the parent material, a forge force is applied to the parts to consolidate the joint. This produces a forge butt weld with no melted metal remaining in the joint. The process can be subdivided in three phases: preheating, flashing and upsetting or butting[109,110].

For a long time FBW is the process of preference regarding chain welding[15], and despite being a resistance welding process, good quality welds can be achieved for a number of materials. However, it is not without its drawbacks since FBW is a fusion process. Therefore, welding defects related to fusion joining processes such as, segregation or hot cracking are prone to appear[15,111]. Other limiting factors of this conventional technology are the shape of the chain links (round) as well as the weldability of the steel grade, which very much depends upon the carbon content and alloying elements.

To overcome the aforementioned shortcomings of resistance processes, LFW has been a subject of research in chain welding over the recent years, since it provides very clean and reproducible welds, comprising exceptional mechanical properties[14]. This section therefore provides some of the most relevant milestones and research achievements in LFW of chains to this date.

3.8.1 Chain link design

One of the limitations associated to FBW is the geometric restrictions imposed by the process, i.e. pre-bent links out of wire rods, meaning that only round cross-section are produced. On the other hand, the LFW chain has no geometry boundaries, since the components are dropforged. Hence, the geometry can be adjusted for every special demand, with special focus on reduced surface pressure and increased wear volume. Figure 3.22 shows schematically the differences of interlink contact of a conventional round link and a LFW *Hero* geometry. The load specific geometry of pewag *Hero* chain has increased interlink contact area and more than twice the wear volume of a conventional chain. This leads to significantly reduced contact and maximum stress, better performance and approximately 30% longer service life.

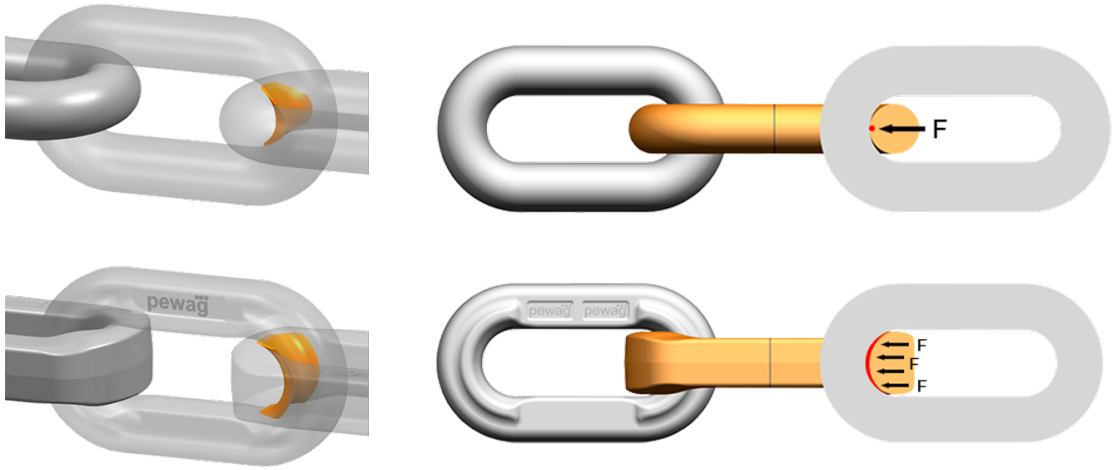

Figure 3.22: Comparison between round and *Hero* links in terms of wear volume increase and surface pressure reduction[112].

3.8.2 Parameter optimization

A systematic analysis using factorial design was conducted to linear friction welded 30CrNiMo8 using as main factors the amplitude, frequency, axial load, and forging load; in order to optimize the process regarding to tensile strength, flash morphology and welding time[113,114]. The results herein presented are normalized and gathered in contour plots (see figure 3.23).

Regarding tensile strength, the amplitude and axial load proved to be the critical parameters. To guarantee exceptional mechanical properties, one can use any amplitude within the investigated range, as long as the axial load is kept at its lower setting. Moreover, for high axial loads a high amplitude is necessary, as depicted in figure 3.23 (a).

The quality of a LFW joint for this particular material can be visually assessed by the morphology of the flash[113,114]. Hence, the flash appearance was categorized in four types, from A to D, for low and exceptional flash morphology, respectively. Once more, the parameters that influence prominently the flash formation are the amplitude and axial load. From figure 3.23(b) a quality flash can be achieved for amplitudes higher than 0.5 at any axial load level.

The welding time is highly dependent on amplitude and frequency. However, unlike the previous outputs the shortest welding time (<3 s) is only possible in a very small range, for high levels of amplitude and frequency, shown in figure 3.23(c).

Finally, the statistical results were evaluated to yield the optimum combination. The results predicted by the optimum combination was successfully confirmed[113].

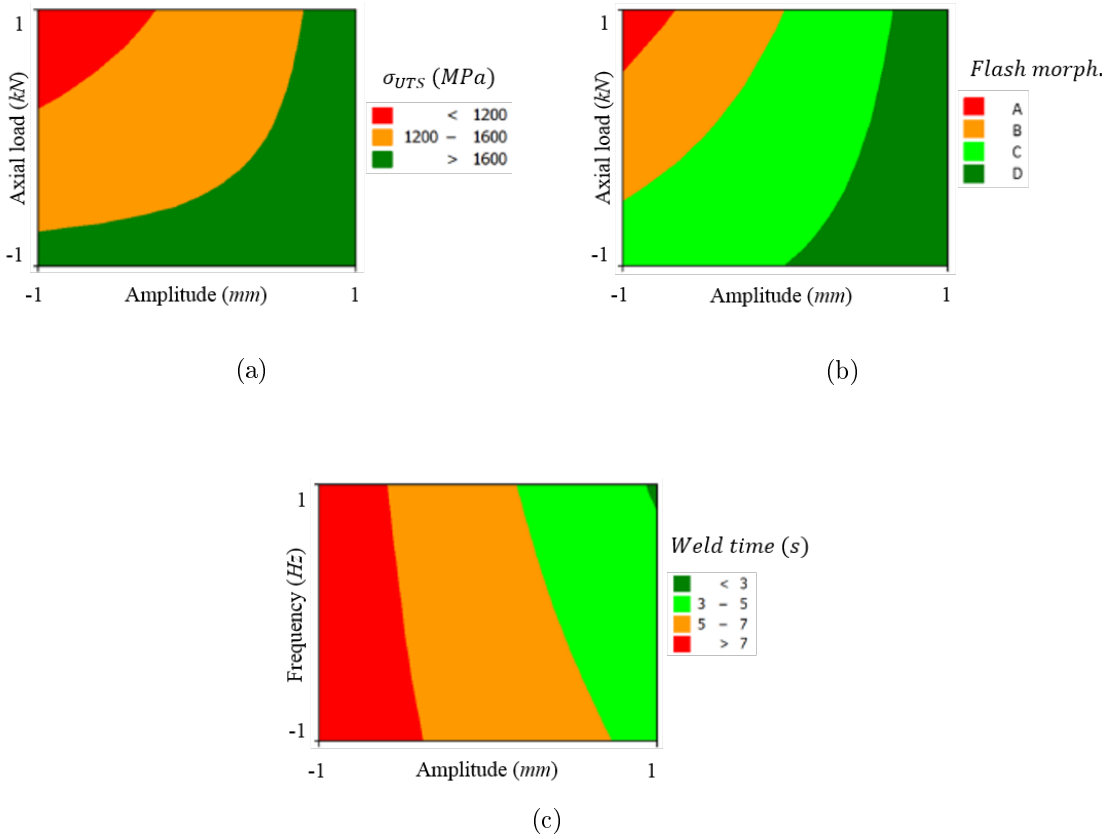

Figure 3.23: Contour plots for: (a) tensile strength; (b) flash morphology; and (c) welding time[113].

3.8.3 Mechanical properties

Tensile testing was already reported in the previous section within the scope of the parameter optimization process. For the optimized parameter combination a significant increase in yield and ultimate tensile strength of 11% and 17.6% compared to the BM, was reported correspondingly. Also, the maximum elongation of the welded joint exceed the BM slightly. The results are summarized in table 3.3.

Sample	σ_y (MPa)	σ_{UTS} (MPa)	ε (%)
BM	1422.7	1516.5	5.75
Welded	1581.5	1783.8	6.14

Table 3.3: Tensile test results for BM and welded specimens[113].

Impact toughness (IT) was also investigated for temperatures between -60°C to 120°C for the base material and -70°C to 150°C including the WZ, using notched specimens with a 45° angle. The superimposed results results are shown in figure 3.24. From the analysis it was concluded that the specimens containing the joint behaved considerably better to crack propagation at sub-zero temperatures. However, the opposite occurred for temperatures above 70°C. A comparable IT was acknowledged for both conditions within 20°C and 50°C. Further testes were conducted with notches specifically positioned in the different zones of the LFW joint. According to table 3.4 the highest and lowest IT were recorded at the WZ and TMAZ, respectively. It is

believed that the low toughness in the TMAZ is related to the highly elongated grain size, compromising the hardness; or temper embrittlement due to slow cooling in the range of 450-650°C.

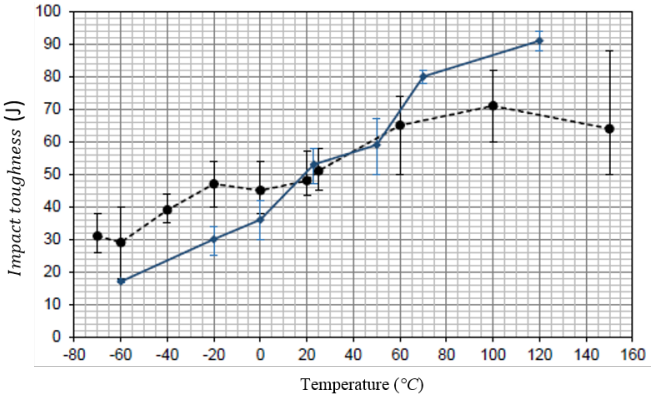

Figure 3.24: Impact toughness comparison between BM and welded specimens[113].

Region	1^{st} measurement		2^{nd} measurement		Total
	Mean	Std. deviation	Mean	Std. deviation	Mean
WZ	47.3	5.6	47.6	2.1	47.4
TMAZ	38.2	0.6	22.3	2.1	30.3
HAZ	32.3	2.5	36.7	5.7	34.5
BM	28.7	2.4	30.3	4.7	29.5

Table 3.4: Impact toughness results for the different regions of the LFW joint[113].

3.8.4 Process modelling

Finite element modelling has firstly been used by Fuchs et al.[115] using MSC Marc software to predict the stresses involved when a reciprocating movement is prescribed to a conventional pre-bent round chain link used in FBW (see figure 3.25(a)). Figure 3.25(b) depicts the model used where one end is firmly clamped while the other has an oscillation movement.

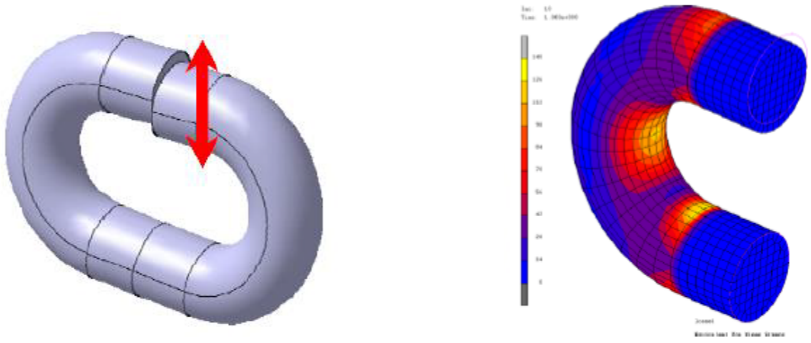

(a) (b)

Figure 3.25: Schematic representation of: (a) conventional pre-bent link as used in FBW; and (b) bended halved links[115].

The results show that localised stress occurs in two specific zones surpassing 140 MPa, ultimately compromising the fatigue life. Based on this result a completely new concept for chain production has been developed and patented[116]. Thus, the conventional pre-bent link was substituted by two bent half links.

Later on, Lopera[117] investigated the thermo-mechanical and thermo-metallurgical outputs of linear friction welded chains, using DEFORM. Although the process consisted on the combined effect of relative motion between the two workpieces, and the applied load, the models built in this work are static, hence there is no oscillation applied. Furthermore, a heat flux function that integrates the effects of the frictional heat was used, as shown in figure 3.26.

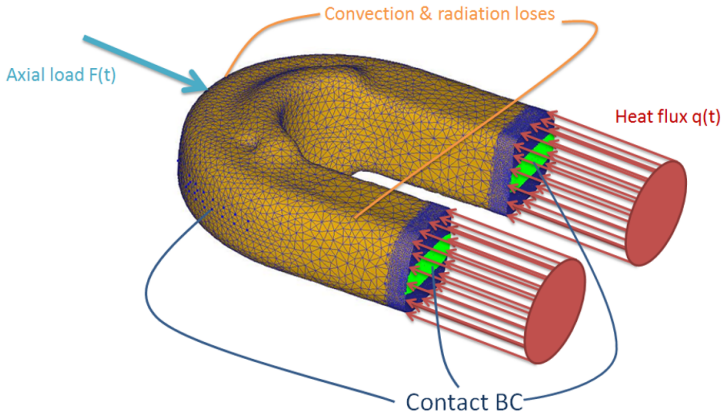

Figure 3.26: Chain model with applied boundary conditions[117].

Heat was estimated via an inverse heat conduction problem (IHCP), from which temperature measurements at different points of the workpiece and at different times during the process were performed, enabling the heat flux to be "back calculated". Moreover, the heat flux on the rubbing surface was determined using a 1D transient heat conduction equation with axial shortening:

$$\rho c_p \frac{\partial T}{\partial t} = \frac{\partial}{\partial x}\left(k\frac{\partial T}{\partial x}\right) - v\frac{\partial T}{\partial x} \tag{3.7}$$

where ρ is the density, c_p is the heat capacity, k is the heat conductivity and $v\frac{\partial T}{\partial x}$ is the convective term accounting for the effect of the axial-shortening v. The heat transfer equation was solved by discretizing the domain using finite differences.

As a result, the developed model provided fairly accurate thermal results. Furthermore, a good agreement was also obtained for the final burn-off between experimental and calculated. However, the burn-off in the initial phase was underestimated due to the lack of plastic deformation exhibited by the model.

Contrastingly, due to the assumptions made, such as of not considering the oscillation movement, the model could not capture the mechanisms and the flash morphology of an actual chain (see figure 3.27). Additionally, this omition in the oscillating movent will have a toal on the strain and strain-rates developed at the interface, as these will be underestimated. The highest values of strain rate are obtained were 30 s^{-1}. The model also does not account for the mechanical mixing, thus the flash in the two links appears separate, instead of one single feature.

As mentioned in the objectives defined in chapter 1, the modelling campaign described in this dissertation also aims to improve some of the shortcomings of these models.

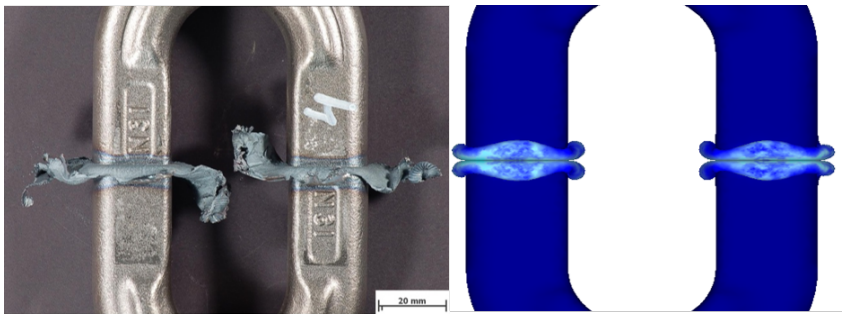

Figure 3.27: Comparison between experimental and predicted flash[117].

Chapter 4

Model description

Commercial Finite Element Method (FEM) based software DEFORM® 11.1 SP1 was used to develop 2D and 3D thermo-mechanically coupled models for transient analysis of LFW process applied. In this chapter, the fundamentals of the used approach are discussed.

4.1 Scope and plan

The development of the process model for Linear Friction Welding (LFW) was aimed to provide insight to the process, regarding heat generation, interfacial conditions, and consequently predicting the material flow phenomena.

In a more precise approach from the one presented in section 3.6.2.1, the LFW process is a coupled thermo-mechanicalmechanical-metallurgical problem, where the inertia effects associated with the mass of components also play a relevant role in the energetic equilibrium. To conceptually understand the developed model, figure 4.1 shows a schematic representation on how thermal and mechanical components of the process are related with material evolution behaviour, namely thermal softening, work hardening and metallurgical aspects.

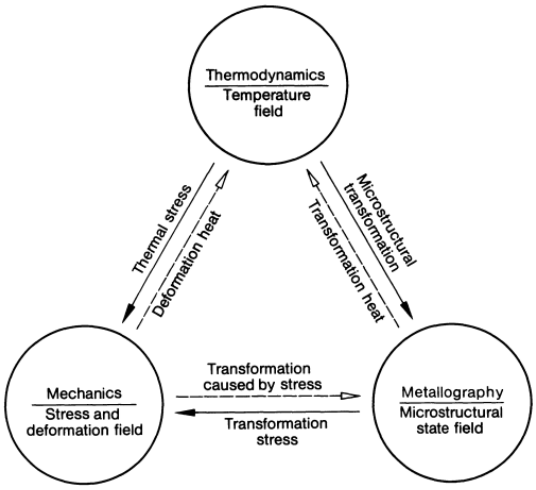

Figure 4.1: Relation and mutual influencing of temperature field, stress and deformation field and microstructural state field[1].

The modelling campaign presented in this dissertation is divided in two fundamental case studies:

1) pewag *Hero*

The first study focuses on the new commercially introduced *pewag Hero* linear friction welded chains, where a 2D and 3D model was developed. The aim is to study the protruding particularities of the LFW process when applied to chains. Hence, the advantages of each model serve as a complement for the analysis and not for comparison amongst them, but rather with the experimental result.

The combination of parameters yielding the best mechanical properties was already optimized using a systematic analysis, documented in previous investigations[14]. Hence, solely one combination is considered in the present study. Due to confidentiality reasons, the absolute values of the welding parameters are not presented.

Finally, the predicted results were evaluated and validated experimentally in terms of thermal histories, flash formation, material flow and residual stresses. As already mentioned, one of the advantages of FEA is that it provides further knowledge on the process. Therefore, the analysis was extended to stress and strain fields, during the process, which cannot be tackled experimentally.

2) Small cross-section

The second study concentrates on the applicability and the gathering of knowledge of the LFW process to join chains with smaller cross-section, mainly towards outputs that cannot be measured experimentally. A systematic analysis using Design of Experiments (DoE) was performed to assess the influence of the process inputs, combining experimental and numerical approaches. The use of DoE has grown rapidly, and a variety of industries have employed this technique to improve products and manufacturing processes[118].

The modelling approach and strategy used is in everything similar to the 2D modelling of the pewag *Hero* that will be described in this chapter, apart from the welding parameters and geometrical characteristics. The type of boundary conditions used are also the same, thus only changing in absolute value.

Confirmation tests were carried out to test the adequacy of the developed models yielded by the DoE study, when subjected to independent and random combinations within the evaluated parameter range.

4.2 Modelling strategy

The modelling campaigns of both aforementioned case studies were carried out using third approach discussed in section 3.6.2.1 . Hence, the process was divided in two distinct stages, consisting of a purely thermal and a thermo-mechanical model. Figure 4.2 depicts schematically the modelling strategy used.

The calculation process begins with the setup of a purely thermal model, that represents the heating by friction in the initial phase of the process, thus serving as an initial thermal boundary condition directly in the thermo-mechanical model. Unlike other studies, the initial phase during the *Hero* chain welding has considerable plastic deformation and is traduced in approximately 2 mm of burn-off. This has to do with the fact that the interfaces of the chains are not flat. Due to the drop forging process the interface of the chain has a ridge and the edges are round. However, for the sake of simplification the deformation on the initial phase was not considered in both 2D and 3D models. The models were ran until a burn-off of approximately 3 mm, which represent the total upset in the equilibrium phase. Contrastingly, for the small cross-section negligible plastic deformation was registered in the initial phase of the process.

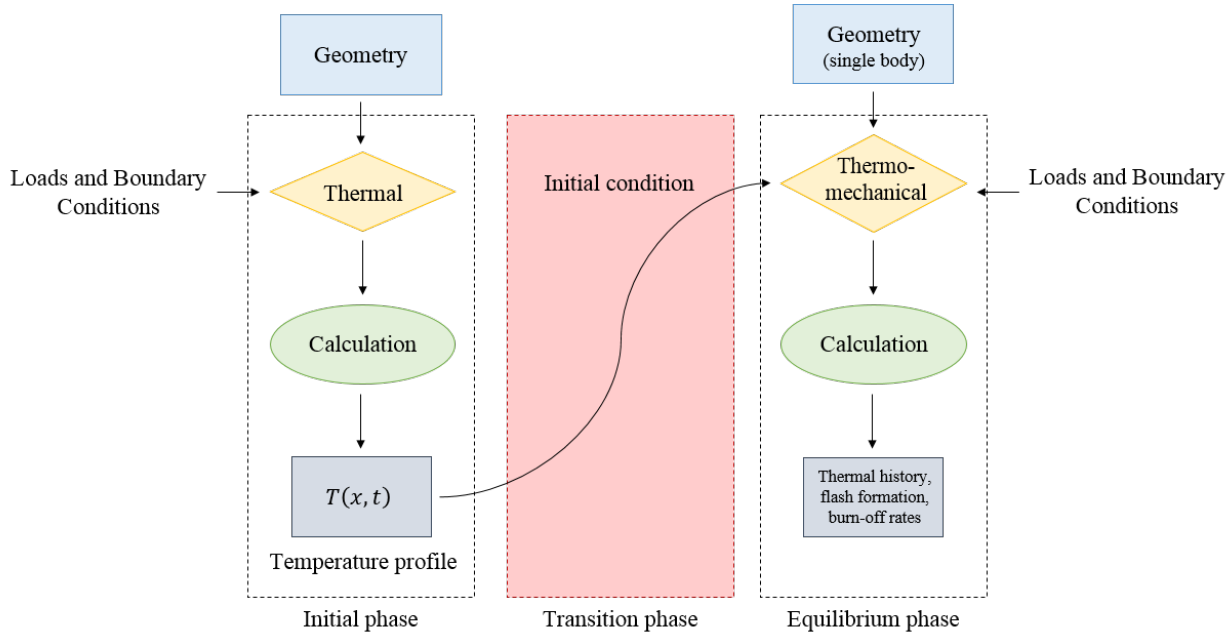

Figure 4.2: Schematic representation of the modelling strategy.

The thermo-mechanical model accounts for plastic deformation in the equilibrium phase, as the quasi-steady state condition is a defining characteristic of this phase. Worth of mention is the "jump" from initial to equilibrium phases, which is explained by the fact that in the transition phase the true contact area increases gradually until total surface contact is established at the end of this phase, hence beginning of the equilibrium phase. For this reason, the "single-body" approach cannot be applied to this stage of the process. As it turns out, the duration of this phase, in comparison to heating and equilibrium phases, is small enough in order

for its effect to be neglected.

4.3 Components of the models

There are three main components which intervene in the models, and these are:

- Plastic workpiece
- Rigid oscillating die
- Rigid forging die

However, the purely thermal model is carried out solely with a single plastic workpiece as there is no mechanical movement involved; whereas the thermo-mechanical model needs two additional dies to account for the mechanical movements of the process. Both dies are modelled as rigid geometric entities to reduce computational time. Additionally, to further reduce computational effort, the interaction between rigid dies and plastic workpiece is done as what is called in DEFORM software as "sticking condition". This entails that the workpieces is rigidly "bonded" to the die in commonly shared nodes.

4.4 Geometries

The first step in model development was to define the geometries for the components of the model. Hence, the geometrical characteristics used for the considered case studies are highlighted.

4.4.1 pewag *Hero*

Figure 4.3 shows the geometrical characteristics of the used dropforged *Hero* half chain links with a cross-sectional width and height of 22 mm and 24 mm, respectively; where x is the oscillation direction, y the forging direction, and z the direction perpendicular to the oscillation. To develop models as efficient computationally as possible, smaller portions of the overall geometry were selected. These are highlighted in red and blue for the 2D and 3D models, respectively.

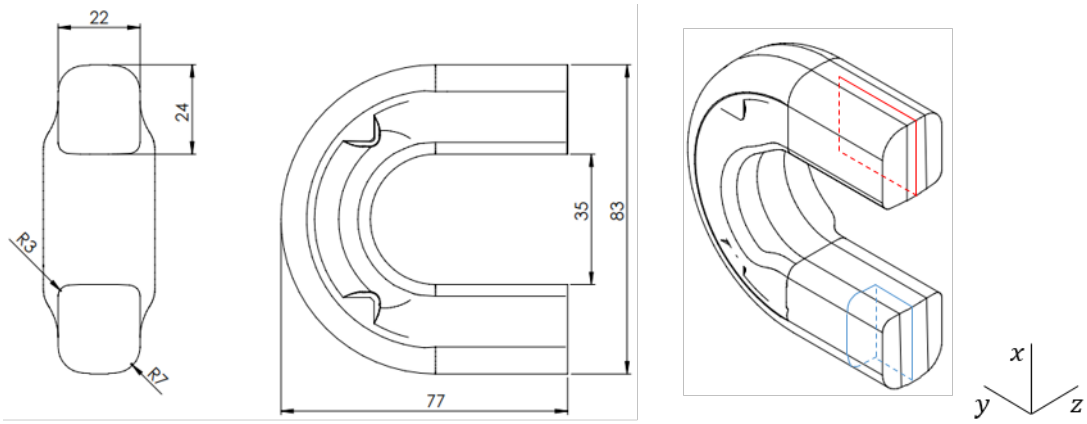

Figure 4.3: Technical drawing of the used *Hero* half chain link, highlighting the portions of the geometry used for the 2D and 3D models in red and blue, respectively.

The dimensional details of the 2D and 3D models are shown in figure 4.4 and 4.5, respectively. The purely thermal geometries represent the mid-section portion of one half link , whereas the geometry of the thermo-mechanical models is a product of simply mirroring the first one with relation to the interface.

The dies of 2D thermo-mechanical model are specifically designed to leave a free length before welding of 16 mm, as encountered in the real clamping system of the LFW machine. Thin design of the dies was considered to reduce as much as possible workpiece-die contact during the flipping movement of the flash, thus impacting negatively the required computational effort, which is not representative of reality

The geometrical setup of the 3D models is slightly different from the 2D one. The extent of the plastic workpiece in the y-direction was reduced to 16 mm, again corresponding to the free length mentioned previously. The dies sit flat to the upper and lower limits of the workpiece, with the same length and width as the latter. Furthermore, the definition of the contact conditions is very difficult to describe. The process is considered to be symmetrical in z-direction, hence the workpiece was reduced to 11 mm. Ultimately, this configuration enables quicker computational times.

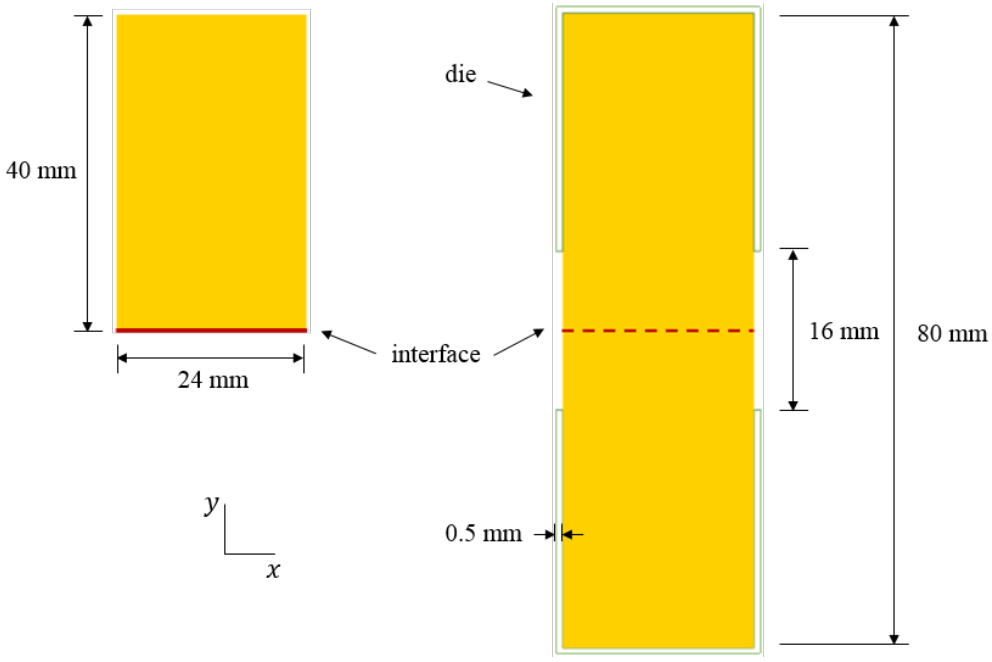

Figure 4.4: Dimensional details of the 2D purely thermal (left) and thermo-mechanical (right) models.

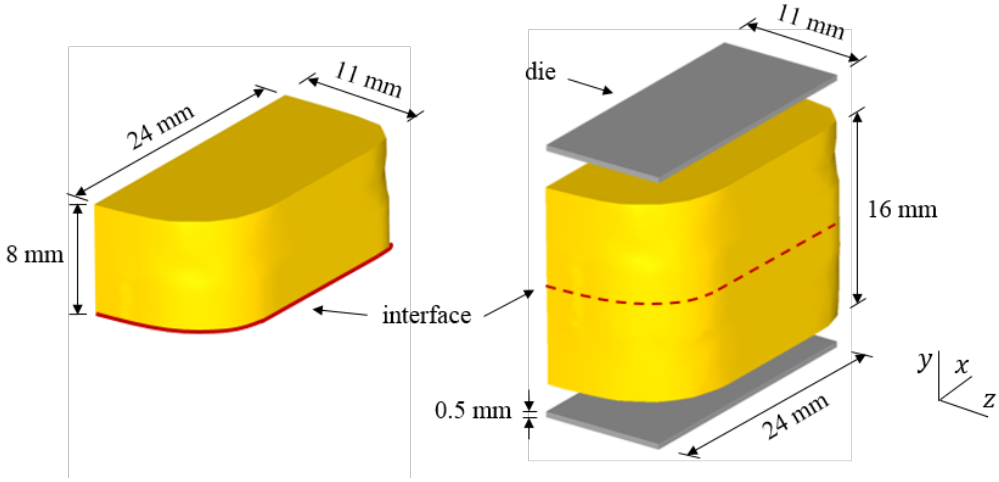

Figure 4.5: Dimensional details of the 3D purely thermal (left) and thermo-mechanical (right, exploded view) models.

4.4.2 Small cross-section

The small cross-section specimen is composed by two rods with different diameters. One part of the rod with 10 mm in diameter, where the actual weld will take place; and the other part with 26.5 mm in diameter and 70 mm in length, purposely made to enable the use of the existing clamping device of the LFW machine. Figure 4.6 illustrates the geometric details of such a sample, along with the portion selected to proceed with 2D analysis is highlighted in red. It is unsound to reduce the present welding procedure to a 2D plain

strain problem due to the circular cross section. Nevertheless, this was deliberated for FEA for the sake of calculation time (approximately 14h for 2D versus 6 weeks for 3D) and amount of parameter combinations produced by the DoE analysis.

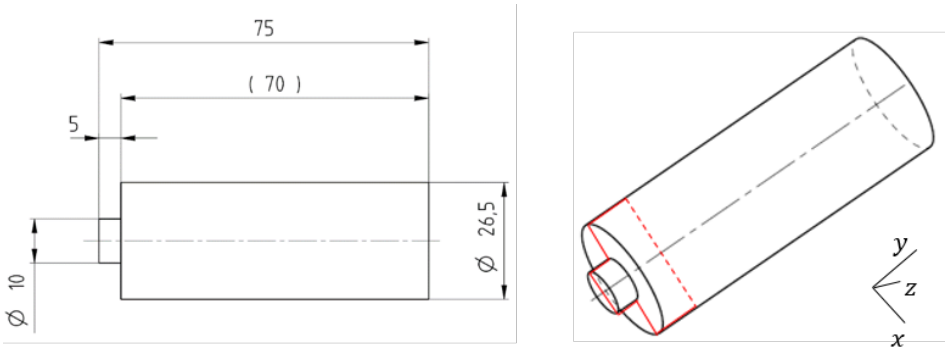

Figure 4.6: Technical drawing of the used small cross-section.

Although the geometry differs from that of an actual chain, it is not anticipated that this will have a major effect on the process/thermal field due to short process duration which results in the thermal field being confined to near the weld interface. The dimensional details of the 2D model are shown in figure 4.7. Similarly to the previous section, the purely thermal geometries represent the mid-section portion of one half link, whereas the geometry of the thermo-mechanical models is a product of simply mirroring the first one with relation to the interface.

The extent of the plastic workpiece in the y-direction is 30 mm, again corresponding to the free surface of the workpiece, "sticking-out" from the clamping system. The dies have the a width and height of 26.5 mm and 0.5 mm, respectively.

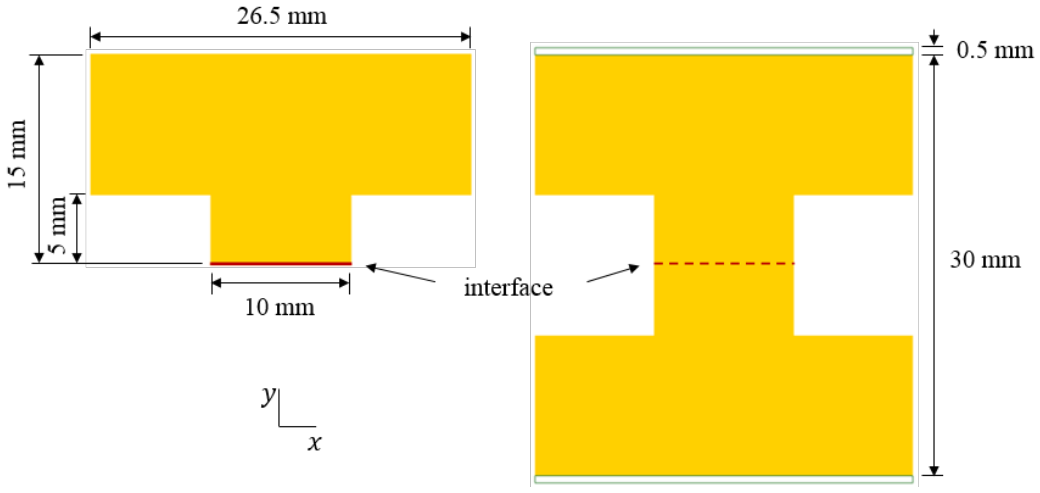

Figure 4.7: Dimensional details of the 2D purely thermal (left) and thermo-mechanical (right) models.

4.5 Meshing characteristics

In LFW most of the heat generation and plastic deformation throughout the process occurs along the weld interface. Thus for the 2D purely thermal models, an average element size of 0.2 mm was used within a 4 mm band around the interface. Outside this region, the element size was gradually increased using 4 additional meshing windows (2 above + 2 below the interface). The mesh of the thermo-mechanical model is obtained by merging and mirroring the purely thermal model along the interface. The mesh appearance is illustrated in figure 4.8(a) and (b) for pewag *Hero* and small cross-section, respectively.

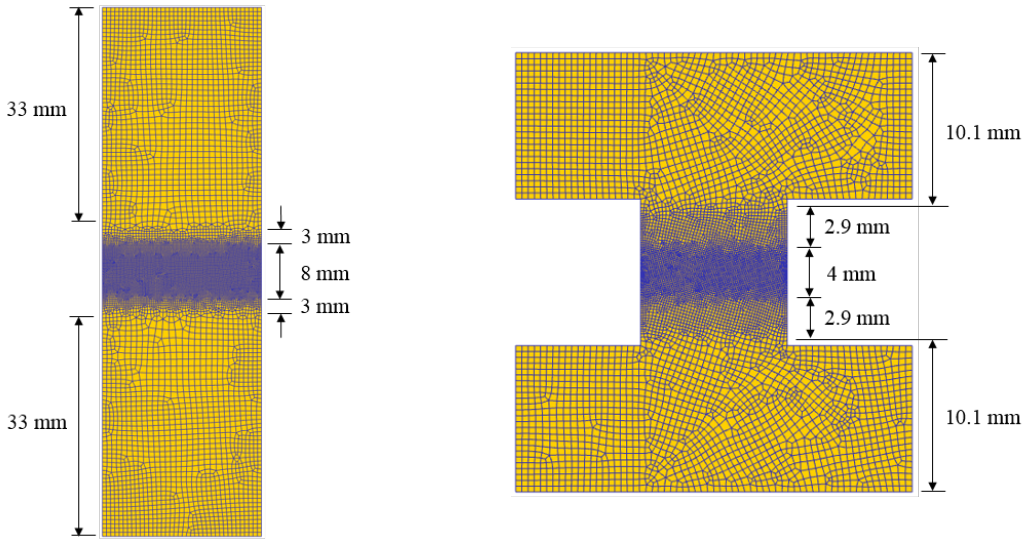

Figure 4.8: Illustration of the mesh used for the 2D thermo-mechanical models: (a) pewag *Hero* (b) small cross-section.

The 3D purely thermal and thermo-mechanical models were discretized using 4-node tetrahedral elements, which besides fitting better the geometry, are more stable for problems dealing with high deformations. Again, the mesh was refined in the areas of interest such as in the vicinity of the welding interface. Hence for the purely thermal model a width band with 3 mm close to the interface was considered, using elements with an average size of 0.5 mm. Similar element sizes were used by Gao et al.[119] and Pashazadesh et al.[120] when modelling friction stir spot and friction stir welding, respectively. The approach described in the 2D model was also carried out to the 3D one. Hence, the mesh used on the thermo-mechanical model is a result of mirror merging the purely thermal model at the interface, and is illustrated in figure 4.9.

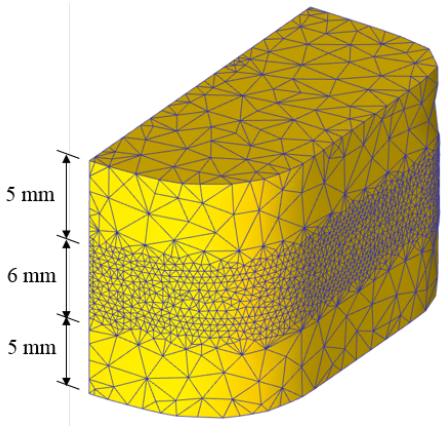

Figure 4.9: Illustration of the mesh used for the 3D pewag *Hero* thermo-mechanical model

4.6 Mathematical formulation

The thermal analysis is governed by the heat equation with a thermo-mechanical heat source term and is given by equation 4.1 [121].

$$\rho c_p \dot{T} = (kT_{,i})_{,i} + \eta \sigma_{ij} \dot{\varepsilon}_{ij} \tag{4.1}$$

where c_p is the specific heat capacity, k the thermal conductivity, σ_{ij} the stress tensor and $\dot{\varepsilon}_{ij}$ is the strain rate tensor. The terms $\rho c_p \dot{T}$ and $(kT_{,i})_{,i}$ represent the internal energy and heat transfer rates, respectively. "$,i$" denotes the differentiation in i-direction. The term η is the related to the fraction of mechanical work that is converted into heat. The energy balance can be rewritten in the variational form as [83]:

$$\int_V kT_{,i}\delta T_{,i} dV + \int_V \rho c_p \dot{T} \delta T dV - \int_S q_n \delta T dS - \int_V \eta \sigma_{ij} \dot{\varepsilon}_{ij} \delta T dS = 0 \tag{4.2}$$

where q_n is the heat flux over the boundary surface S. The term η in the case of the purely thermal model is not considered since there is no plastic deformation. Thus, equation 4.2 reduces to:

$$\int_V kT_{,i}\delta T_{,i} dV + \int_V \rho c_p \dot{T} \delta T dV - \int_S q_n \delta T dS = 0 \tag{4.3}$$

However, η is taken into account in the thermo-mechanical model and assumed to be 0.9. The fraction of the remainder plastic deformation energy is associated with changes in dislocation density, (sub-)grain boundary generation and migration, and phase transformation and evolution [120].

In an FE framework, the energy balance can be discretized into:

$$[C]\left\{\dot{T}\right\} + [K]\{T\} = \{Q\} \tag{4.4}$$

where $[C]$ is the heat capacity matrix, $[K]$ the conductivity matrix, $\{Q\}$ the vector accounting for all thermal sources in the system,$\{T\}$ and $\left\{\dot{T}\right\}$ are the nodal temperature and rate of temperature change, respectively.

The temperature rate at the beginning of a time increment can be obtained according to equation 4.5.

$$\left\{\dot{T}\right\}_i = [C]^{-1}\left(\{Q\} - [K]\{T\}_i\right) \tag{4.5}$$

Deform uses a implicit dynamic numerical method designed for metal forming processes. Thus, the temperature vector can be given by equation[122,123].

$$\{T\}_{i+1} = \{T\}_i + \Delta t\left((1-\beta)\left\{\dot{T}\right\}_i + \beta\left\{\dot{T}\right\}_{i+1}\right) \tag{4.6}$$

where β specifies the time integration factor, which is the forward integration coefficient for temperature integration over time. Its value should be between 0 and 1. The default value of 0.75 is adequate for most simulations[124].

Regarding the mechanical analysis, rigid-viscoplastic finite element approach was considered using the variational principle.

The rigid-viscoplastic material is an idealization of an actual one, by neglecting the elastic response. The rigid viscoplastic material, which was introduced for the analytical convenience, simplifies the solution process with less demanding computational procedure. Moreover, it seems that the idealization offers excellent solution accuracies due to the negligible effects of elastic response at large strain in the actual material. Hence, this simplification is especially suitable for metal forming analysis at high temperatures, in which LFW is included[125].

The variational approach requires that among admissible velocities u_i that satisfy the conditions of compatibility and incompressibility, as well as velocity boundary conditions, the actual solution gives the following functional a stationary value[126]:

$$\pi = \int_V E\left(\dot{\varepsilon}_{ij}\right) dV - \int_{S_F} P_i u_i dS \tag{4.7}$$

where P_i represents surface tractions, and $E\left(\dot{\varepsilon}_{ij}\right)$ is the work function expressed by[127]:

$$E\left(\dot{\varepsilon}\right) = \int_0^{\dot{\bar{\varepsilon}}} \bar{\sigma} d\dot{\bar{\varepsilon}} \tag{4.8}$$

where $\bar{\sigma}$ is the effective stress, and $\dot{\bar{\varepsilon}}$ is the effective strain-rate. The solution of the original boundary-value problem is then obtained from the solution of the dual variational problem, where the first-order variation of the functional vanishes, namely,

$$\delta\pi = \int_V \bar{\sigma}\delta\dot{\bar{\varepsilon}} dV - \int_{S_F} P_i \delta u_i dS = 0 \tag{4.9}$$

with $\bar{\sigma} = \bar{\sigma}\left(\bar{\varepsilon}, \dot{\bar{\varepsilon}}\right)$ for rigid-viscoplastic materials. The incompressibility constraint on admissible velocity fields is removed by introducing a penalized form of the incompressibility in the variation of the functional. Therefore, the actual velocity field is determined from the stationary value of the variation as follows,

$$\delta\pi = \int_V \bar{\sigma}\delta\dot{\bar{\varepsilon}} dV + K\int_V \dot{\varepsilon}_v \delta\dot{\varepsilon}_v dV - \int_{S_F} P_i \delta u_i dS = 0 \tag{4.10}$$

where K is the penalty constant, which should be a large positive value for incompressibility; and is the volumetric strain-rate.

4.7 Energy input analysis

Determining the energy given to the welding interface is of utmost importance to account for the friction component during the initial phase of the process. To that end, a similar approach to the one reported by Ofem et al.[26] is used, provided the fact that the machine is fully instrumented. Using the recordings of in-plane load and displacement recorded by the machine, the energy input can be obtained. However, the load cell does not measure the in-plane load directly at the sample but rather between the clamping and servo-hydraulic system, as depicted schematically in figure 4.10. The instantaneous heat flux at the interface can be computed by,

$$\dot{q}^{"}(t) = \frac{F_{int}^{net}(t)\, v(t)}{A(t)} \tag{4.11}$$

Where $F_{int}^{net}(t)$, $v(t)$ and $A(t)$ is the in-plane load, velocity at the interface and contact area between the half links, at a particular time step, respectively. Applying free body analysis to the system presented in figure 4.10, the load in the interface can be computed by,

$$F_{int}^{net}(t) = F_{int}^{total}(t) - Ma \tag{4.12}$$

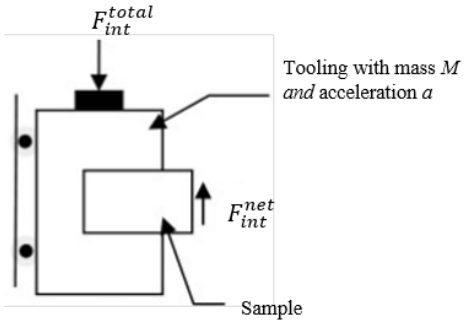

Figure 4.10: Schematic diagram of the oscillating clamping system of an LFW machine[26].

Notwithstanding, the mass M of the oscillatory clamping system is unknown. Hence, the LFW machine was subjected to an unloaded run to account for the inertial movement and internal friction of the tooling system F_{int}^{0}. The load registered was then subtracted from the results obtained when the machine is loaded with a sample and equation 4.12 is rewritten as:

$$F_{int}^{net}(t) = F_{int}^{total}(t) - F_{int}^{0}(t) \tag{4.13}$$

The preceding analysis requires an estimate of the velocity. This can be achieved numerically since the position at discrete values in time is known and the frequency of data acquisition times is approximately 7 times higher than the frequency of oscillation. Thus, the central finite difference is used for the first order derivative[128],

$$v(t) = \frac{|x_{t+\Delta t} - x_{t-\Delta t}|}{2\Delta t} \tag{4.14}$$

where $x_{t-\Delta t}$ and $x_{t+\Delta t}$ denote the positions at a previous and future time levels, respectively; and Δt stands for the time step size.

Finally, the total energy applied at the interface during a certain phase can be obtained as a result of the integration of equation over the phase duration t_{ph}.

$$E_{ph} = \int_0^{t_{ph}} \dot{q}^{"}(t)\, A(t)\, dt \tag{4.15}$$

4.8 Material model

The material used in the present study is a medium carbon 30CrNiMo8 high strength steel. The nominal chemical composition and mechanical properties at room temperature are given in table 4.1 and 4.2, respectively.

Elem.	C	Si	Mn	Cr	Mo	Ni	Fe
%	0.30	0.30	0.50	2.00	0.35	2.00	Bal.

Table 4.1: Chemical composition of 30CrNiMo8 (wt%)[129].

$E\ (GPa)$	$\sigma_y\ (MPa)$	$\sigma_{UTS}\ (MPa)$	$\varepsilon\ (\%)$
210	1050	1250	9

Table 4.2: Mechanical properties of 30CrNiMo8 at room temperature[129].

4.8.1 Flow stress data

To describe the material behaviour in the 2D and 3D models, the tabular format provided by DEFORM software was used, due to its versatility and ability to represent any material. The material flow stress is given as a function of strain, strain-rate and temperature[124].

$$\bar{\sigma} = f(\bar{\varepsilon}, \dot{\bar{\varepsilon}}, T) \tag{4.16}$$

Stress-strain curves were obtained using JMatPro for temperatures, strains and strain-rates up to 1400°C, 4 and 1000 s^{-1}, respectively. Logarithmic interpolation was considered between the defined flow stress data points. Temperature dependent thermal conductivity and heat capacity were also obtained via JMatPro and are also graphically shown in Annex 1.

4.8.2 Phase transformation

Medium carbon steels undergo solid state phase transformations during the heating and cooling cycle which it experiences during the welding process[130,131]. During heating,transformation from the base material of tempered martensite to austenite happens, in the approximate temperature range 830-900°C (at representative heating rates). The material transforms back to (quenched) martensite on cooling, beginning at around 300°C. These transformations are shown schematically in Figure 4.11, where Ac_1 and Ac_3 are

the start and finish temperatures of the transformation to austenite on heating and M_s and M_f are the marstensite start and finish temperatures.

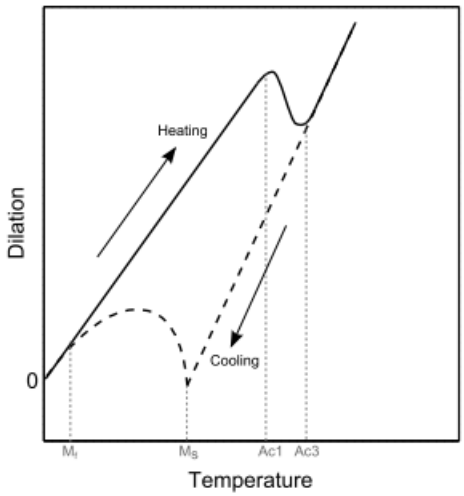

Figure 4.11: Schematic diagram of volume change/dilation due to phase transformations.

In order to predict the thermo-metallurgical changes, phase transformations have been included in the finite element model of the LFW process using the DEFORM-HT add on to the base software to create a triple phase material (martensite, bainite & austenite) that will be used to investigate the transformation between the phases during the weld. After performing a Q&T operation to the half links, the actual 30CrNiMo8 steel is roughly composed of 60% Bainite and 40% Martensite. This composition was employed in the model as the starting structure at room temperature.

In the present study, two phase transformation possibilities were considered:

Bainite & Martensite to Austenite

The transformation kinetics is modelled with a simplified diffusion function based on Johnson-Mehl-Avrami-Kolmogorov (JMAK)[132], and is defined by the following equation:

$$\xi_J = 1 - exp\left\{A\left(\frac{T - T_s}{T_e - T_s}\right)^D\right\} \tag{4.17}$$

The coefficients of the function, A and D set by dilation-temperature diagrams, along with T_s and T_e, the transformation start and end temperatures respectively, have been carried over from literature[133] and are summarized in table 4.3.

Parameter	Value
A	-4
D	2
T_s	600
T_e	900

Table 4.3: Coefficients to define solid state phase transformations used in the simplified diffusion function[133].

Austenite to Martensite

The transformation kinetics to martensite during cooling are modelled using Magee's martensitic transformation function:

$$\xi_m = 1 - exp\left\{\psi_1 T + \psi_2 \left(C - C_0\right) + \psi_{31}\sigma_m + \psi_{32}\bar{\sigma} + \psi_4\right\} \tag{4.18}$$

where σ_m and $\bar{\sigma}$ are the mean and effective stresses, respectively. For the purpose of this work it is assumed that there is no dependency on the carbon content, due to the short time at high temperatures during the welding, or stress on the martensite transformation and therefore ψ_2, ψ_{31} and ψ_{32} take a value of 0 and equation 4.18 reduces to:

$$\xi_m = 1 - exp\left\{\psi_1 T + \psi_4\right\} \tag{4.19}$$

ψ_1 and ψ_4 are identified, provided the fact that the temperatures for for 50% and 90% martensite are known.

Parameter	Value
ψ_1	0.0191
ψ_4	-5.7308

Table 4.4: Coefficients to define solid state phase transformations used in the Magee's function.

4.9 Loads, boundary and initial conditions

The main prescribed loads, boundary and initial conditions intervening in the 2D/3D thermal and thermo-mechanical models are summarised in this section, solely for the pewag *Hero* case study. The reader should bare in mind that the loads and boundary conditions applied in the small cross-section case are analogous to the 2D pewag *Hero* case. Notwithstanding, the key differences from one to the other are pointed out through this section.

4.9.1 Thermal model

The thermal models account for the effect of frictional heat during the initial phase of the process. The developed 2D and 3D models are analogous, differing slightly in the way heat input is applied at the interface.

In either models the heat flux is computed using equation presented in section 4.7 and is referred in figure 4.12(a) as $\dot{q}^{"}$. The heat flux is uniformly applied across most of the interface and lineally reduced to 50% of this value from a distance away from the edge, corresponding to the amplitude, as depicted in figure 4.12(b). This reduction represents the effect of the oscillatory movement, where the offset between the workpieces means a lower heat input in the regions of the edges.

Emissivity was kept at default setting in both models, hence 0.7. The convective heat transfer (h) between the workpiece and the surroundings assumed to be 20 W/m^2K[119], consistent with free convection in air. An initial condition of 20°C was set for the bulk temperature (T_{bulk}). The medium temperature (T_m) was also given the same temperature.

The purely thermal model does not possess self-regulatory properties, hence a truncation temperature had to be applied to avoid the temperature of the elements at the interface climbing over the melting point, as a result of the applied heat flux. The model was ran until $1.5s$, which corresponds to the end on the initial

phase and all interface elements reached 1000°C. The resulting thermal profile is shown in figure 4.13 and will be used as an initial condition for the thermo-mechanical problem.

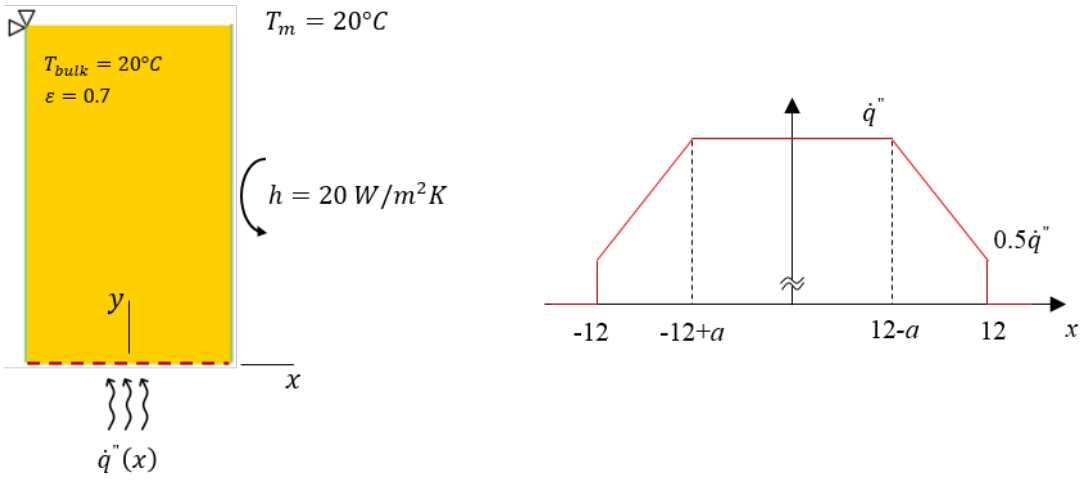

(a) (b)

Figure 4.12: . (a) 2D thermal model boundary conditions; (b) and heat flux profile applied and the weld interface.

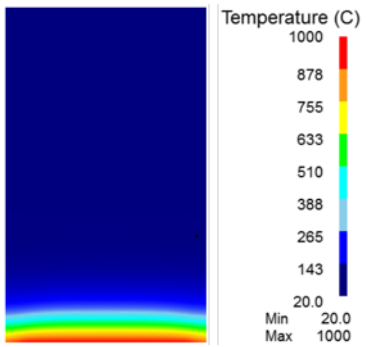

Figure 4.13: 2D thermal profile generated in the end of the initial phase, serving as initial condition for the thermo-mechanical model.

Similarly to the 2D model, the heat flux was uniformly applied across most of the interface, represented by the surface on the underside of the workpiece in figure 4.14(a). Notwithstanding, the heat flux was not linearly reduced away from the edges, corresponding to the amplitude a. Instead, a single step approach was used, where 50% of the value of $(\dot{q}'')$ was used for half the amplitude near the edges. In order to maintain the mean energy due to contact/no-contact condition, 100% of $(\dot{q}'')$ was considered for the remaining half of the amplitude value. Thus, the heat flux was applied as illustrated in Figure 4.14(b). Another simplification to the thermal model was considered by not assuming the influence of the rounded edges in the overall interface contact throughout the process, hence the same heat flux profile was used in every point in the direction perpendicular to oscillating movement.

Due to the considerably smaller extent of the workpiece in the y-direction compared to the 2D model, conduction heat transfer $(k\,(T))$ is allowed on the upper surface of the workpiece. The change in thermal

conductivity as a function of temperature is shown in Annex 1.

The convective heat transfer (h) between the workpiece and the surroundings is highlighted in green, wrapping all around the lateral surface of the workpiece. Its value, along with emissivity, bulk and medium temperatures remain the same as in the 2D model.

The model was ran until $1.5s$ and the appearance of the generated thermal profile is depicted in figure 4.15.

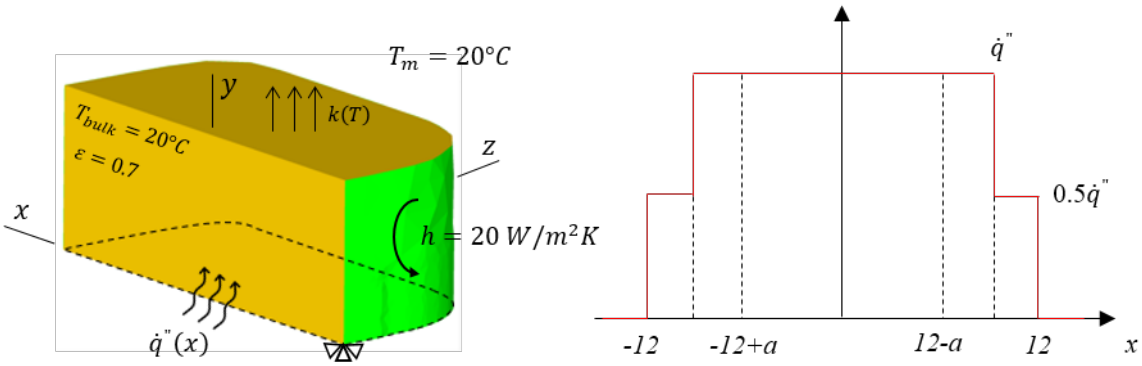

(a) (b)

Figure 4.14: (a) 3D thermal model boundary conditions; (b) and heat flux profile applied and the weld interface.

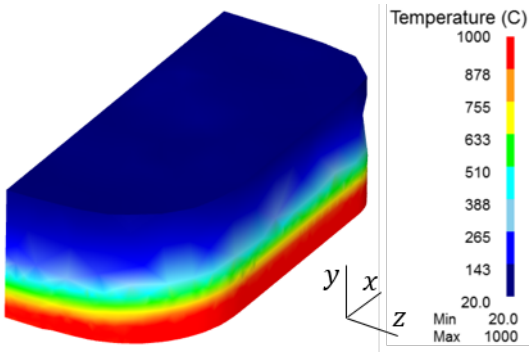

Figure 4.15: 3D thermal profile generated in the end of the initial phase, serving as initial condition for the thermo-mechanical model.

4.9.2 Thermo-mechanical model

The thermo-mechanical models are set up using a plastic workpiece and two rigid dies. As previously mentioned, the temperature profile obtained from the thermal model described in the previous section was mapped onto the plastic workpiece, and serves as an initial boundary condition. This is pictorially demonstrated in figure 4.16.

The reciprocating movement is defined for the upper die by means of what is called in DEFORM as a "path function". This allows to describe the velocity of the harmonic movement in discrete time steps. Thus

$$\overrightarrow{v_x} = a\omega \cos(\omega t) \tag{4.20}$$

where a is the amplitude and ω the angular frequency, which can also be written as $\omega = 2\pi f$ being f the frequency.

In DEFORM, 2D plain strain is modelled considering 1 unit length in the thickness direction (z-direction) [124], thus 1 mm. Thus, the axial load had to be readjusted accordingly to the geometric characteristics of the 2D model, i.e. an interface with a surface area $S_{2D} = 24mm^2$. After some mathematical manipulation, the axial load assigned to the lower die is denoted by F, as shown in figure 4.16(a).

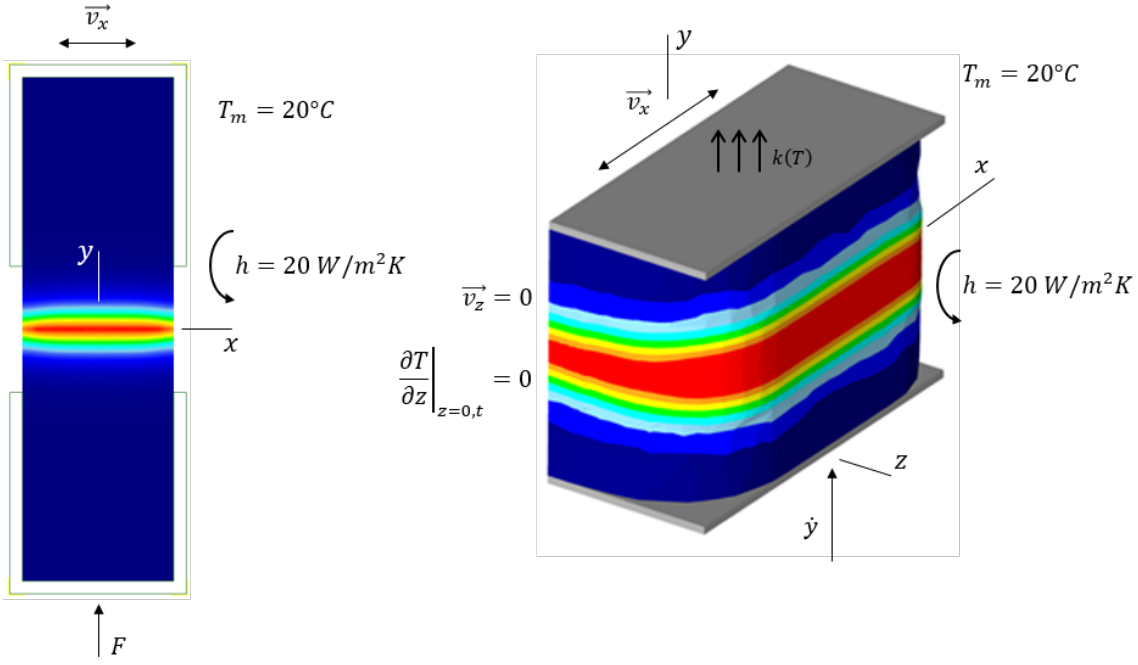

Figure 4.16: Thermo-mechanical model showing a plastic single workpiece with a mapped thermal profile and applied boundary conditions: (a) 2D model; and (b) 3D model.

Natural convection (h) between the workpiece and the surroundings was assumed to be 20 W/m^2K for the sake of simplicity. This is a rough assumption since this is a forced convection problem, with temperature dependence near the weld interface. However, the equilibrium phase lasts approximately $0.9s$, hence its influence is considered to be negligible. Additionally, due to the extent of the workpiece, brevity of this phase and the heat being largely concentrated near the weld line, conduction heat transfer between workpiece and dies was not considered. The medium temperature (T_m) is set to 20 °C.

The 3D thermo-mechanical setup is analogous to 2D, apart from the fact that in the lower die the experimental data of burn-off movement ($\dot{y}$) is used rather than load, as shown in figure 4.16(b). This approach enables the possibility to exploit the advantages of the Conjugate Gradient Solver, which, according to the DEFORM users' manual, computationally more advantageous in terms of reduction of simulation time and storage [124]. Thermal symmetry and no material flow was assumed at the mid-section of the workpiece, hence $\frac{\partial T}{\partial z}\Big|_{z=0,t} = 0$ and $\overrightarrow{v_z} = 0$.

4.10 Solving strategy

Selecting the appropriate solver is an important task when working with FEM to guarantee a smooth convergence of the solution within acceptable computational time and effort. Hence, the solving strategies used for 2D and 3D modelling, along with some pithy explanatory remarks on how they work, are herein presented.

4.10.1 2D model

Regarding 2D modelling DEFORM provides two solvers for temperature and deformation calculation: *Sparse* and *Skyline*. The Skyline method was used as solving method for both thermal and deformation calculations as it provides significant storage and processing advantages over the *Sparse* solver. This method is useful for banded symmetric matrices, which are commonly seen in the FEA with an appropriate node numbering form. The scheme stores the non-zero cells of a matrix entry at the beginning and end of each column in the second-line array. However, in the case, the non-zero elements are located around the main diagonal, and the global stiffness matrix is created in a certain numerical order; an arithmetical logic can be proposed, in which the second-line array could be removed. Consequently, one can apply a series of simple mathematics rules when solving linear equations while keeping the self-determining property of the computational process. According to the following example, here the stiffness matrix **K** can be stored in a single-dimensional array or in a single column vector. To do this, the diagonal entries of the matrix must be stored in an array[134].

$$\mathbf{K} = \begin{bmatrix} a_{11} & 0 & a_{13} & 0 & 0 & 0 \\ & a_{22} & 0 & a_{24} & 0 & 0 \\ & & a_{33} & 0 & 0 & 0 \\ & & & a_{44} & a_{45} & 0 \\ & symm & & & a_{55} & a_{56} \\ & & & & & a_{66} \end{bmatrix} \tag{4.21}$$

Next the envelope of **K** is defined as follows. From each diagonal entry move up the corresponding column until the last non-zero entry is found. The envelope separates that entry from the rest of the upper triangle. The remaining zero entries are conventionally removed:

$$\mathbf{K} = \begin{bmatrix} a_{11} & & a_{13} & & & \\ & a_{22} & 0 & a_{24} & & \\ & & a_{33} & 0 & & \\ & & & a_{44} & a_{45} & \\ & symm & & & a_{55} & a_{56} \\ & & & & & a_{66} \end{bmatrix} \tag{4.22}$$

What is left constitutes the *Skyline* profile or *Skyline* template of the matrix. A *Sparse* matrix that can be profitably stored in this form is called a *Skymatrix* for brevity. Notice that the skyline profile may include zero entries.

Finally the one dimensional *Skyline array* can be written as:

$$\mathbf{s} = \begin{bmatrix} a_{11} & a_{22} & a_{13} & 0 & a_{33} & a_{24} & 0 & a_{44} & a_{45} & a_{55} & a_{56} & a_{66} \end{bmatrix} \tag{4.23}$$

4.10.2 3D model

As highlighted previously, the DEFORM user's manual highly recommends the use of the Conjugate Gradient (CG) Solver for 3D simulations, since it is computationally more advantageous in terms of reduction of simulation time and storage. This solver is usually implemented as an iterative algorithm and applicable to sparse systems which are too large to be dealt by direct implementation or other direct methods, being effective for systems of the form[135]:

$$\mathbf{A}\mathbf{x} = \mathbf{b} \tag{4.24}$$

where x is an unknown vector, $\mathbf{b}$ is a known vector, and A is a known matrix, square $(n \times n)$, symmetric $\left(\boldsymbol{A}^{\top} = \boldsymbol{A}\right)$, and positive-definite $\left(\mathbf{x}^{\top}\mathbf{A}\mathbf{x} > 0\right)$ for all non-zero vectors x in $\mathbb{R}^n$.

By selecting carefully the conjugate vectors $\mathbf{p}_k$ a good approximation to the solution $\mathbf{x}_*$ can be obtained. Starting with $\mathbf{x}_0$ as an initial guess for $\mathbf{x}_*$, one needs a metric as a way to assess the proximity to the actual solution, which is also the unique minimiser for the following quadratic function:

$$f(x) = \frac{1}{2}\mathbf{x}^{\top}\mathbf{A}\mathbf{x} - \mathbf{x}^{\top}\mathbf{b}, \qquad x \in \mathbb{R}^n \tag{4.25}$$

The existence of a unique minimiser is likely as its second derivative is symmetric positive-definite matrix.

$$\frac{d^2}{dx^2}\left[f(x)\right] = \mathbf{A} \tag{4.26}$$

Furthermore, the first order derivative solves the initial problem, such as

$$\frac{d}{dx}\left[f(x)\right] = \mathbf{A}\mathbf{x} - \mathbf{b}, \qquad when\ \frac{d}{dx}\left[f(x)\right] = 0 \tag{4.27}$$

This implies taking the first basis vector $\mathbf{p}_0$ to be the negative of ∇f at $\mathbf{x} = \mathbf{x}_0$, where $\mathbf{x}_0$ is an initial guess, and hence $\mathbf{p}_0 = \mathbf{b} - \mathbf{A}\mathbf{x}_0$. The other vectors in the basis will be conjugate to the gradient. Moreover, $\mathbf{p}_0$ is also the residual provided by this initial step of the algorithm.

Let the residual $\mathbf{r}_k$ at the k^{th} step be given by:

$$\mathbf{r}_k = \mathbf{b} - \mathbf{A}\mathbf{x}_k \tag{4.28}$$

From previous reasoning, $\mathbf{r}_k$ is the negative gradient of f at $\mathbf{x} = \mathbf{x}_k$, so the gradient descent method would suggest to proceed in direction $\mathbf{r}_k$. However, in the CG method one insists the directions $\mathbf{p}_k$ to be conjugate to each other. This condition can be enforced by requiring that the next search direction be yielded from the current residual and all preceding search directions. Hence,

$$\mathbf{p}_k = \mathbf{r}_k - \sum_{i<k} \frac{\mathbf{p}_i^{\top}\mathbf{A}\mathbf{r}_k}{\mathbf{p}_i^{\top}\mathbf{A}\mathbf{p}_i}\mathbf{p}_i \tag{4.29}$$

Considering this direction, the upcoming optimum location is given by:

$$\mathbf{x}_{k+1} = \mathbf{x}_k + \alpha_k \mathbf{p}_k \tag{4.30}$$

where

$$\alpha_k = \frac{\mathbf{p}_k^\top (\mathbf{b} - \mathbf{A}\mathbf{x}_k)}{\mathbf{p}_k^\top \mathbf{A}\mathbf{p}_k} = \frac{\mathbf{p}_k^\top \mathbf{r}_k}{\mathbf{p}_k^\top A \mathbf{p}_k} \tag{4.31}$$

and the second term follows the definition of $\mathbf{r}_k$. α_k can be obtained substituting $\mathbf{x}_{k+1}$ into f and minimizing with respect to α_k.

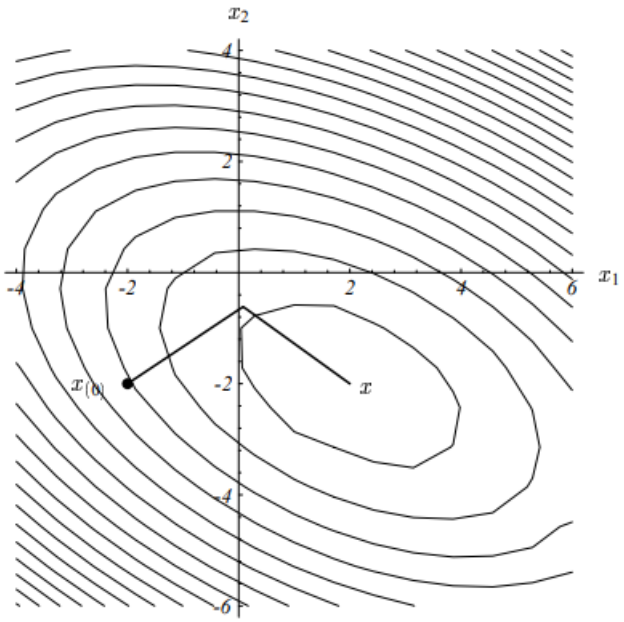

Figure 4.17: Schematic example of the method of Conjugate Gradients. [135]

4.11 Mesh control and distortion

DEFORM is able to automatically remesh the deformed regions of the domain whenever the solver cannot converge to a solution in a time step. This is particularly useful when coping with the problems of large plastic strain, for instance, the heavy plastic deformation near the weld interface.

Each model was given a time-step, Δt, to ensure only a half of the element length was travelled during the reciprocating motion, per iteration.

$$\Delta t = \frac{l_e}{2 \cdot |\overrightarrow{v_x}|} \tag{4.32}$$

where l_e is the element length and $|\overrightarrow{v_x}|$ is the absolute velocity of the reciprocating movement.

Lagrangian incremental formulation was used for 2D and 3D modelling.

4.12 Model limitations

The quality of a FEA model is equivalent to the level of detail with which a certain system is described. Despite the considerable effort to replicate the maximum amount of intervening aspects of the LFW process, the developed models hold a number of limitations, some which are listed below.

- ***Deformation in the initial phase***: although the "single body" approach provides a more realistic output toward the material flow behaviour in the equilibrium phase, its limitation lies on the lack of information prior to mentioned phase. This issue is crucial specially for the pewag *Hero* chain since there is plastic deformation during the initial phase of the LFW process, which was not captured. Furthermore, not considering the flash formation in the initial phase will traduce on the thermal balance at the start of the modelling of the equilibrium phase
- ***Plane strain condition***: this assumption used in the 2D models of both case studies hinders the material flow behaviour in the third direction. Furthermore, and particularly with respect to the small cross-section case study which deals with circular geometry, this assumption is unsound from a theoretical stand point.
- ***Heat flux***: the energy was delivered to the weld interface in a very simple and convenient manner. However, it is a product of experimental data limiting its applicability when investigating other parameter combinations. Moreover, regarding the 3D *Hero* chain model, the procedure used to apply the heat flux to the weld interface will generate errors, as it was applied through the whole length of the interface without considering the rounded edges.
- ***Thermal losses***: admittedly using constant thermal boundary conditions, such as convection heat transfer, may deviate the results of the numerical analysis, regardless of the quick nature of the LFW process.

Chapter 5

Procedure implemented for numerical validation

In this chapter a brief introduction to the LFW research-purpose machine, installed at pewag GmbH facilities in Kapfenberg, is made. Additionally, procedural details of the experiments carried out to test the adequacy of the developed models are presented. These include thermal measurements, residual stress measurements, mechanical and metallurgical characterization, all of which carried out at the Institute of Material Science, Joining and Forming (IMAT) - TU Graz.

5.1 The RSM-1 machine

The welds were carried out in a prototype machine fully developed by pewag Engineering GmbH, displayed in figure 5.1. The design and development of machine was based on the required welding parameters obtained during the preliminary investigations at *The Welding Institute* (TWI) and *Schweisstechnische Lehr und Versuchsanstalten* (SLV). In addition to very high forces (about 300 kN) and the ability to perform a reciprocating motion, the machine was developed with a very high degree of accuracy for the straight alignment of the component axis, before the forging phase. Moreover, the system is fully instrumented and allows the measurement of both normal and in-plane forces, as well as displacements during the process[113].

The four main components of the RSM-1 are namely the pulsator, two clamping actuators and upsetting actuator, meet the following technical specifications:

- Maximum amplitude: 3 mm
- Maximum frequency: 100 Hz
- Adjustable friction and forging force of up to 300 kN
- Clamping system with four jaws, whereby the half chain links are held during welding. This system enables the use of machine for a variety of welding tasks, just by changing the clamping jaws.
- Controllable adjustment of the axial shortening of the chain links.

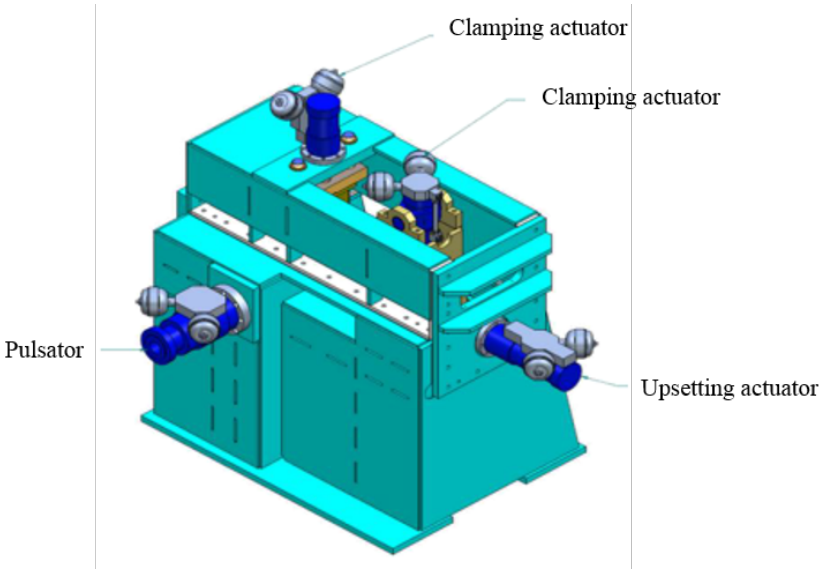

Figure 5.1: RSM-1 Linear friction welding machine[113].

5.2 Thermal measurements

Thermocouple measurements were performed to validate the data provided by the thermal model. To install the k-type thermocouples ($\phi 0.3mm$), one of the links was cut in half and three channels ($\phi 2.5mm$) were milled perpendicular to the oscillation direction and parallel to the axial loading direction, to accommodate the wiring. The equally distance channels were milled until $3.6mm$, $4mm$ and $4.8mm$ from the interface. To secure the terminals in place, epoxy resin was used. The described setup is shown in figure 5.2. Finally, the two halves were joined together and locally TIG welded as far away as possible from the weld interface, to avoid subjecting regions around the interface to thermal cycle and ensure their alignment throughout the process.

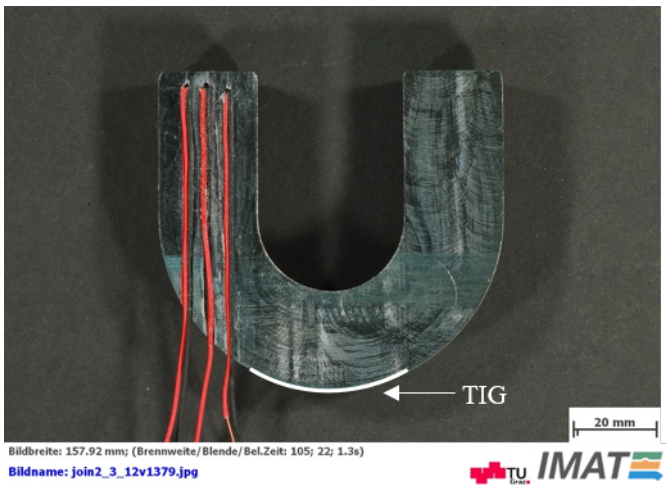

Figure 5.2: Macrograph with the positioning of the K-thermocouples: 3.6 mm (left), 4.0 mm (centre) and 4.8 mm (right) from the interface. The tack welding position is indicated by the white line.

5.3 Mechanical and metallurgical characterization

The Vickers hardness profiles were drawn in the cross section of the joints to evaluate the variations in hardness in the different welding regions. According to the standard ASTM E384-11[136], the indentations were performed at the mid-section, along the axial load direction (y-direction) passing through the welded chain links, with spacing of 0.2 mm between them. The load applied was 1 kgf (HV 1) during 10 s. In order to cover all the microstructural regions, hardness profiles were plotted along an extension of 14 mm or 7 mm for each side of the weld. The measurements were made using an EMCO Duravision G5 machine linked to a dedicated data acquisition software.

Metallurgical characterization was carried out to evaluate the weld quality and geometrical characteristics of the flash using macrographic images light optical microscope (LOM), and ultimately compare with the results yielded by the numerical model. The metallographic procedure here described was carried out in both case studies described in this dissertation.

The welded samples were cut carefully as possible to avoid microstructural modifications and to assure that the cut is made exactly in the centre of the weld. The cutting machine used was a Struers Sectotrom-50®. The samples were hot embedded using Struers DuroFast®, grinded using SiC papers from grade 120 to 4000 and polished with diamond suspension, DiaPro 3μm® and 1μm®, using a Struers Tegramin-30® machine. Moreover, the Struers Teyraforce-5® and Struers Teyrapol-31® holders were used for grinding and polishing, respectively. The samples were rinsed with ethanol to remove the remains of the polishing suspension. Finally, the samples were etched using Nital 5%.

For macroscopic images, the setup at the IMAT Metallography Lab with a special lighting arrangement and 5X magnification capable optical lens was used. The microscopic studies were carried out in a Zeiss Observer – Z1m, paired to a dedicated Zeiss Application Software.

Chapter 6

Results and discussion

This chapter includes all the relevant results from numerical and experimental work for this thesis with reference to the aim of the study, which was the development of numerical models using finite element analysis to provide further insight to the LFW process, specifically applied to chain welding. To that end the two case studies aforementioned will be addressed separately, and thus divided in two main subchapters corresponding to the case studies in hand: pewag *Hero* chain and small cross-sections. Herein are the concluding remarks comprising the main findings and shortcomings.

6.1 Numerical analysis of LFW applied to pewag *Hero*

The present subchapter focuses on the results of the coupled numerical model as a way to comprehend the welding process applied specifically to the *Hero* chain. The importance of this study lies in the advantage of predicting the intervening physical quantities of the process such as temperature distribution, flash formation, burn-off rate, mechanical and metallurgical properties; all of which will be herein discussed. The numerical results were compared and validated for relevant and possibly relatable physical aspects comprised in the analysis.

Worth of mention is the fact that the results of either models were conveniently used to tackle different subjects of the analysis. Hence, the purpose of the 2D and 3D models is not to compare the capabilities of each setup, but rather to complement each other in the analysis.

6.1.1 Thermal analysis

The thermal histories were recorded every 0.5 s at the corresponding upset position to assess the adequacy of the developed models. The experimental upsetting position was used to withdraw the temperature in the models to avoid further uncertainty provided by the slight misfit between experimental and modelled burn-off rate, covered in the upcoming section. The predicted temperatures are presented until the end of the equilibrium phase, as presented in figure 6.1.

From figure 6.1(a) it can be acknowledged that the thermocouple 4 mm from the interface registered higher temperatures than the one closest to the interface. Although the thermocouples are mounted on the

stationary part of the chain, they are under high cyclic stress due to the reciprocating movement and in-plane load. As a result, it is believed that one has moved in relation to the other.

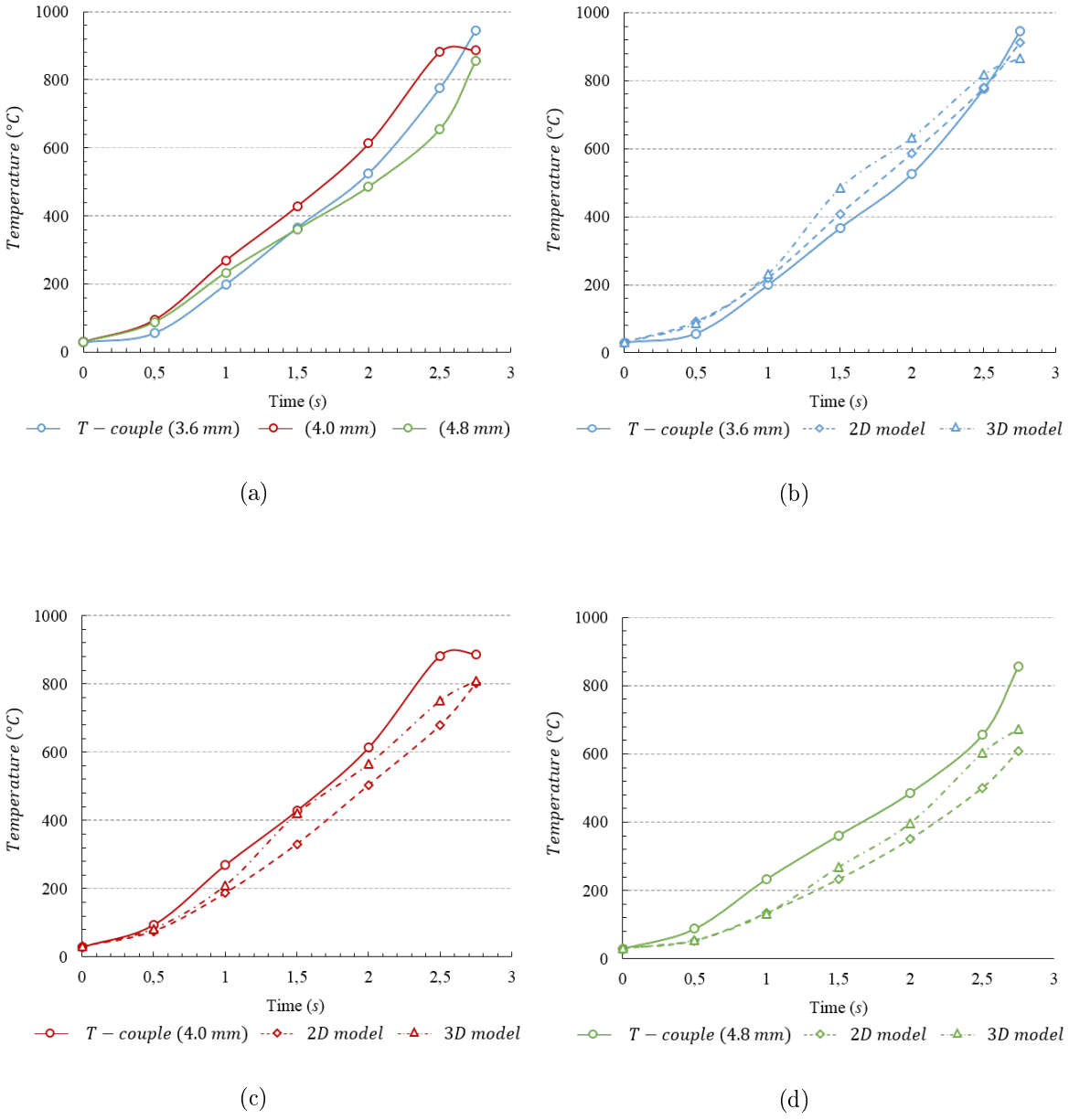

Figure 6.1: Comparison of the thermal histories between: (a) thermocouple measurements; and experiment and models: (b) 3.6 mm; (c) 4.0 mm; and (d) 4.8 mm.

For the thermocouple closest to the interface, good agreement was obtained in relation to the FE models, as shown in figure 6.1(b). From $t = 1\ s$ to $t = 2.5\ s$, the 3D model overestimated the temperature, and a maximum temperature difference of approximately 100°C registered at the beginning of the equilibrium phase (t =1.5 s). Adequate results were also obtained between the thermocouple initially at 4.0 mm and the models, as illustrated in 6.1(c). Both models underestimated the temperature at $t = 2.5\ s$. However, the highest discrepancy is acknowledged in the thermocouple furthest from the interface, although the 3D model

was able to predict more accurately the temperatures throughout the process, despite the differences at the end of the equilibrium phase.

Finally, two effective conclusions can be made from the analysis: i) the temperature trend i.e. the curve gradients are similar; and ii) towards the end of the analysis in all cases the models underestimate the experimentally measured value. This might related with the loss of accuracy for the material model at higher temperatures and strain rates.

6.1.2 Burn-off rate

The interest in studying and predicting the rate of material expelled as flash is of great importance, as it is related to the upsetting process. To that end, a burn-off rate analysis was solely carried out to the 2D model since it is load controlled, whereas the 3D model is stroke controlled (see section 4.9.2). Hence, in the latter case makes no sense to study the burn-off rate.

To evaluate the burn-off throughout the process, point tracking was used, as shown in figure 6.2 specified by P_1. The model predicted a linear axial shortening, typical of the LFW process in the equilibrium phase, where quasi-steady state conditions are achieved in steel. A comparable result is acknowledged, with an average experimental and predicted burn-off rate of 3.08 mm/s and 3.13 mm/s, respectively.

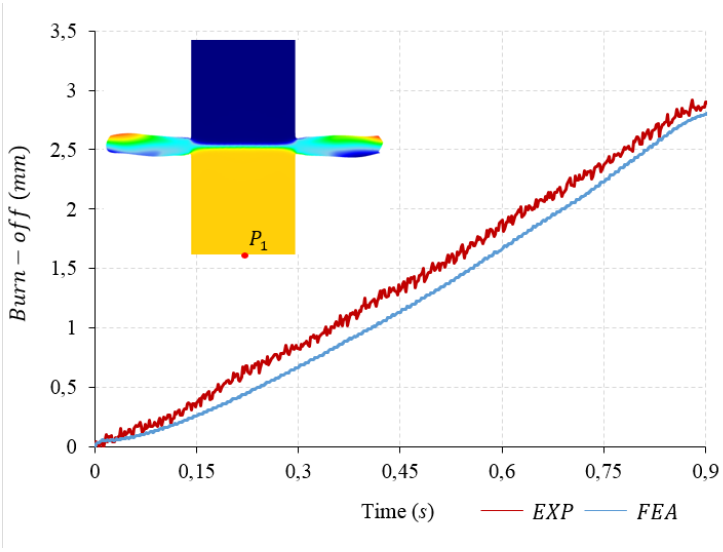

Figure 6.2: 2D FEA axial displacement in the equilibrium phase with point tracking P_1.

Despite the good agreement, it is clear that in the initial instants of the equilibrium phase the model does not upset in the same rate as experimentally, which suggests that the prescribed interface temperature resulting from the purely thermal model is low. Hence, the material flow until $0.25s$ was underestimated. Steady state burn-off is observed throughout the remainder of the equilibrium phase and comparable upset was reached between model and experiment.

This outstanding result supports the adequacy of the developed model in terms of setup, material model and properties, loads and boundary conditions used.

6.1.3 Flash formation

The morphology and formation of the flash is directly related to the mechanisms driving the plastic deformation. Thus, the viscous material is expelled according to two main mechanisms: (i) the axial load steadily extruding the viscous hot layer of material form between the workpieces; and (ii) the oscillatory motion dragging material from the weld line in each stroke of the oscillation. The prevailing effect is linked to the process parameters used, namely amplitude. Thus (i) is associated with low amplitudes, whereas (ii) with high amplitudes. Furthermore, larger oscillation amplitudes produces larger ripples in the flash. The rippling effect is a result of the interaction between viscoplastic material and vertical surface of the workpiece. The vertical surface therefore drags the viscoplastic material during the reciprocating movement, creating a distinct ripple[80].

6.1.3.1 2D model

In the present case the amplitude value is not high enough to shear the viscous material. Hence, mechanism (i) occurs and the extruded material remains in constant contact with the upper and lower workpiece during oscillation. Also, the thermal profile is wide enough to accommodate the difference in strain rates, and flow stresses associated, between the interface and material being sheared by the edge. As a result, a smooth flash without rippling is formed. Figure 6.3 depicts the comparison between the experimental and modelling results for the flash morphology. The experimental flash is characterized by a smooth surface regardless of the small rippling which has not been reproduced by the model, since the element size used is not small enough to capture these features.

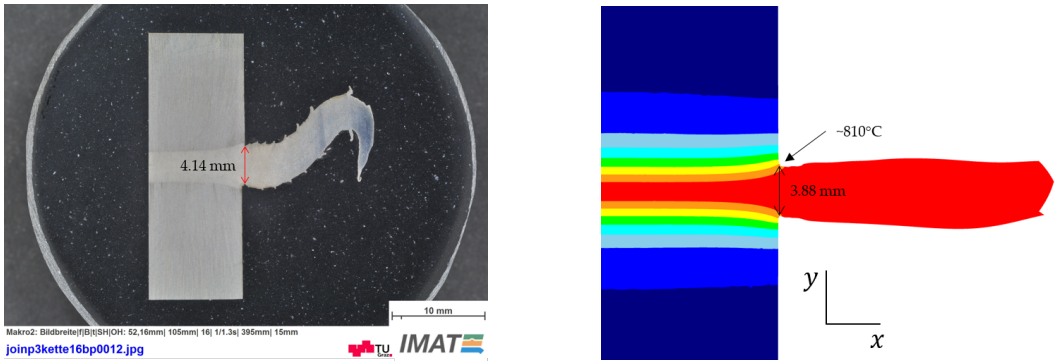

(a) (b)

Figure 6.3: Flash morphology comparison between the (a) experimental and (b) model.

The flash deflects upwards and downwards with the reciprocating movement, reaching its maximum height when the amplitude is at its maximum value. At a certain length, the experimental flash contacts the tooling, causing its tip to divert downwards as shown in figure 6.3(a). This behaviour was not observed in the model since there is no tooling interacting with the flash.

A relatively good agreement was obtained for the flash extrusion thickness, with 4.14 mm and 3.88 mm for the experiment and model, respectively. This difference might be due to model related assumptions, such

as meshing characteristics, heat input data; and material related, like flow stress and heat conductivity data.

Worthy of note, the model showed that the boundary temperature between flash formation and negligible material flow is approximately 810°C, as shown in figure 6.3(b). This temperature corresponds to the Ac3 temperature of this material.

Moreover, the calculated flash shoes a rounded edge, in contrast with the sharp edge obtained in the experiment. This difference can be explained by the geometric properties of the chain links, as they are not completely flat as shown in figure 6.4. As a result, in the initial phase of the process this traduces in higher pressure and local heat input, consequently plasticizing locally the material in the interface.

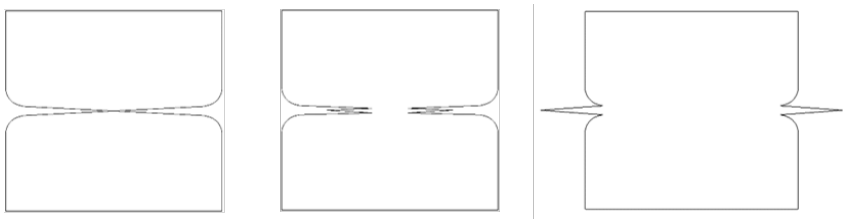

Figure 6.4: Schematic representation of the evolution of the flash formation at the interface of the chain due to the surface of the forged chain link.

6.1.3.2 3D model

Analogous to the 2D flash formation, the extruded material remains in constant contact with the upper and lower parts of the workpiece during the oscillation movement, which characterizes welds with low amplitude, unable to promote shearing. The 3D model is invaluable to understand the multi directional material flow behaviour of the process, and figure 6.5 shows the morphology of the flash mirrored in the z-direction at different time steps.

Figure 6.5(a) shows the flash appearance in the early stages of the process. Also, until approximately $t = 0.35s$, the flash distorts severely upwards and downwards with the oscillating movement. However, at a certain point despite the flipping movement of the flash, a preferential flow towards the moving part is acknowledged and is shown in figure 6.5(b). This tendency might be related due to the constant constraints imposed on the flash by self-contact and tooling contact, promoting local shearing on the base of the flash, which coupled with the pressure increase at high amplitudes redirects the flash to the moving side. Furthermore, the deflection of the flash might also be a product of the tooling effect entitled "micro-swinging". Hence, the moving part of the chain does not move rigidly in the oscillation direction, but has a micro-swing relative to the oscillation plane instead. According to Li et al.[73] micro-swinging has a significant effect of the extrusion manner, as the swinging part ends up digging into the other promoting deflection of the flash from its centre point. On the other hand, negligible effect on the interface temperature at the centre of the weld. This phenomena can also be observed in the experimental flash, according to figure 6.3(a). Notice that the flash near to the extrusion zone also diverts upwards.

A further consequence of the flash extrusion evolution has to do with the self-contact observed at a certain point of the simulation process as the flash contacts the workpiece. As a result, conduction heat transfer occurs locally, causing the uneven cooling of the flash as shown in figure 6.5(c). Moreover, by the end of the equilibrium phase $t = 0.90s$ illustrated in figure 6.5(d), one can intuitively acknowledge that the flash further away from the extrusion zone is locally colder when compared to other regions due to convection and the

influence of conduction from earlier stages.

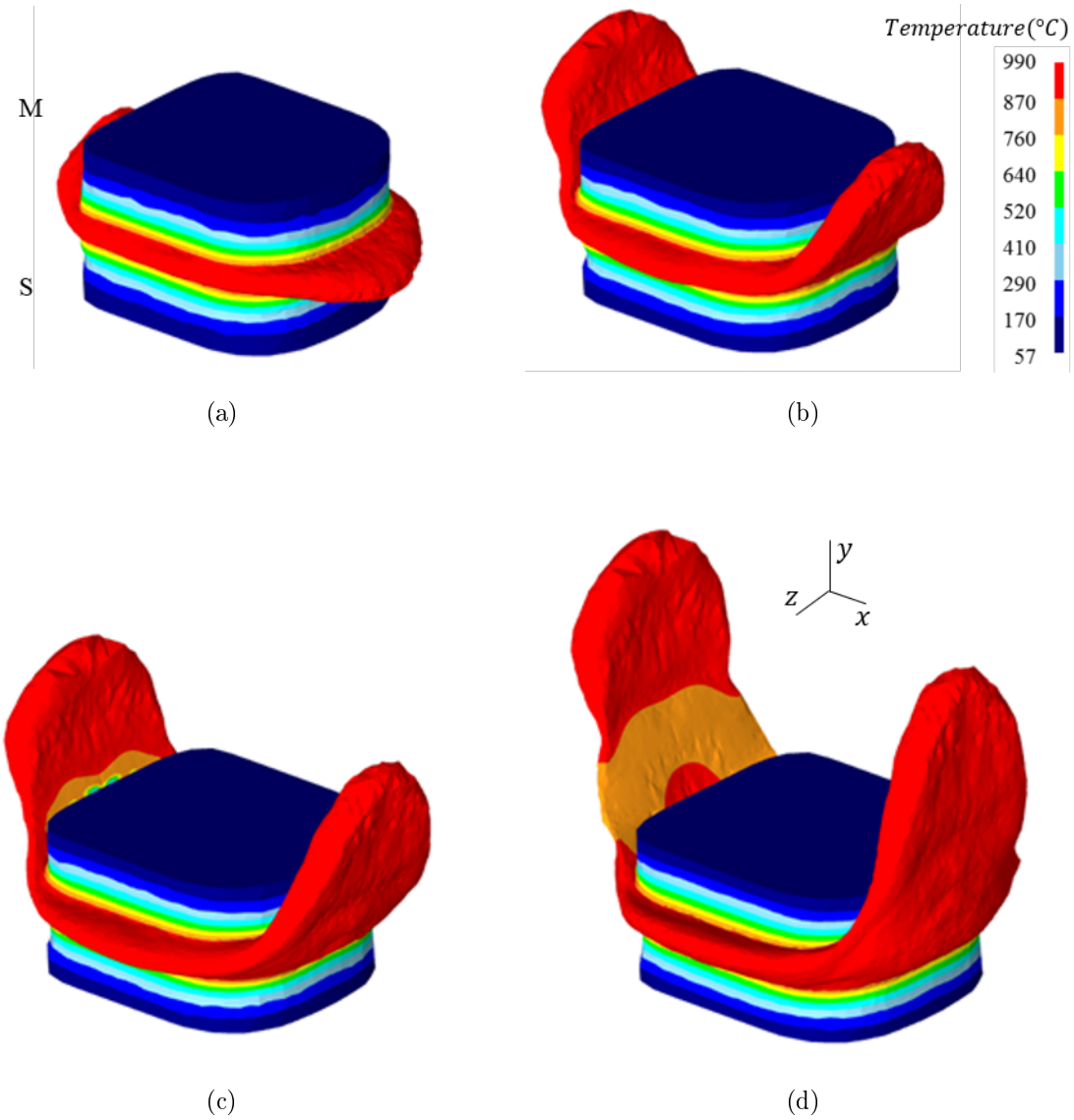

(a) (b)

(c) (d)

Figure 6.5: Appearance of the formed flash through different time steps: (a) $t = 0.25\ s$; (b) $t = 0.5\ s$; (c) $t = 0.75\ s$; and (d) $t = 0.90\ s$. "S" denotes the stationary and "M" the moving component.

6.1.4 Mechanical analysis

One of the advantages of computational modelling is that it enables the possibility to assess the mechanical behaviour of the chain in terms of stress, strain and strain rates, at any given moment of the process. The analysis was conducted for a single time step $t = 0.80\ s$, just before the end of the equilibrium phase. Additional time steps were not considered as the behaviour and magnitude of these three state variables remains virtually unchanged at equivalent time steps throughout the simulation process, due to the periodic characteristics of the oscillatory movement.

6.1.4.1 Stresses

The stress fields were evaluated in terms of effective stress or Von Mises stress σ_{eff}, and principal stresses σ_x and σ_y, presented in figure 6.6 and 6.7. Due to the coarser mesh used in the 3D model the stress field lacks detail compared to the 2D, although qualitatively a good agreement can be acknowledged. The 810°C isothermal dashed lines denote the boundary between regions with plastic flow (WZ) and without (HAZ), as previously stated in subsection 6.1.3.1. The effective stress is given as[137]:

$$\sigma_{eff} = \frac{1}{\sqrt{2}}\sqrt{(\sigma_{xx} - \sigma_{yy})^2 + (\sigma_{yy} - \sigma_{zz})^2 + (\sigma_{zz} - \sigma_{xx})^2 + 6\left(\sigma_{xy}^2 + \sigma_{yz}^2 + \sigma_{zx}^2\right)} \tag{6.1}$$

The stress distribution reveals roughly a symmetrical behaviour along the weld line, although inverted according to the axial direction y. This is explained by the inherent property of the LFW process, in which the relative movement from upper and lower parts of the workpiece occurs in different directions, with same relative speed. Intuitively, the stresses present on the left of the upper part will be present in the lower part on the right and vice versa.

At the WZ, an average compressive stress in the x-direction of 40 MPa was registered, as shown in figure 6.6(b). The low stresses in these regions is related to the viscoplastic condition of the material due high temperatures, which consequently implies lower loads to induce plastic deformation. Furthermore, considering the upper workpiece, the viscoplastic material upstream and downstream from the vertical mid-plane is being "pulled" and "dragged", respectively, by colder regions of the workpiece; resulting in the tensile and compressive stresses towards the TMAZ and HAZ, accordingly. Due to the relative speed between workpieces the opposite happens in the lower workpiece.

According to figure 6.6 and 6.7(c) a relatively uniform compressive stress distribution of 27 MPa was obtained in the y-direction, consistent with the forging load acquired experimentally.

From the experimental point of view, the expected stresses imposed by the tooling on the workpieces are of compressive nature solely. At the evaluated time step, the reciprocating tool is moving from left to right. This explains the compressive stresses found on the left of the upper workpiece at the contact edge where die meets the workpiece, as shown in figures 6.6(b) and (c). Predicted compressive stress of approximately 390 MPa and 440 MPa was predicted for x and y directions, respectively. On the other hand, a tensile contribution is visible in the opposite side for both directions. Additionally, an analogous behaviour can be observed for stresses in the z-direction, according to figure 6.7(d). This is a direct consequence of the rigid coupling (sticking condition) between die and workpieces selected in DEFORM, which is not representative of reality. Thus the tensile stresses arisen are an artefact related to the modelling set up.

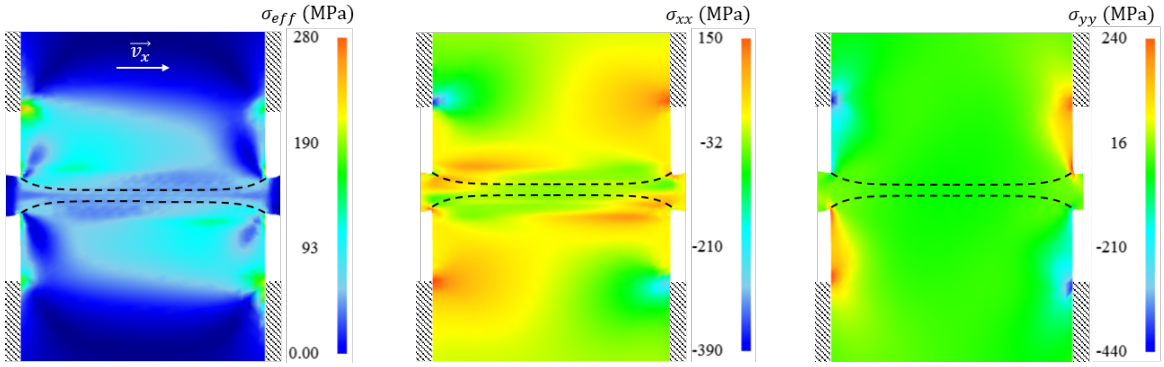

(a) (b) (c)

Figure 6.6: 2D stress fields at $t = 0.80\ s$: (a) effective stress σ_{eff}; (b) in the reciprocating direction σ_{xx}; and (c) in the forging direction σ_{yy} (dashed lines delimit the WZ).

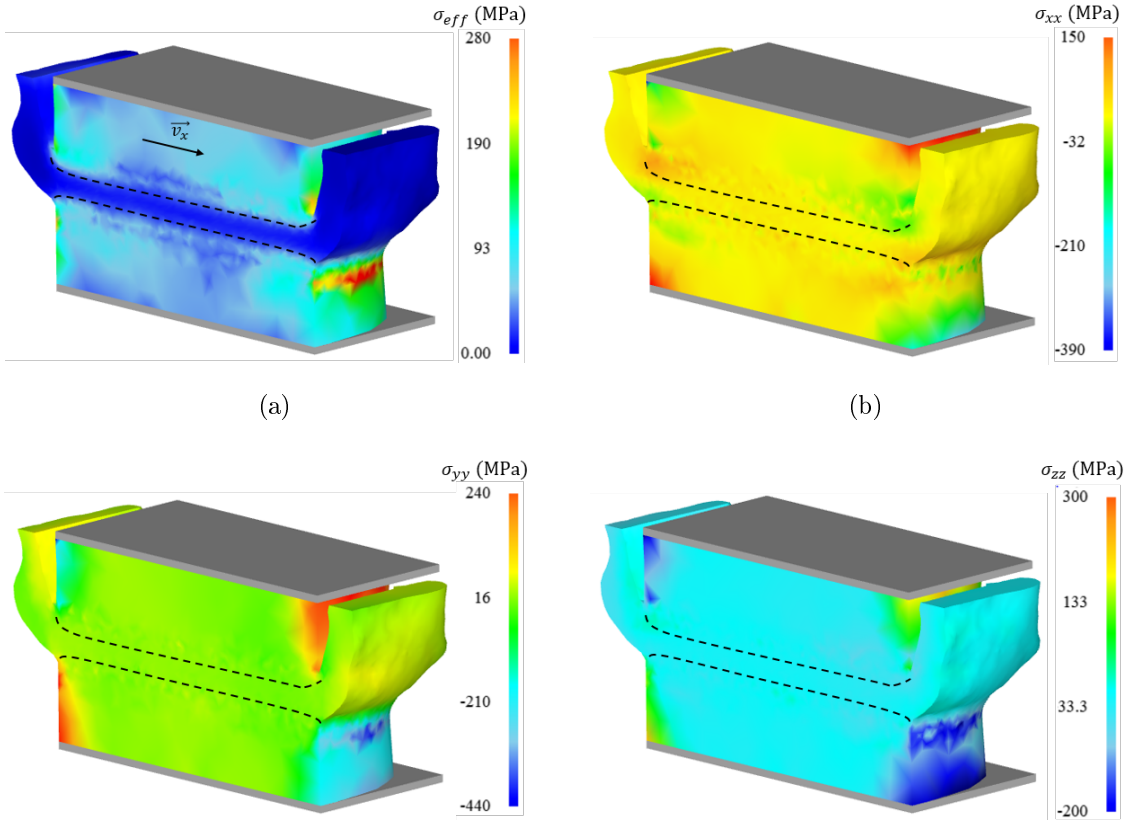

(a) (b) (c) (d)

Figure 6.7: 3D stress fields at $t = 0.80\ s$: (a) effective stress σ_{eff}; (b) in the reciprocating direction σ_{xx}; (c) in the forging direction σ_{yy}; and (d) in the forging direction σ_{zz} (dashed lines delimit the WZ).

6.1.4.2 Strains

Strain is a measure of the degree of deformation in an object[138–140]. The measure of strain used in large deformation analysis, including DEFORM is Hencky strain or true strain, which differs slightly from the well known engineering strain presented in typical engineering applications. Engineering strain is defined as change in length (Δl) by original length (l_0) and is suitable for low deformation applications[141].

$$e = \frac{\Delta l}{l_0} \tag{6.2}$$

For large deformation analysis, it is better to use true strain, which is defined as the sum of a large series of arbitrarily small strain increments integrating this over the total change in length gives[142]:

$$\varepsilon = ln\frac{l_f}{l_0} \tag{6.3}$$

where l_f is the final length.

Through various mathematical techniques which are beyond the scope of this discussion, it is possible to define so-called "principal axes" on which all components of shear strain are zero. The strains measured along these axes are termed "principal strains". It is frequently useful to have a single characteristic strain value to describe the degree of deformation. DEFORM uses a value common to metal forming analysis known as the effective or Von-Mises strain[124,143]:

$$\varepsilon_{eff} = \frac{\sqrt{2}}{3}\sqrt{(\varepsilon_{xx} - \varepsilon_{yy})^2 + (\varepsilon_{yy} - \varepsilon_{zz})^2 + (\varepsilon_{zz} - \varepsilon_{xx})^2} \tag{6.4}$$

where ε_{xx}, ε_{yy} and ε_{zz} are the principal strains.

The effective strain at $t = 0.80\ s$ is shown in figure 6.8 and 6.9. It is clear that the strain is concentrated within a narrow band with its border no more than 2 mm from the weld line.

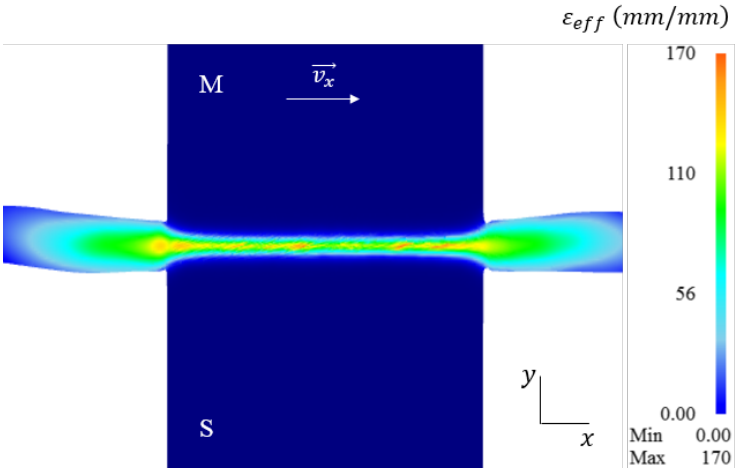

Figure 6.8: 2D effective strain ε_{eff} distributions at $t = 0.80s$.

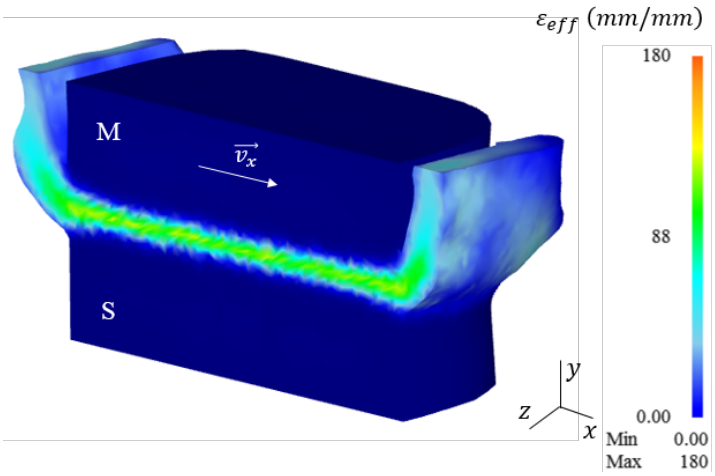

Figure 6.9: 3D effective strain ε_{eff} distributions at $t = 0.80s$.

Due to the steep temperature gradient near the weld interface the material in this region is soft enough and undergoes severe plastic deformation, where a maximum effective strain of 170 and 180 was registered for 2D and 3D models, accordingly.

6.1.4.3 Strain rates

Strain rate is a measure of the rate of deformation with respect to time. The components of strain rate are defined in the same manner as the components of strain. Strain rate is defined as the instantaneous plastic strain rate.

The effective strain rate at $t = 0.80s$ is shown in figure 6.10 and a maximum of 1700 s^{-1} and 2000 s^{-1} was observed on the weld interfaces of the 2D and 3D models, respectively. The predicted values of two normal strain rate components $\dot{\varepsilon}_{xx}$ and $\dot{\varepsilon}_{yy}$ were evaluated along the two vertical lines L_1 and L_2 passing through the weld interface.

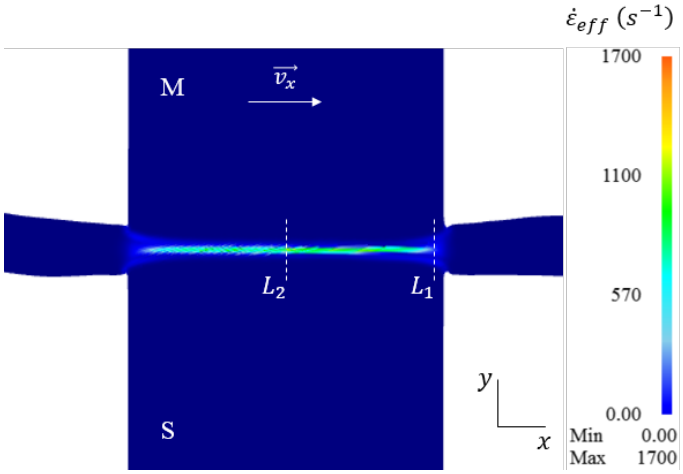

Figure 6.10: 2D effective strain rate $\dot{\varepsilon}_{eff}$ distributions at $t = 0.80s$.

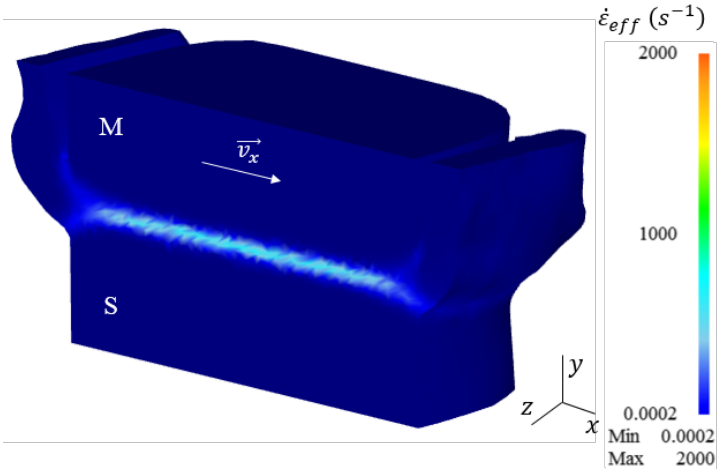

Figure 6.11: 3D effective strain rate $\dot{\varepsilon}_{eff}$ distributions at $t = 0.80s$.

According to figure 6.12(a), the x-component of velocity v_x in L_1 starts to increase at $y = -1.5\ mm$ until it reaches a maximum speed of approximately 865 mm/s, at $y = 1.5\ mm$. The velocity gradient $\frac{\partial v_x}{\partial x}$, i.e., the strain rate component, $\dot{\varepsilon}_{xx}$, is positive in the stationary side of the workpiece as the viscoplastic material is sheared and forced to accelerate[144]. This trend is visible until $y = -0.75\ mm$ where a maximum strain rate of 100 s^{-1} is reached, as depicted in figure 6.12(b). From this point onward the velocity profile starts to decay, passing through zero at the weld line, on to a negative strain rate of approximately -120 s^{-1}. The negative values of $\dot{\varepsilon}_{xx}$ are related to the flow deceleration in the x-direction of fast moving viscoplastic material probably due to viscosity effects from slower moving adjacent material. Moreover, the viscoplastic material downstream from the fast moving colder edge of the upper worpiece is under compression, also explaining the negative $\dot{\varepsilon}_{xx}$ above the weld line. A similar interpretation can be done for L_2 , although the region of interest for strain rate analysis, i.e. the WZ, is narrower.

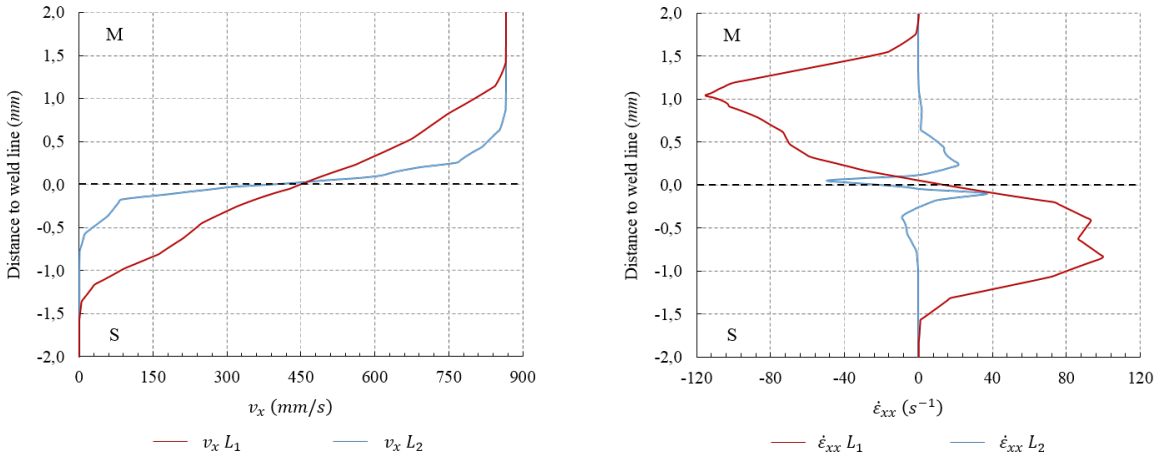

(a) (b)

Figure 6.12: Predicted values of velocity and strain rate component in the x-direction: (a)v_x and (b)$\dot{\varepsilon}_{xx}$; along two vertical lines L_1 and L_2 at $t = 0.80s$.

Theoretically, at $t = 0.80s$ where the stationary and moving part are perfectly aligned, the velocity and strain rate profiles should be symmetric around the weld line. However, this behaviour was not obtained by the models and are likely related to numerical artefacts such as, too coarse mesh size and long time steps.

Regarding the velocity in y-direction in L_1 depicted in figure 6.13(a), the movement near the edge of the upper workpiece from left to right combined with the axial pressure drags the material on its path and pushes it downwards with a velocity at the weld line of approximately 100 mm/s. As there is material being forced down the velocity gradient $\frac{\partial v_y}{\partial y}$ related to the strain rate component $\dot{\varepsilon}_{yy}$ is positive, as shown by figure 6.13(b). Naturally, this downward material flow has to be counteracted by the stationary workpiece, hence the velocity gradient decreases and $\dot{\varepsilon}_{yy}$ is negative between $y = -1.5$ mm and the weld line. In L_2 the effect of axial pressure from the stationary workpiece is predominant and forces viscoplastic material in the moving side to flow with positive velocity v_y and $\dot{\varepsilon}_{yy}$. The magnitude of v_y in L_2 is negligible compared to the flow velocities expected in the process.

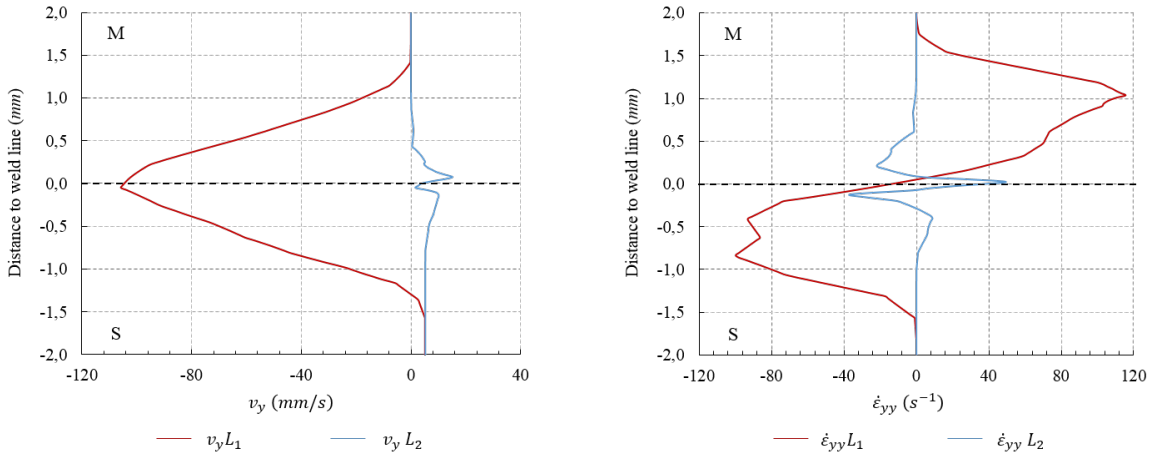

(a) (b)

Figure 6.13: Predicted values of velocity and strain rate component in the y-direction: (a) v_y and (b) $\dot{\varepsilon}_{yy}$; along two vertical lines L_1 and L_2 at $t = 0.80s$.

From the L_2 analysis the combined effect of positive v_x and negative v_y explains the downward movement of the flash during the flipping movement, which can be visually assessed from figure 6.14.

Finally, the analysis conducted in the present subsection is valid solely to $t = 0.80$ s distanced by $2\pi k$ with $k \in \mathbb{Z}$, where only the width of the WZ is expected to vary slightly with each period.

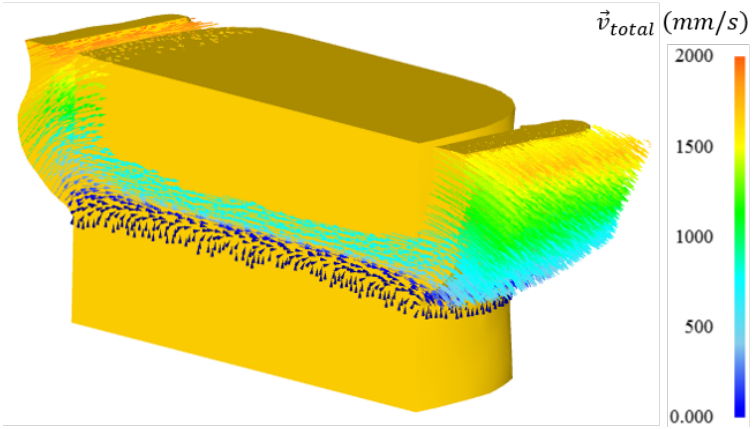

Figure 6.14: Vector plot for material flow velocity at $t = 0.80s$.

6.1.5 Thermo-metallurgical analysis

An interesting outcome of the thermo-metallurgical model is the prediction of the width of the heat affected zone (HAZ). Figure 6.15(a) illustrates the distribution of martensite after friction welding and cooling in the weld centre, HAZ and base material (BM). The width of the predicted HAZ is approximately 5 mm, taken by an average along the weld line. This is in good agreement with the measured hardness data shown in figure 6.15(b). According to Maleekian et al.[145] this agreement is expected if the model is able to predict accurately the temperature gradient (figure 6.1), thus leading to the precise prediction of the HAZ.

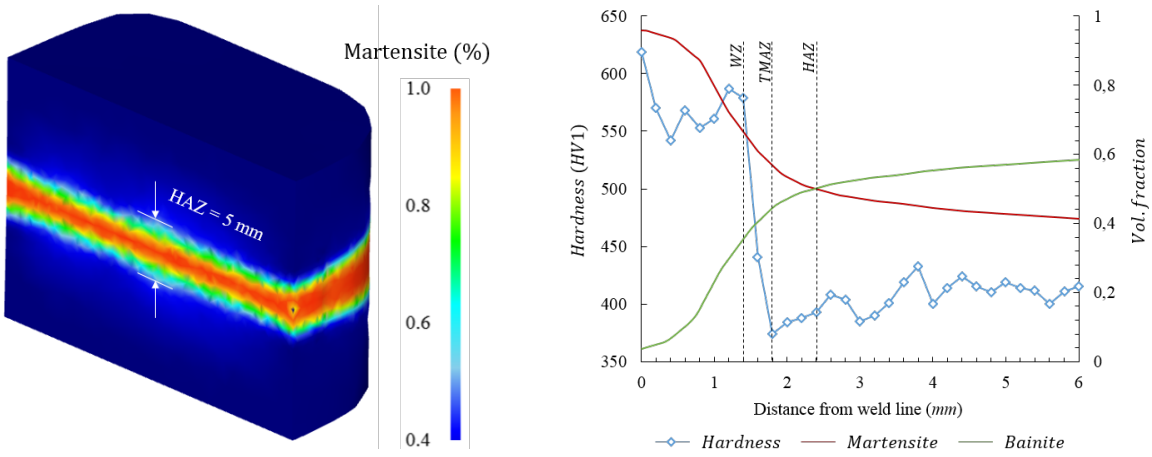

(a) (b)

Figure 6.15: (a) Predicted final volume fraction of martensite after linear friction welding and cooling; and (b) graphical representation of hardness and volume fractions as a function of the distance from the weld line.

Figure 6.15(b) also shows the predicted volume fractions of martensite and bainite as a function of longitudinal distance from the weld line. The volume fraction of martensite decreases from 96% in the centre of the WZ to 40% on the BM. The high heating rate during LFW and the consequent fast cooling rate after

welding accounts for the high amount of martensite[146]. Correspondingly, the volume of bainite increases from 3.7% on the WZ to 60% on the BM. The remainder fraction 0.3% predicted by the model at the WZ, is retained austenite.

6.1.6 Modelling applications

In previous subsections, experimental validation was carried out to a range of outputs, which resulted in very good accuracy between experimental and computational campaigns. This allowed the data predicted by the models that was non-amenable to experimental observation to be trustworthy such as, the partial unbonding phenomena or self-cleaning effect.

6.1.6.1 Partial unbonding

The partial unbonding phenomena was observed in the developed 3D model at low burn-off values, as depicted in figure 6.16. This particularity was also reported by McAndrew et al.[72] and Addison[21], and is known to compromise mechanical properties, ultimately leaving a notch that acts as a crack initiation site. Unbonding was observed solely in the corners of the cross-section with lower radii, suggesting that there might be a critical radius at which partial unbonding is prone to occur. Nonetheless, as the model progressed the heat provided to these regions by the flash and interface due to conduction, caused the corners to soften and plastically deform, thus resulting in a defect free bond.

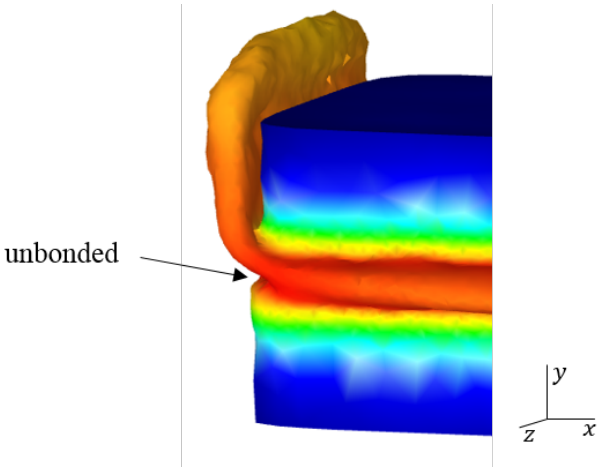

Figure 6.16: FEA appearance of partial unbonding at the interface.

6.1.6.2 Self cleaning effect

To determine whether the present combination of welding parameters provides a weld free of surface contaminants, point tracking provided by DEFORM was used along the interface. Weld line self-cleaning is an important matter since the present of surface oxides or other contaminants compromise the mechanical properties of the welded chains. Figure 6.17 (a) shows the displacement of the tracking points, each separated by 1 mm. The unwanted contaminants are expelled, providing that a sufficiently large number of oscillations

and burn-off is used. Contaminants close to the centre of the workpiece are expelled at a very slow rate since there is almost null flow in such regions, as shown in figure 6.17(c) and (d). However, according to figure 6.17(e), the minimum number of oscillation required for total expulsion of contaminant, once in the equilibrium phase, is approximately 126.

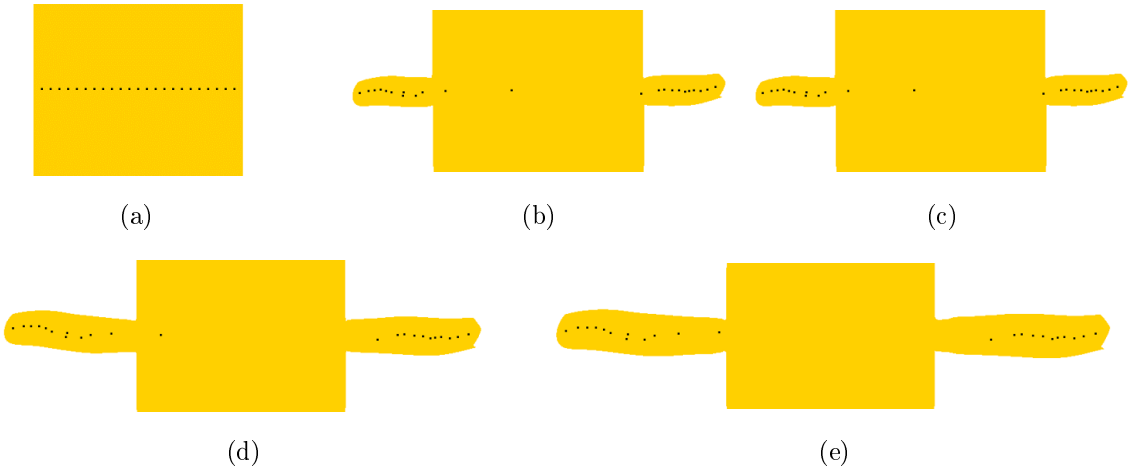

Figure 6.17: Evolution of the surface contaminants using point tracking: (a) initial positioning of the points on the weld line; points are being extruded through the flash: (b) $t = 0.25\ s$ and approximately 36 oscillations; (c) $t = 0.50\ s$ and 70 oscillations; (d) $t = 0.75\ s$ and approximately 104 oscillations; and (e) $t = 0.90\ s$ and approximately 126 oscillations.

6.1.7 Summary

This section described the combined use of 2D and 3D modelling approaches to evaluate and predict the intervening physical quantities of the LFW process when joining 30CrNiMo8 high strength steel half chain links. The key findings and advances are listed below:

- A 2D and 3D finite element modelling for the LFW of 30CrNiMo8 high strength steel chains has been formulated, using an optimized welding parameter combination, in order to predict the thermal and mechanical characteristics. This was achieved by means of a purely thermal and thermo-mechanical model. A good agreement between reality and model was achieved without application of a single fit parameter.
- The uneven interface surface of the chains is responsible for the plastic deformation present in the initial phase of the process. This phenomena is not reproducible in the purely thermal model.
- Flash showed a smooth morphology much in accordance with experimental observation apart from the slight rippling effect of this last one. This smooth pattern is related to low process parameters which yield low energy input. The local plasticisation of the material due to the uneven surface of the interface meant that the morphology of edges between experimental and predicted flash did not match. The mechanism that prevails for the set of parameters in this study, is dictated by the forging load, steadily extruding viscous material from the interface.
- The burn-off rate in the equilibrium phase yielded from the model is in good agreement with the experiment, with a burn-off rate of 3.08 mm/s and 3.13 mm/s, respectively. In the early instants of

the equilibrium phase, the predicted burn-off is underestimated, which might be explained by the fact that the temperature profile carried over from the thermal model is low. Hence, not promoting the adequate viscoplastic flow.

- The stress distribution reveals roughly a symmetrical behaviour along the weld line, although inverted according to the axial direction y. The strains and strain rates are concentrated within a narrow band with its border no more than 2 mm from the weld line for both 2D and 3D models with an effective maximum value between 170-180 and 1700-2000 s^{-1}.
- Partial unbonding was observed for low burn-off values in the cross-section corners of lower radius. The model showed that sufficient heat was provided to soften and plastically deform the regions.
- Self-cleaning study using point tracking proved to be a relevant tool to characterize the flow and expulsion of surface debris in LFW of a chain.

6.2 Numerical analysis of LFW applied to small cross-section

A parameter investigation on 30CrNiMo8 cross-section with 10 mm in diameter was conducted experimentally and numerically, using DoE, namely a factorial design. Factorial designs are an effective technique for various technologies in investigating the effect of process parameters on the weld integrity[147], and was therefore used to characterise the influence of the welding parameters by means of experimental and numerical quality outputs. Ultimately the models provided by the factorial design were validated with a random set of parameter combinations.

Figure 6.18 illustrates the welded appearance of a small cross-section specimen.

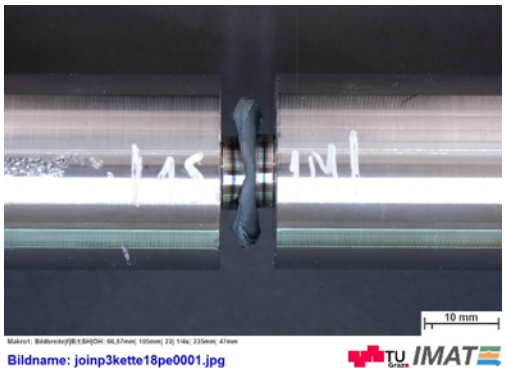

Figure 6.18: Appearance of a welded small cross-section sample.

6.2.1 Experimental design

The welding experiments were based on a 2^k full factorial design and *Minitab 16*® statistical software was used to yield the design matrix and analysis of the experimental data, where k is the number of input factors. Three welding parameters such as, amplitude (A), frequency (B) and burn-off (C) were considered as influencing factors, since they represent the main input variables of LFW[6]. Hence, $k = 3$. Other authors[148,149] considered axial load as an influencing factor. However, for the present investigation, a prescribed burn-off rate of 7 mm/s was set as a boundary condition in equilibrium phase. Therefore, the loads during the equilibrium phase are time dependent in order to keep the prescribed burn-off, regardless of the welding parameters. Each factor was evaluated at two levels. The welding parameters are kept confidential, and thus are presented by the table of signs shown in table 6.1, where $(-)$ and $(+)$ represent the low and high level configuration for each factor, respectively. Experimental (EXP) and numerical (FEA) outputs where used as quality characteristics such as, burn-off rate $\left(\dot{b_0}\right)$, extrusion zone thickness (δ), interface temperature (T_i) and interface strain rate ($\dot{\varepsilon}_{max}$). These last two were evaluated solely with FEA.

Weld	Factors		
	Amplitude (A)	Frequency (B)	Burn-off (C)
1	-	+	-
2	-	-	-
3	-	+	+
4	+	-	+
5	-	-	+
6	+	+	+
7	+	-	-
8	+	+	-

Table 6.1: 2^3experimental design matrix (table of signs) generated randomly by *Minitab 16*®.

6.2.2 Effects of the parameters

The results obtained for the EXP and FEA outputs and mean effect plots are presented in table 6.2, and figure 6.19, respectively.

Weld	Responses					
	EXP $\dot{b_0}$ [mm/s]	FEA $\dot{b_0}$ [mm/s]	EXP δ [mm]	FEA δ [mm]	FEA T_i [°C]	FEA $\dot{\varepsilon}_{max}$ [s^{-1}]
1	6.80	6.97	2.16	1.93	1020	1136
2	6.25	6.69	2.47	2.04	973	740
3	7.32	7.05	2.47	2.39	1015	1250
4	6.83	7.79	2.49	2.11	1001	1052
5	7.12	6.59	2.41	2.03	978	771
6	7.47	8.54	2.51	2.38	1038	1879
7	7.03	6.95	2.23	1.82	1001	1031
8	7.12	8.16	2.52	2.37	1039	1880

Table 6.2: Results of EXP and FEA responses.

A fairly good agreement was obtained between experimental and modelled burn off rate $\dot{b_0}$. A comparison of the mean effects of EXP and FEA $\dot{b_0}$ is shown in figure 6.19(a). Notwithstanding, welds with high heat input tend to overestimate the upset rate, which suggest that the model is comparably hotter or softer compared to the experiment. Naturally, a hotter weld coupled with the axial load will result in higher $\dot{b_0}$: Qualitatively, the trends in responses are identical, i.e. a higher $\dot{b_0}$ is expected for high levels of A, B and C, for both experiments and models. However, the welding parameters clearly have a more prominent effect on the responses of the FE models, particularly the amplitude. Both frequency and burn-off have equal effect on the upset rate of EXP which can be acknowledged by their equal slope.

Regarding δ, relatively similar results were obtained, although underestimated by the FEA. This can also be seen in figure 6.19(b), where for any given parameter at any given level the flash thickness is always lower than EXP. Once more the trend of the mean effects of EXP and FEA is comparable. Hence, a positive effect in δ is expected if amplitude, frequency and burn-off are set to higher levels. Notwithstanding, the variation of these factors affect the response more significantly the response in the FEA case due to their higher slope compared to EXP.

Finally, amplitude and frequency have a significant effect in T_i and $\dot{\varepsilon}_{max}$, whereas the influence of the burn-off is negligible, as depicted in figure 6.19(c) and (d), respectively.

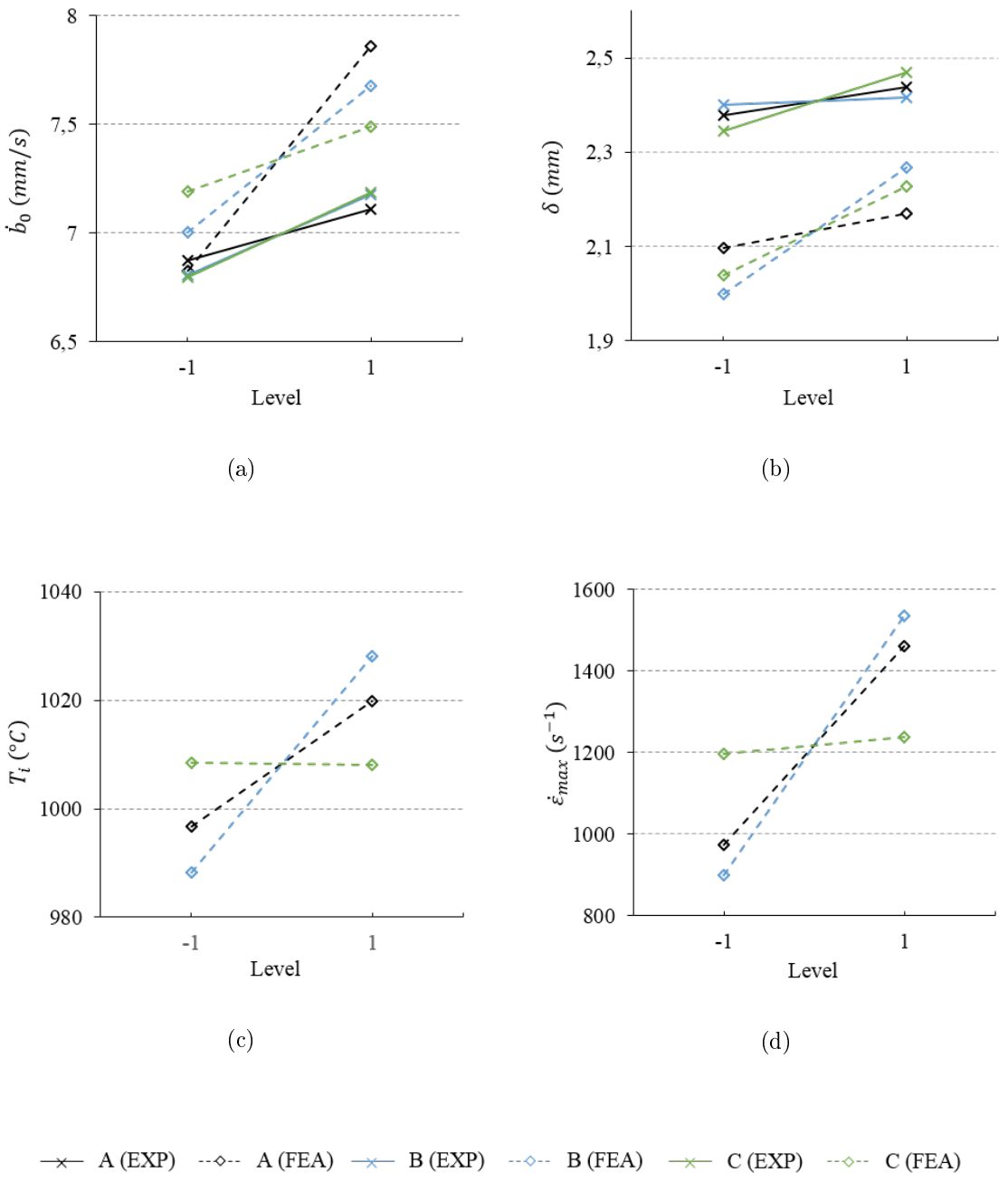

Figure 6.19: Mean effects plot: (a) $\dot{b_0}$; (b) δ; (c) T_i; and (d) $\dot{\varepsilon}_{max}$.

6.2.2.1 Correlation analysis

To evaluate the relation between comparable EXP and FEA outputs, the Pearson's product-moment correlation was used. This method measures the strength of a linear association between two variables and is denoted by r. Basically a Pearson's product-moment correlation attempts to draw a best t trough the data of the two variables, and the coefficient r indicates how far away all the data points are to this line. Coefficient r varies from -1 to 1 and the larger the absolute value of r, the stronger the relationship. If $r \geq 0.5$

or $r \leq -0.5$ the correlation between EXP and FEA outputs can be considered to be strong. The Pearson's correlation is given by:

$$r = \frac{\operatorname{cov}(X,Y)}{\sqrt{\operatorname{var}(\mathrm{X}) \cdot \operatorname{var}(\mathrm{Y})}} = \frac{\sum_{i=1}^{n}(x_i - \overline{x})(y_i - \overline{y})}{\sqrt{\sum_{i=1}^{n}(x_i - \overline{x})^2} \cdot \sqrt{\sum_{i=1}^{n}(y_i - \overline{y})^2}} \tag{6.5}$$

where x_1, x_2,..., x_n and y_1, y_2,..., y_n are the measured values of both EXP and FEA variables, respectively, within the output being evaluated $\dot{b_0}$ or δ; and $\overline{x}$ and $\overline{y}$ are the mean values. Furthermore, n is the number of measured values, which in this case is 8.

The correlation for experimental and numerical burn-off rate is $r_{\dot{b_0}} = 0.5$. Furthermore, in terms of flash thickness $r_\delta = 0.8$ was obtained. The positive value in correlation suggests that as one value of one variable increases, so does the value of the other variable. This can easily be seen from the mean plots in figure 6.19. In both cases a strong association can be established between EXP and FEA for both outputs, although $\dot{b_0}$ show higher scattering. This is also relatable to figure 6.19 since a positive variation in EXP $\dot{b_0}$ traduces in larger variation in FEA $\dot{b_0}$. On the other hand, and despite δ EXP and FEA having slightly different values, the increase in one value will affect the other in almost the same manner, thus the higher correlation factor.

6.2.3 ANOVA and regression analysis

The statistical technique analysis of variance (ANOVA) has been applied to identify the significant input parameters which are expected to influence the output responses. Thus, the ANOVA tables 6.3-6.8 summarize the results in terms of sum of squares (SS), mean squares (MS), F-value and P-value. According to literature[150,151], if the P-value is lower than $\alpha = 0.05$ one can assume that a particular factor has statistical significance. Additional statistical indicators are presented, such as R^2, *Adjusted* R^2 and *Predicted* R^2 to assess the fit of the obtained regression models. A significance test was carried out to eliminate the insignificant contrasts, although the appropriate ones were kept to achieve better regression characteristics.

6.2.3.1 Burn-off rate $\left(\dot{b_0}\right)$

All welding parameters have a significant and synergistic effect in EXP $\dot{b_0}$, presenting very similar P-values. Furthermore, the interactions, apart from B·C, also proved to be significant towards EXP $\dot{b_0}$, according to table 6.3. This might be explained by the fact that all parameters try to balance each other in order to maintain the specified burn-off rate. On the other hand, statistical results of FEA suggest that only amplitude and frequency are the prominent factors influencing FEA $\dot{b_0}$, highlighted in table 6.4. This has to do with the fact that, when the amplitude reaches maximum displacement, a pressure increase occurs due to the decrease in contact area at the interface. As a result, cooler material ploughs into the highly viscous material. With the retracting movement of the workpieces to the aligned position, the viscous material shears past the cooler edge of the workpiece. Hence, for high levels of A and B the shearing process is faster and consequently $\dot{b_0}$ increases. This remark is also valid for EXP.

Despite the statistical significance of C, in reality it is believed that once in steady state conditions, the influence in plastic deformation and thermal profile is independent of this latter factor[30,95]. Thus, serves the purpose of enhancing model fitting characteristics.

The estimated coefficients by *Minitab 16*® for the EXP and FEA $\dot{b_0}$ using data in coded units were drawn out to yield the mathematical models given by equations 6.6 and 6.7.

Source	Sum of squares	d	Mean square	F-value	P-value
Main effects	0.6855	3	0.2285	4570	0.011
A	0.1152	1	0.1152	2304	0.013
B	0.2738	1	0.2738	5476	0.009
C	0.2965	1	0.2965	5929	0.008
A·C	0.1922	1	0.1922	3844	0.010
B·C	0.0050	1	0.0050	100	0.063
A·B·C	0.1013	1	0.1013	2025	0.014
Residual	5e-5	1	5e-5		
Total	0.9840	7			
R^2=99.99%	Adj. R^2=99.96%		Pred.R^2=99.67%		

Table 6.3: ANOVA table for EXP $\dot{b_0}$.

Source	Sum of squares	d	Mean square	F-value	P-value
Main effects	3.2337	3	1.0779	35.34	0.028
A	2.1425	1	2.1425	70.24	0.014
B	0.9113	1	0.9113	29.88	0.032
C	0.1800	1	0.1800	5.90	0.136
A·B	0.1861	1	0.1861	6.10	0.132
A·C	0.1922	1	0.1922	6.30	0.129
Residual	0.0610	2	0.0305		
Total	3.6729	7			
R^2=98.34%	Adj. R^2=94.19%		Pred.R^2=73.43%		

Table 6.4: ANOVA table for FEA $\dot{b_0}$.

$$\dot{b_0}(EXP) = 6.9925 + 0.120 \cdot A + 0.1850 \cdot B + 0.1925 \cdot C - 0.1550 \cdot A \cdot C + 0.0250 \cdot B \cdot C + 0.1125 \cdot A \cdot B \cdot C \quad (6.6)$$

$$\dot{b_0}(FEA) = 7.3425 + 0.5175 \cdot A + 0.3375 \cdot B + 0.150 \cdot C - 0.0153 \cdot A \cdot B + 0.1550 \cdot A \cdot C \quad (6.7)$$

In order to study the progress of material flow and consequently axial shortening, the relative burn-off history (b_0^*) of the welds considered in the DoE were analysed in intervals of $0.05s$. b_0^* is obtained by the relation between the burn-off at a particular time step t and the specified burn-off according to the design matrix at t_{final}, given in equation 6.8.

$$b_0^* = \frac{b_0(t)}{b_0(t_{final})} \quad (6.8)$$

The results are depicted in figure 6.20 and relate solely to the equilibrium phase of the process. In general, very good agreement can be observed between EXP and FEA burn-off histories, despite some discrepancies which are more prominent for high heat input welds, such as 6 and 8 depicted by figure 6.20(f) and (h) respectively. For welds 2 and 3, illustrated in figure 6.20(b) and (c) respectively, the burn-off was clearly overestimated in the initial 0.1 s of the equilibrium phase. This suggests that the heat provided by the

thermal model is excessive. Nonetheless, the time dependent axial load ended up compensating this effect for the remainder of the equilibrium phase.

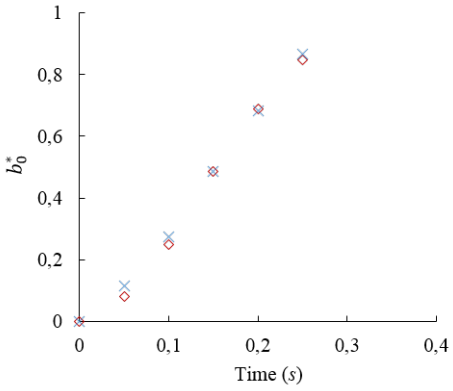

(a) weld 1: A = -1, B = +1, C = -1

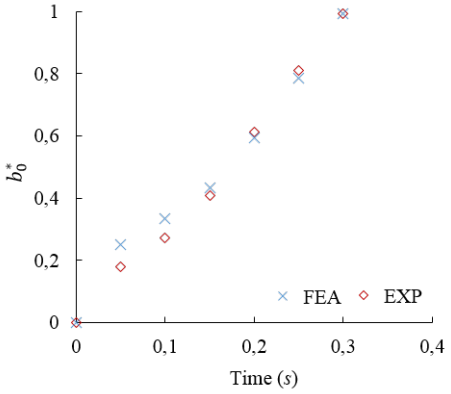

(b) weld 2: A = -1, B = -1, C = -1

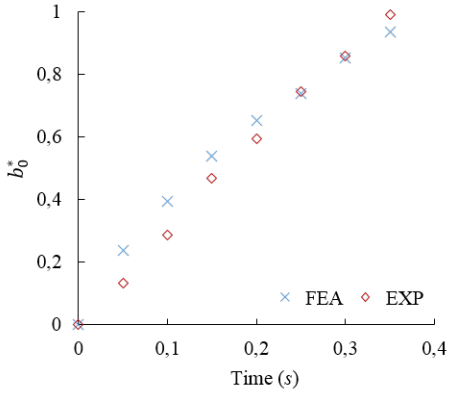

(c) weld 3: A = -1, B = +1, C = +1

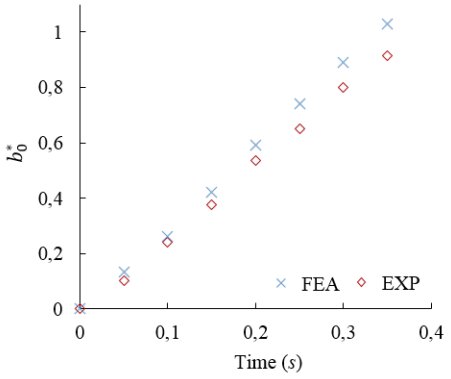

(d) weld 4: A = +1, B = -1, C = +1

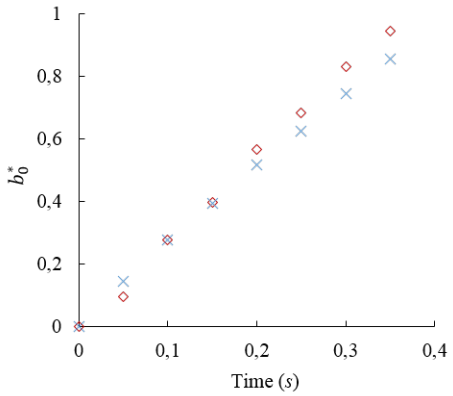

(e) weld 5: A = -1, B = -1, C = +1

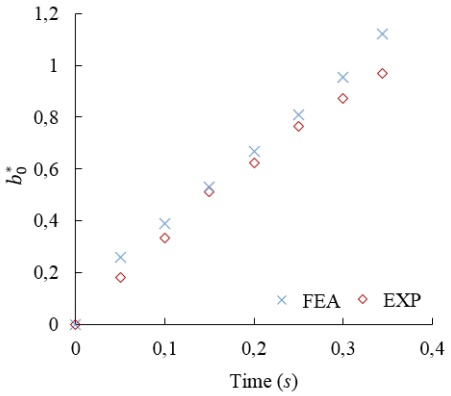

(f) weld 6: A = +1, B = +1, C = +1

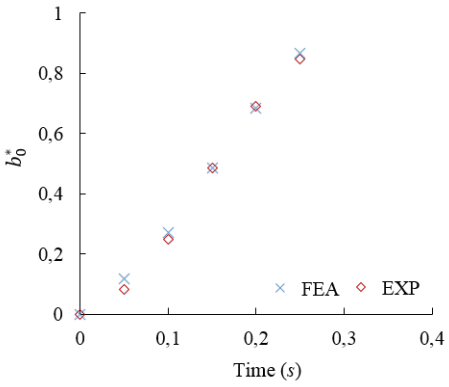

(g) weld 7: A = +1, B = -1, C = -1

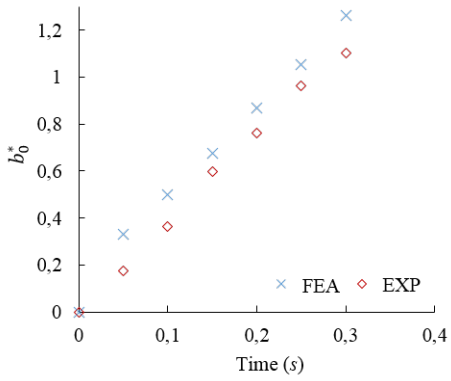

(h) weld 8: A = +1, B = +1, C = -1

Figure 6.20: Comparison of the burn-off histories between EXP and FEA: a) weld 1; b) weld 2; c) weld 3; d) weld 4; e) weld 5; f) weld 6; g) weld 7; and h) weld 8.

6.2.3.2 Extrusion zone thickness (δ)

The experimental flash thickness is strongly influenced by C and interactions A·B and A·B·C, according to table 6.5. The strong influence with C might be due to the additional welding time in order to achieve the designated burn-off, once $\dot{b_0}$ is to be kept at constant rate throughout the equilibrium phase. As consequence, conduction heat transfer will extend further from the interface, meaning that wider regions reach viscoplastic condition. Unlike in EXP, B is also significant in FEA flash thickness. This discrepancy might be due to model related hypothesis, such as plain strain assumption, friction conditions which are modelled using a power law, and material model, as flow stresses and thermal properties. Thus, further research has to be conducted to assess the influence of such assumptions on the comparative analysis of EXP and FEA.

Source	Sum of squares	d	Mean square	F-value	P-value
Main effects	0.0389	3	0.0130	20.75	0.046
A	0.0072	1	0.0072	11.52	0.077
B	0.0005	1	0.005	0.72	0.486
C	0.0313	1	0.0313	50.00	0.019
A·B	0.0392	1	0.0392	62.72	0.016
A·B·C	0.0512	1	0.0512	81.82	0.012
Residual	0.0013	2	6.25e-4		
Total	0.1305	7			
R^2=99.04%	Adj. R^2=99.65%		Pred.R^2=84.68%		

Table 6.5: ANOVA table for EXP δ.

Source	Sum of squares	d	Mean square	F-value	P-value
Main effects	0.2239	3	0.0746	20.38	0.047
A	0.0105	1	0.0105	2.87	0.232
B	0.1431	1	0.1431	39.08	0.025
C	0.0703	1	0.0703	19.20	0.048
A·B	0.0406	1	0.0406	11.09	0.080
A·B·C	0.0703	1	0.0703	19.20	0.048
Residual	0.0073	2	0.0037		
Total	0.3422	7			
R^2=97.86%	Adj. R^2=92.51%		Pred.R^2=65.75%		

Table 6.6: ANOVA table for FEA δ.

$$\delta(EXP) = 2.4075 + 0.030 \cdot A + 0.0075 \cdot B + 0.0625 \cdot C - 0.070 \cdot A \cdot B - 0.160 \cdot A \cdot B \cdot C \tag{6.9}$$

$$\delta(FEA) = 2.1338 + 0.0363 \cdot A + 0.1338 \cdot B + 0.0938 \cdot C - 0.0713 \cdot A \cdot B - 0.1875 \cdot A \cdot B \cdot C \tag{6.10}$$

Figure 6.21 depicts a comparison between EXP and FEA flash of three welds with different heat inputs (low, medium and high given by welds 2, 3 and 6, respectively). Morphologically, the FEA flash is highly deformed in comparison to EXP. This can be explained by the fact that no material flow occurs perpendicular to the oscillatory direction in FEA. Hence, a higher amount of material is expelled in the oscillatory direction, which eventually contact the surface of the outer rod due to the flipping movement of the flash. Notwithstanding, the predicted flash was able to capture the rippling features present in EXP for the medium and high heat inputs shown in figure 6.21(b) and (c), respectively. Whereas for the low heat input, despite there being ripples in the EXP, the FEA was not able to captures them as illustrated in figure 6.21(a). The reason behind this result is likely due to the element size selected for the models, which prove to be suitable for medium and high heat input welds. Moreover, the amplitude also plays an important role since high level amplitudes are related to a more distinct ripple formation[80,86] (see table 6.1).

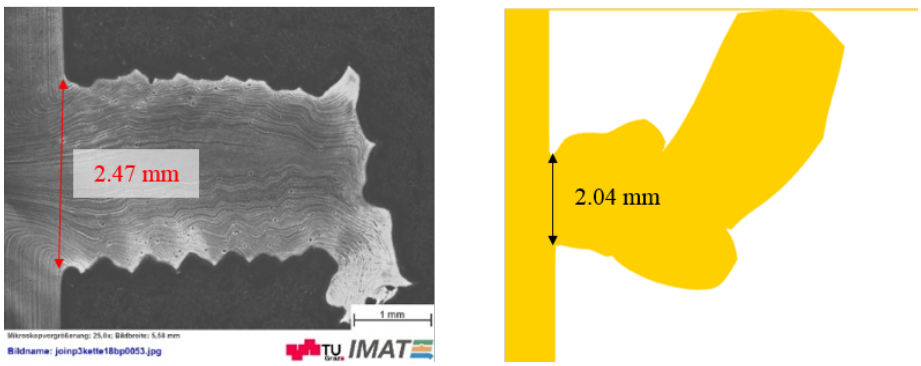

(a)

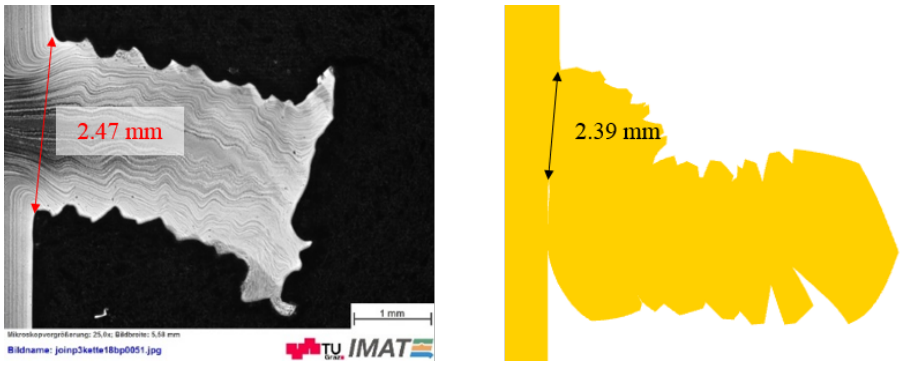

(b)

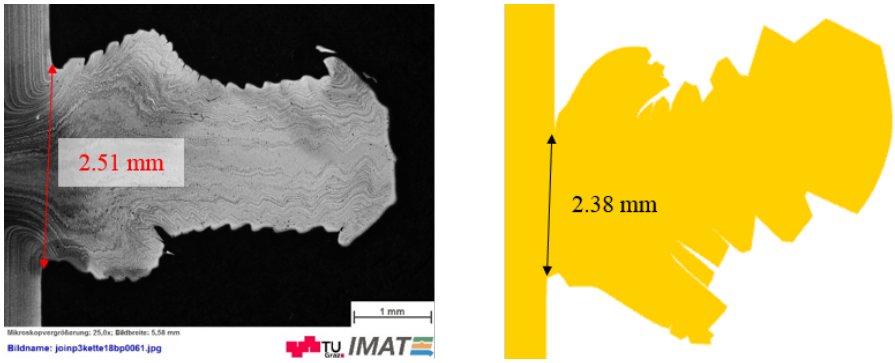

(c)

Figure 6.21: Comparison between experimental and modelled flash: (a) low heat input - weld 2, (b) medium heat input - weld 3; and (c) high heat input - weld 6.

6.2.3.3 Interface temperature (T_i)

Regarding T_i, frequency is the most significant main effect followed by the amplitude, resulting in a hotter weld line[80]. On the other hand, the burn-off has no significance towards the temperature at the interface. Besides the fact that low levels of A and B yield low heat inputs, the axial load during equilibrium phase required to ensure 7 mm/s burn-off rate has to be higher, for comparable C. According to[36], this can be explained by the relationship between the power input and $\dot{b}_0$. Since the upset rate is virtually the same for all welds, a reduction in the force results in a larger amount of heat conducts back from the interface, for high heat input compared to low heat input welds. The outcome is the broadening of the region of heated material. This effect combined with the heat generated by plastic deformation at the interface results in a higher T_i[33].

Source	Sum of squares	d	Mean square	F-value	P-value
Main effects	4243.68	3	1414.56	2102.50	0.016
A	1064.91	1	1064.91	1582.81	0.016
B	3178.44	1	3178.44	4724.19	0.009
C	10.67	1	10.67	0.50	0.608
A·B	7.57	1	7.57	11.25	0.184
B·C	13.73	1	13.73	20.41	0.139
A·B·C	10.67	1	10.67	15.86	0.157
Residual	0.67	1	0.67		
Total	4276.32	7			
R^2=99.98%	Adj. R^2=99.89%		Pred.R^2=98.99%		

Table 6.7: ANOVA table for FEA T_i.

$$T_i(FEA) = 1008.22 + 11.54 \cdot A + 19.93 \cdot B - 0.20 \cdot C - 0.97 \cdot A \cdot B - 1.31 \cdot B \cdot C + 1.16 \cdot A \cdot B \cdot C \quad (6.11)$$

6.2.3.4 Interface strain rate ($\dot{\varepsilon}_{max}$)

The main and interaction effects between amplitude and frequency are significant to $\dot{\varepsilon}_{max}$, increasing the required flow stress. Nonetheless, for higher A and B the heat input at the interface will also be higher, resulting in an increase of T_i, and consequently lower flow stress[152]. Notice through table 6.2 that high $\dot{\varepsilon}_{max}$ is associated to high T_i, suggesting that both previously mentioned consequences cancel out. Such result was also reported in[33].

Source	Sum of squares	d	Mean square	F-value	P-value
Main effects	1.29e6	3	4.30e6	898.16	0.025
A	4.73e5	1	4.73e5	988.37	0.020
B	8,12e5	1	8.12e5	1698.91	0.015
C	3400	1	3400	7.19	0.227
A·B	80254	1	80254	167.72	0.049
B·C	1992	1	1992	4.16	0.290
A·B·C	1339	1	1339	2.80	0.343
Residual	478	1	478		
Total	1.37e6	7			
R^2=99.97%	Adj. R^2=97.77%		Pred.R^2=96.76%		

Table 6.8: ANOVA table for FEA $\dot{\varepsilon}_{max}$.

$$\dot{\varepsilon}_{max} = 1217.31 + 243.14 \cdot A + 318.77 \cdot B + 20.74 \cdot C + 100.16 \cdot A \cdot B - 15.78 \cdot A \cdot C - 12.94 \cdot A \cdot B \cdot C \quad (6.12)$$

6.2.4 Validation of the developed models

The obtained mathematical models (equations 6.6-6.12) indicated fairly good regression characteristics (see tables 6.3-6.8), apart from the model concerning FEA δ, with a *Predicted* R^2 of 65.75%.

Confirmation tests were carried out to test the adequacy of the developed models when subjected to combinations within the evaluated parameter range, other than the eight combinations given by the design. To that end, two tests were considered, using random parameter combination. Table 6.9 summarizes the obtained results for the considered confirmation experiments. Once more, each parameter value is given in coded units. The mathematical models obtained in the previous section seem to predict appropriately the outputs with a maximum error of 12.2% for FEA $\dot{\varepsilon}_{max}$. Although the *Predicted* R^2 of FEA δ was low according to ANOVA, the model was able to adequately forecast the response for both confirmation experiments.

Experiment	Parameters			Responses						
	A	B	C		EXP $\dot{b}_0$	FEA $\dot{b}_0$	EXP δ	FEA δ	FEA T_i	FEA $\dot{\varepsilon}_{max}$
Expt. I	0	0	+1	Result	7.53	7.91	2.45	2.05	1011	1087
				Predicted*	7.19	7.49	2.47	2.23	1008	1238
				Error (%)	4.7	5.6	0.8	8.1	0.26	12.2
Expt. II	+1	-1	0	Result	7.62	7.59	2.39	2.00	1001	1052
				Predicted*	6.93	7.51	2.36	1.96	1001	1042
				Error (%)	10	1.1	1.3	2.0	0	1.0

*based on equations derived from statistical evaluation

Table 6.9: Confirmation experiments.

6.3 Summary

The process parameters of linear friction welded small cross-sections was studied, from which the following conclusions can be drawn:

- A 2D finite element model for the LFW of 30CrNiMo8 high strength steel 10 mm cross-section pins has been formulated and compared to experiments to evaluate the influence of different welding parameters on the final joint. A systematic experimental approach using full factorial design was used and outputs evaluated experimentally and numerically.
- Relatively good agreement was obtained between experiments and modelling. However, some differences in the statistical effect of the parameters was observed from one to the other, particularly regarding burn-off rate, where main and interaction effects exhibited a similar contribution to EXP, in contrast with FEA where solely amplitude and frequency have a significant effect.
- Burn-off is the contrast affecting prominently δ due to the additional welding time, and consequently heat conducted back from the interface, in order to achieve the designated upset.
- Statistical discrepancies between EXP and FEA might be attributed to model related assumptions, such as plain strain which excludes the possibility of material flow in the perpendicular direction; heat input (friction) model and material model are further sources of uncertainty.
- Amplitude and frequency are the most significant factors on either T_i and $\dot{\varepsilon}_{max}$. A balancing effect between required flow stress and interface temperature related to high amplitude and frequency was observed when analysing $\dot{\varepsilon}_{max}$.
- The mathematical models proved to be reliable for the investigated parameter window, with the actual values of the confirmation experiments matching fairly well the predicted ones. A mismatch regarding the morphological characteristics of the flash was observed. FEA shows high deformation compared to EXP due to the modelling assumptions made.

Chapter 7

Concluding remarks and outlook

The main findings and advances in LFW of chains, followed by an outlook for further research within this subject, is presented in this section. This should allow the reader to appreciate the benefits of numerical modelling in LFW process for joining 30CrNiMo8 high strength steel chains, envisioning further process development and exploitation.

Numerical modelling, particularly the finite element method was used by means of the commercial software DEFORM® 11.1 SP1. At the centre of this study were two distinct case studies: one focusing on the well established pewag *Hero* chain using a single optimized parameter combination; and the other on the applicability and the gathering of knowledge of the LFW process to join chains with smaller cross-section, using Design of Experiments.

Naturally, the numerical effort presented carries a number of limitations, resulting from the different modelling assumptions discussed throughout. The most prominent assumption was neglecting the plastic deformation in the initial phase of the pewag *Hero* case study, as a result of the modelling approach used, i.e. purely thermal for the initial phase and thermo-mechanical for the equilibrium phase. Consequently, this hindered the understanding of viscoplastic phenomena happening in the initial phase.

Experimental validation was carried out to a range of outputs, which resulted in very good accuracy between experimental and computational campaigns. This allowed the data predicted by the models that was non-amenable to experimental measurement to be trustworthy, such as stress, strain, and strain rate analysis.

This study concludes that modelling can indeed support continuous knowledge build-up towards LFW of chains, without the need of exaggerated experimental campaigns. For this reason, the successful numerical investigation comprised in this research has resulted in the direct implementation of FEM in the pewag *Hero* chains production line.

Despite the advances in modelling reported in the present dissertation, as a tool to analyse comprehensively the linear friction welding process applied to chains, there are still several knowledge gaps that need to be tackled. Some of which are:

1. ***Influence of interface geometry***: most of the modelling effort has been put into planar interface geometries. However, the influence of the interface geometry (e.g. bevels angles) on LFW chains should be assessed and optimized to reduce flash formation and ultimately curtail the amount of scrap generated during production.

2. ***Microstructure modelling***: models could be used to investigate the impact of the processing conditions on the microstructure evolution. This would allow for the effects of the processing conditions on different phases, average grain size and their spatial distribution.

3. ***Flash formation***: the models can be enhanced to provide an even more accurate flash formation and final shape. The use of smaller elements in the interface coupled with higher computational power and efficient solvers is key to capture even more detail and important features related to the flash formation.

4. ***Residual stress analysis***: modelling can be used to predict the impact of the processing conditions, such as the workpiece geometry, amplitude, frequency, axial load, on the formation and magnitude of residual stresses in linear friction welds. Figure 7.1 shows some preliminary results on residual stresses after cooling and before PWHT. The predicted results were compared with the hole-drilling method. However, this method only accounts for the stress state near the surface. Hence, a further step is to compare the predicted results using other residual stress measurement techniques, such as neutron diffraction or contour method.

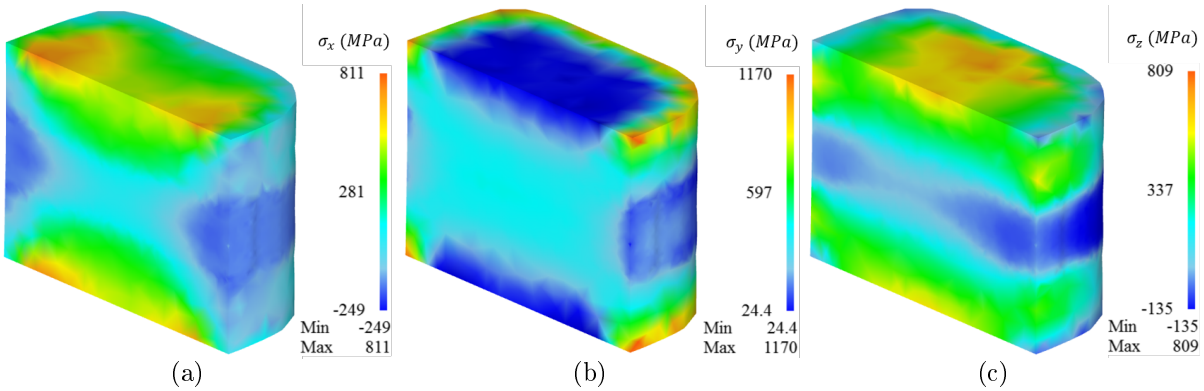

Figure 7.1: Residual stresses in: (a) σ_x; (b) σ_y; and (c) σ_z.

5. ***Extension to other materials***: Although the focus of this article is on 30CrNiMo8, there is still a need to understand the effects of the LFW process on the joining of other high-value materials, such as aluminium alloys, aluminium-lithium alloys and nickel-based superalloys, even if not within the scope of chain welding.

6. ***Tool wear***: the clamping system of a LFW machine is subjected to high cycle fatigue (HCF) due to the reciprocating motion and loads involved during the process (axial and in-plane). As a result the clamping systems geometric features can surpass the acceptable clearances. FEA is therefore a powerful tool to conduct a predictive analysis of tool wear and assist in a "real life" maintenance plan.

7. ***3D modelling of small cross-sections***: in the present study a 2D analysis was deliberated for the sake of calculation time. However, it is technically unsound to reduce a circular cross-section to a plain strain problem. Despite the adequate results obtained, for the best parameters yielding from the DoE analysis, a 3D analysis should be considered as a future step to understand how much a difference exists.

Bibliography

[1] D Radaj. *Heat effects of welding: temperature field, residual stress, distortion*. Springer, 1992.

[2] Tsubakimoto Chain Co. A Brief History of Chain, 1995.

[3] Makoto. Kanehira and Kyosuke. Otoshi. *The complete guide to chain*. Tsubaki, 1997.

[4] Pewag. History of the pewag Group.

[5] Gianluca Buffa, Marco Cammalleri, Davide Campanella, and Livan Fratini. Shear coefficient determination in linear friction welding of aluminum alloys. *Materials & Design*, 82:238–246, 2015.

[6] I. Bhamji, M. Preuss, P.L. L Threadgill, and A.C. C Addison. Solid state joining of metals by linear friction welding: a literature review. *Materials Science and Technology*, 27(1):2–12, 2011.

[7] A. Vairis and M. Frost. High frequency linear friction welding of a titanium alloy. *Wear*, 217(1):117–131, 1998.

[8] E.D. Nicholas. Friction Processing Technologies. *Welding in the World*, 47(11):2–9, 2003.

[9] M. Maalekian. Friction welding - critical assessment of literature. *Science and Technology of Welding and Joining*, 12(8):738–759, 2007.

[10] W A Baeslack, T F Broderick, M Juhas, and H L Fraser. Characterization of solid-phase welds between Ti-6A1-2Sn-4Zr-2Mo-0.1Si and Ti-13.5A1-21.5Nb titanium aluminide. *Materials Characterization*, 33(4):357–367, 1994.

[11] A. Chamanfar, M. Jahazi, J. Gholipour, P. Wanjara, and S. Yue. Maximizing the integrity of linear friction welded Waspaloy. *Materials Science and Engineering A*, 555:117–130, 2012.

[12] Priti Wanjara and M. Jahazi. Linear friction welding of Ti-6Al-4V: Processing, microstructure, and mechanical-property inter-relationships. *Metallurgical and Materials Transactions A: Physical Metallurgy and Materials Science*, 36(8):2149–2164, 2005.

[13] A. C. Addison. Linear Friction Welding of Engineering Metals. *TWI Ltd Core research program report*, 2008.

[14] Kemal Mucic, Franz Fuchs, and Norbert Enzinger. Process optimization for linear friction welding of high strength chain. In *EUROJOIN Conference*, pages 157–166, Pula, Croatia, 2012.

[15] Kemal Mucic, Norbert Enzinger, and Franz Fuchs. Linear Friction Welding of High Strength Chains. *Trends in Welding Research: Proceedings of the 9th international conference*, pages 752–756, 2013.

[16] Anthony R. McAndrew, Paul A. Colegrove, Clement Bühr, Bertrand C.D. Flipo, and Achilleas Vairis. A literature review of Ti-6Al-4V linear friction welding. *Progress in Materials Science*, 92(October):225–257, 2018.

[17] W Richter. Herbeifuhrung einer Haftverbindung zwischen Plattchen aus Werkzeugstahl und deren Tragern nach Art einer SchweiBung oder Lotung, 1929.

[18] M. E. Nunn. Aero engine improvements through linear friction welding. In *1st International Conference on Innovation in Aerospaceb Sciences*, Queen's University Belfast, Northern Ireland, UK, 2005.

[19] Wenya Li, Achilles Vairis, Michael Preuss, and Tiejun Ma. Linear and rotary friction welding review. *International Materials Reviews*, 61(2):71–100, 2016.

[20] R. Mayura and J. Kauzlarich. Reciprocating Friction Bonding Apparatus, 1969.

[21] A. C. Addison. Linear friction welding information for production engineering. *TWI Industrial Member Report Summary*, 961, 2010.

[22] P. Frankel, M. Preuss, A. Steuwer, P. J. Withers, and S. Bray. Comparison of residual stresses in Ti-6Al-4V and Ti-6Al-2Sn-4Zr-2Mo linear friction welds. *Materials Science and Technology*, 25(5):640–650, 2009.

[23] K. T. Slattery. Structure assemblies and preforms therefor formed by linear friction welding, 2007.

[24] I Bhamji, a C Addison, P L Threadgill, and M Preuss. *Linear friction welding in aerospace engineering*. Woodhead Publishing Limited, 2012.

[25] A. Vairis and M Frost. On the extrusion stage of linear friction welding of Ti 6Al 4V. *Materials Science and Engineering: A*, 271(1-2):477–484, 1999.

[26] U. U. Ofem, P. A. Colegrove, A. Addison, and M. J. Russell. Energy and force analysis of linear friction welds in medium carbon steel. *Science and Technology of Welding and Joining*, 15(6):479–485, 2010.

[27] A. Vairis and M. Frost. Modelling the linear friction welding of titanium blocks. *Materials Science and Engineering A*, 292(1):8–17, 2000.

[28] F Schroeder, R M Ward, R P Turner, M M Attallah, J Gebelin, and R C Reed. Linear friction welding of titanium alloys for aeroengine applications: modelling and validation. *9th International Conference on Trends in Welding Research*, (January):886 – 892, 2012.

[29] R. Turner, R. M. Ward, R. March, and R. C. Reed. The magnitude and origin of residual stress in Ti-6Al-4V linear friction welds: An investigation by validated numerical modeling. *Metallurgical and Materials Transactions B: Process Metallurgy and Materials Processing Science*, 43(1):186–197, 2012.

[30] Wen-Ya Li, Tiejun Ma, and Jinglong Li. Numerical simulation of linear friction welding of titanium alloy: Effects of processing parameters. *Materials & Design*, 31(3):1497–1507, 2010.

[31] Patrick Romilly. Linear Friction Welding for Near Net Shape Manufacturing of Titanium Parts. *Proceedings of the 13th World Conference on Titanium*, pages 1423–1427, 2016.

[32] Anthony R. McAndrew, Paul A. Colegrove, Adrian C. Addison, Bertrand C D Flipo, and Michael J. Russell. Energy and Force Analysis of Ti-6Al-4V Linear Friction Welds for Computational Modeling Input and Validation Data. *Metallurgical and Materials Transactions A: Physical Metallurgy and Materials Science*, 45(13):6118–6128, 2014.

[33] Anthony R. McAndrew, Paul A. Colegrove, Adrian C. Addison, Bertrand C D Flipo, and Michael J. Russell. Modelling the influence of the process inputs on the removal of surface contaminants from Ti-6Al-4V linear friction welds. *Materials and Design*, 66(PA):183–195, 2015.

[34] W. Y. Li, T. J. Ma, S. Q. Yang, Q. Z. Xu, Y. Zhang, J. L. Li, and H. L. Liao. Effect of friction time on flash shape and axial shortening of linear friction welded 45 steel. *Materials Letters*, 62(2):293–296, 2008.

[35] Imran Bhamji, Michael Preuss, Philip L. Threadgill, Richard J. Moat, Adrian C. Addison, and Matthew J. Peel. Linear friction welding of AISI 316L stainless steel. *Materials Science and Engineering A*, 528(2):680–690, 2010.

[36] J. Romero, M. M. Attallah, M. Preuss, M. Karadge, and S. E. Bray. Effect of the forging pressure on the microstructure and residual stress development in Ti-6Al-4V linear friction welds. *Acta Materialia*, 57(18):5582–5592, 2009.

[37] Caroline Mary and Mohammad Jahazi. Linear Friction Welding of IN-718 Process Optimization and Microstructure Evolution. *Advanced Materials Research*, 15-17:357–362, 2007.

[38] P. L. Threadgill. Terminology in friction stir welding. *Science and Technology of Welding and Joining*, 12(4):357–360, 2007.

[39] P.S. Effertz, V. Infante, L. Quintino, U. Suhuddin, S. Hanke, and J.F. dos Santos. Fatigue life assessment of friction spot welded 7050-T76 aluminium alloy using Weibull distribution. *International Journal of Fatigue*, 87:381–390, 2016.

[40] O M Ivasishin, S V Shevchenko, and S L Semiatin. Effect of crystallographic texture on the isothermal beta grain-growth kinetics of Ti-6Al-4V. *Materials Science & Engineering A*, 332(1-2):343–350, 2002.

[41] W.-Y. Li, T. Ma, Y. Zhang, Q. Xu, J. Li, S. Yang, and H. Liao. Microstructure Characterization and Mechanical Properties of Linear Friction Welded Ti-6Al-4V Alloy. *Advanced Engineering Materials*, 10(1-2):89–92, 2008.

[42] M Karadge, M Preuss, C Lovell, P J Withers, and S Bray. Texture development in Ti-6Al-4V linear friction welds. *Materials Science and Engineering A, Structural Materials: Properties, Microstructure and Processing*, 459(1-2):182–191.

[43] R Ding, Z X Guo, Wei Sha, and A Wilson. Microstructural evolution of a Ti-6Al-4V alloy during thermomechanical processing. page 104, apr 2000.

[44] Tiejun Ma, Tao Chen, Wen Ya Li, Shiwei Wang, and Siqian Yang. Formation mechanism of linear friction welded Ti-6Al-4V alloy joint based on microstructure observation. *Materials Characterization*, 62(1):130–135, 2011.

[45] T. Seshacharyulu, S. C. Medeiros, W. G. Frazier, and Y. V.R.K. Prasad. Microstructural mechanisms during hot working of commercial grade Ti-6Al-4V with lamellar starting structure. *Materials Science and Engineering A*, 325(1-2):112–125, 2002.

[46] V Corzo, O Casals, J Alcalá, A Mateo, and M Anglada. Mechanical evaluation of linear friction welds in titanium alloys through indentation experiments. *Welding International*, 21(2):125–129, jan 2007.

[47] Gianluca Buffa, Davide Campanella, Marco Cammalleri, Antonino Ducato, Antonello Astarita, Antonino Squillace, Sergio Esposito, and Livan Fratini. Experimental and Numerical Analysis of Microstructure Evolution during Linear Friction Welding of Ti6Al4V. *Procedia Manufacturing*, 1:429–441, 2015.

[48] T. Ahmed and H.J. Rack. Phase transformations during cooling in α+β titanium alloys. *Materials Science and Engineering: A*, 243(1-2):206–211, 1998.

[49] T. J. Ma, W. Y. Li, and S. Y. Yang. Impact toughness and fracture analysis of linear friction welded Ti-6Al-4V alloy joints. *Materials and Design*, 30(6):2128–2132, 2009.

[50] J. C. Stinville, F. Bridier, D. Ponsen, P. Wanjara, and P. Bocher. High and low cycle fatigue behavior of linear friction welded Ti-6Al-4V. *International Journal of Fatigue*, 70:278–288, 2015.

[51] P. L. Threadgill. The prospects for joining titanium aluminides. *Materials Science and Engineering A*, 192-193(PART 2):640–646, 1995.

[52] Tiejun Ma, Wen Ya Li, Quanzhou Xu, Yong Zhang, Jinglong Li, Siqian Yang, and Hanlin Liao. Microstructure evolution and mechanical properties of linear friction welded 45 steel joint. *Advanced Engineering Materials*, 9(8):703–707, 2007.

[53] Y Fu, W.Y. Li, and X.W. Yang. Microstructure analysis of linear friction welded AISI 321 stainless steel joint. *Journal of Engineering Science and Technology Review*, 8(Specialiss):37–39, 2015.

[54] M. Karadge, M. Preuss, P. J. Withers, and S. Bray. Importance of crystal orientation in linear friction joining of single crystal to polycrystalline nickel-based superalloys. *Materials Science and Engineering A*, 491(1-2):446–453, 2008.

[55] S. K. Kiseleva, B. O. Bolshakov, I.V. Alexandrov, and F. F. Musin. Microstructure and Properties of an AA2139 Alloy Welded Joint Produced by Linear Friction Welding. *Journal of Engineering Science and Technology Review*, 8(6):30–32, 2015.

[56] H. H. Koo and W. A. Baeslack. Structure, properties, and fracture of linear friction welded Al-Fe-V-Si alloy 8009. *Materials Characterisation*, 28(2):157, 1992.

[57] L. Appel. Grundlagen der Reibschweißtechnik. In *12. Erfahrungsaustausch Reibschweißen in der SLV München*, 2002.

[58] Wen Ya Li, Tiejun Ma, and Siqian Yang. Microstructure evolution and mechanical properties of linear friction welded Ti-5Al-2Sn-2Zr-4Mo-4Cr (Ti17) titanium alloy joints. *Advanced Engineering Materials*, 12(1-2):35–43, 2010.

[59] E. Dalgaard, P. Wanjara, J. Gholipour, X. Cao, and J. J. Jonas. Linear friction welding of a near-β titanium alloy. *Acta Materialia*, 60(2):770–780, 2012.

[60] Lorella Ceschini, Alessandro Morri, Fabio Rotundo, Tea Sung Jun, and Alexander M Korsunsky. A Study on Similar and Dissimilar Linear Friction Welds of 2024 Al Alloy and 2124Al/SiCP Composite. *Advanced Materials Research*, 89-91:461–466, 2010.

[61] F. Rotundo, L. Ceschini, A. Morri, T. S. Jun, and A. M. Korsunsky. Mechanical and microstructural characterization of 2124Al/25 vol.%SiCpjoints obtained by linear friction welding (LFW). *Composites Part A: Applied Science and Manufacturing*, 41(9):1028–1037, 2010.

[62] A. C. Addison and P. L. Threadgill. Initial studies of linear friction welding of a C-Mn steel. *Welding & Cutting*, (6):364, 2010.

[63] Mica Grujicic, G. Arakere, B. Pandurangan, C. F. Yen, and B. A. Cheeseman. Process modeling of Ti-6Al-4V linear friction welding (LFW). *Journal of Materials Engineering and Performance*, 21(10):2011–2023, 2012.

[64] H Kuroki, K Nezaki, T Wakabayashi, and K Nakamura. Application of linear friction welding technique to aircraft engine parts. *IHI Eng Rev*, 47:40–43, 2014.

[65] G. D. Wen, T. J. Ma, W. Y. Li, J. L. Li, H. Z. Guo, and D. L. Chen. Cyclic deformation behavior of linear friction welded Ti6Al4V joints. *Materials Science and Engineering A*, 597:408–414, 2014.

[66] Mark R. Daymond and Neil W. Bonner. Measurement of strain in a titanium linear friction weld by neutron diffraction. *Physica B: Condensed Matter*, 325:130–137, 2003.

[67] Adrian T DeWald, Daira Legzdina, Bjørn Clausen, Donald W Brown, Thomas A Sisneros, and Michael R Hill. A Comparison of Residual Stress Measurements on a Linear Friction Weld Using the Contour Method and Neutron Diffraction BT - Experimental and Applied Mechanics, Volume 4. pages 183–189, New York, NY, 2013. Springer New York.

[68] M Preuss, J Quinta da Fonseca, A Steuwer, L Wang, P J Withers, and S Bray. Residual Stresses in Linear Friction Welded IMI550. *Journal of Neutron Research*, 12(1-3):165–173, 2004.

[69] M. Karadge, P. Frankel, A. Steuwer, C. Lovell, S. Bray, P. J. Withers, and M. Preuss. Microstructure, texture, local tensile properties and residual stress relief in Ti-6Al-4V linear friction welds. *Proceedings Conference on 'Materials science & technology'*, pages 35–46, 2006.

[70] M. M. Attallah, M. Preuss, and P. J. Withers. Influence of Linear Friction Welding Parameters on the Residual Stress Development in Ti-6246. *Trends in Welding Research*, pages 751–757, 2009.

[71] I. Bhamji. *Development of the linear friction welding process*. Phd, University of Manchester, 2012.

[72] Anthony R. McAndrew, Paul A. Colegrove, Bertrand C. D. Flipo, and Clement Bühr. 3D modelling of Ti-6Al-4V linear friction welds. *Science and Technology of Welding and Joining*, (December):1–9, 2016.

[73] Wenya Li, Jia Guo, Xiawei Yang, Tiejun Ma, and Achilleas Vairis. The effect of micro-swinging on joint formation in linear friction welding. *Journal of Engineering Science and Technology Review*, 7(5):55–58, 2014.

[74] A M Yamileva, R K Gazizov, and A Vairis. Computer modelling of the effect of clamping in linear friction welding. *Journal of Engineering Science and Technology Review*, 8(Specialissue6):65–68, 2015.

[75] Wenya Li, Jia Guo, Tiejun Ma, and Achilles Vairis. Numerical modeling of linear friction welding: a literature review. *China Welding*, 23(4):1–7, 2015.

[76] A Francis and R E Craine. On a model for frictioning stage in friction welding of thin tubes. *International Journal of Heat and Mass Transfer*, 28(9):1747–1755, 1985.

[77] H. S. Carslaw and J. C. Jaeger. *Conduction of Heat in Solids*. Oxford University Press, Oxford, 2 edition, 1959.

[78] G. D. Wen, T. J. Ma, W. Y. Li, X. Li, J. L. Li, T. Chen, R. Wen, J. Niu, and H. Z. Guo. Mathematical modelling of joint temperature during linear friction welding of dissimilar Ti-6.5Al-3.5Mo-1.5Zr-0.3Si and Ti-5Al-2Sn-2Zr-4Mo-4Cr alloys. *Journal of Engineering Science and Technology Review*, 5(3):35–38, 2012.

[79] O T Midling and Ø Grong. A process model for friction welding of Al-Mg-Si alloys and Al-SiC metal matrix composites-I. HAZ temperature and strain rate distribution. *Acta Metallurgica et Materialia*, 42(5):1595–1609, 1994.

[80] R. Turner, J. C. Gebelin, R. M. Ward, and R. C. Reed. Linear friction welding of Ti-6Al-4V: Modelling and validation. *Acta Materialia*, 59(10):3792–3803, 2011.

[81] Anthony R. McAndrew, Paul A. Colegrove, Adrian C. Addison, Bertrand C.D. Flipo, Michael J. Russell, and Lucie A. Lee. Modelling of the workpiece geometry effects on Ti-6Al-4V linear friction welds. *Materials and Design*, 87:1087–1099, 2015.

[82] T J Ma, B Zhong, W-Y Li, Y Zhang, S Q Yang, and C L Yang. On microstructure and mechanical properties of linear friction welded dissimilar Ti-6Al-4V and Ti-6.5Al-3.5Mo-1.5Zr-0.3Si joint. *Science and Technology of Welding and Joining*, 17(1):9–12, 2012.

[83] Libin Yang. Modelling of the Inertia Welding of Inconel 718. *Department of Metallurgy and Materials*, (January):160, 2010.

[84] L. E. Lindgren. Numerical modelling of welding. *Computer Methods in Applied Mechanics and Engineering*, 195(48-49):6710–6736, 2006.

[85] J N Reddy and J N Reddy. *An Introduction to the Finite Element Method*. Asia Higher Education Engineering/Computer Science Mechanical Engineering. McGraw-Hill, 2006.

[86] F Schröder, R M Ward, A R Walpole, R P Turner, M M Attallah, J Gebelin, and R C Reed. Linear friction welding of Ti6Al4V: experiments and modelling. *Materials Science and Technology*, 31(3):372–384, 2015.

[87] H. Wu, Y. Chen, D. Strong, and P. Prangnell. Stationary Shoulder FSW for Joining High Strength Aluminum Alloys. *Journal of Materials Processing Technology*, 221:187–196, 2015.

[88] W. Y. Li, S. X. Shi, F. F. Wang, T. J. Ma, J. L. Li, D. L. Gao, and A. Vairis. Heat reflux in flash and its effect on joint temperature history during linear friction welding of steel. *International Journal of Thermal Sciences*, 67:192–199, 2013.

[89] L A Lee, A R McAndrew, C Buhr, K A Beamish, and P A Colegrove. 2D linear friction weld modelling of a Ti-6Al-4V T-joint. *Journal of Engineering Science and Technology Review*, 8(Specialissue6):44–48, 2015.

[90] M. Grujicic, R. Yavari, J. S. Snipes, S. Ramaswami, C. F. Yen, and B. A. Cheeseman. Linear friction welding process model for carpenter custom 465 precipitation-hardened martensitic stainless steel. *Journal of Materials Engineering and Performance*, 23(6):2182–2198, 2014.

[91] X. Song, M. Xie, F. Hofmann, T.S. Jun, T. Connolley, C. Reinhard, R.C. Atwood, L. Connor, M. Drakopoulos, S. Harding, and A.M. Korsunsky. Residual stresses in Linear Friction Welding of aluminium alloys. *Materials & Design*, 50:360–369, 2013.

[92] Clement Bühr, Paul A. Colegrove, and Anthony R. McAndrew. An Efficient Numerical Modelling Approach to Predict Residual Stresses in Ti-6Al-4V Linear Friction Welds. *10th International Conference on Trends in Welding Research*, (October 2016):Article in Press, 2016.

[93] R. Nikiforov, A Medvedev, E Tarasenko, and Vairis A. Numerical Simulation of Residual Stresses in Linear Friction Welded Joints. *Journal of Engineering Science and Technology Review*, 8(6):49–53, 2015.

[94] Clément Bühr, Bilal Ahmad, Paul A Colegrove, Anthony R Mcandrew, Hua Guo, and Xiang Zhang. Prediction of residual stress within linear friction welds using a computationally ef fi cient modelling approach. *Materials & Design*, 139:222–233, 2018.

[95] Wenya Li, Feifan Wang, Shanxiang Shi, and Tiejun Ma. Numerical simulation of linear friction welding based on ABAQUS environment: Challenges and perspectives. *Journal of Materials Engineering and Performance*, 23(2):384–390, 2014.

[96] Xiao Yu Wu. Finite Element Simulation of Linear Friction Welding. *Advanced Materials Research*, 411:126–129, 2012.

[97] Gianluca Buffa, Davide Campanella, Sergio Pellegrino, and Livan Fratini. Weld quality prediction in linear friction welding of AA6082-T6 through an integrated numerical tool. *Journal of Materials Processing Technology*, 231:389–396, 2016.

[98] J. Sorina-Müller, M. Rettenmayr, D. Schneefeld, O. Roder, and W. Fried. FEM simulation of the linear friction welding of titanium alloys. *Computational Materials Science*, 48(4):749–758, 2010.

[99] Wenya Li, Feifan Wang, Shanxiang Shi, Tiejun Ma, Jinglong Li, and Achilleas Vairis. 3D Finite Element Analysis of the Effect of Process Parameters on Linear Friction Welding of Mild Steel. *Journal of Materials Engineering and Performance*, 23(11):4010–4018, 2014.

[100] Anthony R. McAndrew. 2D Linear Friction Weld Modelling of a Ti-6Al- J estr. (September 2015):4–9, 2016.

[101] Xiawei Yang, Wenya Li, Jinglong Li, Bo Xiao, Tiejun Ma, Zhe Huang, and Jia Guo. Finite element modeling of the linear friction welding of GH4169 superalloy. *Materials and Design*, 87:215–230, 2015.

[102] Alexander Bikmeyev. On the visualization of joint formation during linear friction welding J estr. (February), 2016.

[103] A M Yamileva, A Y Medvedev, I S Nasibullayev, A S Selivanov, R K Gazizov, and A Vairis. A two-parameter 2D-model of the elastic stage of linear friction welding using ANSYS mechanical finite element analysis programme. *Journal of Engineering Science and Technology Review*, 5(3):6–9, 2012.

[104] S K Kiselyeva, A M Yamileva, M V Karavaeva, I S Nasibullayev, V M Bychkov, A Y Medvedev, A V Supov, F F Musin, I V Alexandrov, and V V Latysh. Computer modelling of linear friction welding based on the joint microstructure. *Journal of Engineering Science and Technology Review*, 5(3):44–47, 2012.

[105] E. Ceretti, L. Fratini, C. Giardini, and D. La Spisa. Numerical modelling of the linear friction welding process. *International Journal of Material Forming*, 3(SUPPL. 1):1015–1018, 2010.

[106] R Hill, E H Lee, and S J Tupper. The Theory of Combined Plastic and Elastic Deformation with Particular Reference to a Thick Tube under Internal Pressure. *Proceedings of the Royal Society of London. Series A, Mathematical and Physical Sciences*, 191(1026):278–303, 1947.

[107] Guy Banwell, Stefan Mohr, Steve Rothberg, and Jon Roberts. Using experimental modal analysis to validate a finite element model of a tennis racket. *Procedia Engineering*, 34(0):688–693, 2012.

[108] MTI. Linear Friction Welding.

[109] Toshio Kuroda, Kenji Ikeuchi, and Hyuma Ikeda. Flash butt resistance welding for duplex stainless steels. *Vacuum*, 80(11-12):1331–1335, 2006.

[110] Fucheng Zhang, Bo Lv, Baitao Hu, and Yanguo Li. Flash butt welding of high manganese steel crossing and carbon steel rail. *Materials Science and Engineering A*, 454-455:288–292, 2007.

[111] Cemil Çetinkaya and Ugur Arabaci. Flash butt welding application on 16MnCr5 chain steel and investigations of mechanical properties. *Materials and Design*, 27(10):1187–1195, 2006.

[112] Pewag. pewag hero Reibschweißkette.

[113] K. Mucic. *Lineares Reibschweißen in der Kettenfertigung*. Phd, Technische Universität Graz, 2017.

[114] Johannes Löffelmann. *Systematische Untersuchung der Schweißparameter beim linearen Reibschweißen*. PhD thesis, Technische Universität Graz, 2012.

[115] F. Fuchs, P. Tasic, and N. Enzinger. Innovatives Schweißverfahren für hochfeste Hebe- und Förderketten. *Schweiss- & Prüftechnik*, Sodnerband:15–17, 2009.

[116] H. Cerjak, A. Pengg, and F. Franz. Method for producing welded round and profile chains, chain links for a round or profile chain and round or profile chain made of chain links of said kind, dec 2008.

[117] Jose Romero Lopera. Numerical simulation of linear friction welded chain links. (May), 2012.

[118] M. M A Khan, L. Romoli, M. Fiaschi, G. Dini, and F. Sarri. Experimental design approach to the process parameter optimization for laser welding of martensitic stainless steels in a constrained overlap configuration. *Optics and Laser Technology*, 43(1):158–172, 2011.

[119] Z. Gao, J. T. Niu, F. Krumphals, N. Enzinger, S. Mitsche, and C. Sommitsch. FE modelling of microstructure evolution during friction stir spot welding in AA6082-T6. *Welding in the World*, 57(6):895–902, 2013.

[120] H Pashazadeh, J Teimournezhad, and a Masoumi. Numerical investigation on the mechanical, thermal, metallurgical and material flow characteristics in friction stir welding of copper sheets with experimental verification. *Materials & Design*, 55(March):619–632, 2014.

[121] H. Schmidt and J. Hattel. A local model for the thermomechanical conditions in friction stir welding. *Modelling and Simulation in Materials Science and Engineering*, 13(1):77–93, 2005.

[122] J.S. Sun, K.H. Lee, and H.P. Lee. Comparison of implicit and explicit finite element methods for dynamic problems. *Journal of Materials Processing Technology*, 105(1-2):110–118, 2000.

[123] T J R Hughes. *The Finite Element Method: Linear Static and Dynamic Finite Element Analysis (Dover Civil and Mechanical Engineering)*. Dover Publications, aug 2000.

[124] SFTC. DEFORM v11.1 SP1 System Documentation.

[125] S.I. Oh. Finite element analysis of met al forming processes with arbitra rily shaped dies. *International Journal of Mechanical Sciences*, 24(8):479–493, 1982.

[126] Shiro Kobayashi, Soo-Ik Oh, and Taylan Altan. Metal forming and the finite element method , 1989.

[127] R. Hill. New horizons in the mechanics of solids. *Journal of the Mechanics and Physics of Solids*, 5:66–74, 1956.

[128] Erwin Kreyszig. *Advanced Engineering Mathematics: Maple Computer Guide*. John Wiley & Sons, Inc., New York, NY, USA, 8th edition, 2000.

[129] BÖHLER. Heat Treatable Steel Böhler V145. Technical report.

[130] S.-H. Cho and J.-W. Kim. Analysis of residual stress in carbon steel weldment incorporating phase transformations. *Science and Technology of Welding and Joining*, 7(4):212–216, 2002.

[131] Dean Deng. FEM prediction of welding residual stress and distortion in carbon steel considering phase transformation effects. *Materials and Design*, 30(2):359–366, 2009.

[132] Michael C. Weinberg, Dunbar P. Birnie, and Vitaly A. Shneidman. Crystallization kinetics and the JMAK equation. *Journal of Non-Crystalline Solids*, 219:89–99, 1997.

[133] J. Lopera, K. Mucic, F. Fuchs, and N. Enzinger. Linear friction welding of high strength chains: modelling and validation. *Mathematical Modelling of Weld Phenomena*, 10:203–218, 2013.

[134] Reza Karimi, Ali Akbar Akhtari, and Omid Seyedashraf. Implementation of the skyline algorithm in finite-element computations of Saint-Venant equations. 2:63–67, 2014.

[135] Jonathan R Shewchuk. An Introduction to the Conjugate Gradient Method Without the Agonizing Pain. Technical report, Pittsburgh, PA, USA, 1994.

[136] ASTM E384-11. Standard Test Method for Knoop and Vickers Hardness of Materials Specimen. In: American Society for Testing and Materials; 2011. Technical report.

[137] R. Von Mises. Mechanik der festen Körper im plastisch deformablen Zustand. *Nachrichten von der Gesellschaft der Wissenschaften zu Göttingen*, Mathematis(4):582–592, 1913.

[138] W D Callister. *Fundamentals of Materials Science and Engineering: An Integrated Approach*. John Wiley & Sons, 2005.

[139] J F Shackelford. *Introduction to Materials Science for Engineers*. Prentice Hall, 2000.

[140] T H Courtney. *Mechanical Behavior of Materials*. McGraw-Hill series in materials science and engineering. McGraw Hill Custom Pub., 2000.

[141] M F Ashby, H Shercliff, and D Cebon. *Materials: Engineering, Science, Processing and Design*. Butterworth-Heinemann. Butterworth-Heinemann, 2013.

[142] H. Hencky. Über die Form des Elastizitätsgesetzes bei ideal elastischen Stoffen. *Zeitschrift für technische Physik*, 9:215–220, 1929.

[143] Jingui Yu, Qiaoxin Zhang, and Zhufeng Yue. Tensile mechanical properties of Ni3Al nanowires at intermediate temperature. *RSC Advances*, 4(40):20789–20796, 2014.

[144] A. Arora, Z. Zhang, A. De, and T. DebRoy. Strains and strain rates during friction stir welding. *Scripta Materialia*, 61(9):863–866, 2009.

[145] M. Maalekian, E. Kozeschnik, H. P. Brantner, and H. Cerjak. Finite element modeling of orbital friction welding of eutectoid steel bars. *Metallurgical and Materials Transactions A*, pages 1–9, 2008.

[146] M. Maalekian and H. Cerjak. Modelling the orbital friction welding of pearlitic steel bars. *ASM Proceedings of the International Conference: Trends in Welding Research*, (October 2014):736–741, 2009.

[147] P Harris and B L Smith. Factorial techniques for weld quality prediction. *Metal Construction*, 15(11):661–666, 1983.

[148] Livan Fratini, Gianluca Buffa, Davide Campanella, and Dario La Spisa. Investigations on the linear friction welding process through numerical simulations and experiments. *Materials & Design*, 40:285–291, 2012.

[149] Shude Ji, Yue Wang, Jianguang Liu, Xiangchen Meng, Jun Tao, and Tiancang Zhang. Effects of welding parameters on material flow behavior during linear friction welding of Ti6Al4V titanium alloy by numerical investigation. *International Journal of Advanced Manufacturing Technology*, 82(5-8):927–938, 2016.

[150] Douglas C Montgomery. *Design and Analysis of Experiments*, volume 2. John Wiley & Sons, 2012.

[151] M. M D Zulkali, A. L. Ahmad, and N. H. Norulakmal. Oryza sativa L. husk as heavy metal adsorbent: Optimization with lead as model solution. *Bioresource Technology*, 97(1):21–25, 2006.

[152] Rafael Colás. A model for the hot deformation of low-carbon steel. *Journal of Materials Processing Technology*, 62(1-3):180–184, 1996.

List of publications

1. P. S. Effertz, F. Fuchs, and N. Enzinger. Modelling the ash formation of linear friction welded 30CrNiMo8 high strength steel chains. *International Journal of Advanced Manufacturing Technology*, 2017.

2. Pedro Effertz, Franz Fuchs, and Norbert Enzinger. 3D Modelling of Flash Formation in Linear Friction Welded 30CrNiMo8 Steel Chain. *Metals*, 7(10):449, 2017.

3. D.G. Nunes, P.S. Effertz, L. Quintino, I. Pires, F. Fuchs, and N. Enzinger. Residual stresses in 18CrNiMo7-6 linear friction welded high strength steel chains. *International Journal of Advanced Manufacturing Technology*, 2018.

4. P. S. Effertz, F. Fuchs, and N. Enzinger. The influence of process parameters in linear friction welded 30CrNiMo8 small cross-section: a modelling approach. *Science and Technology of Welding and Joining*, 0(0):19, 2018.

5. P. S. Effertz, F. Fuchs, and N. Enzinger. Advances in numerical modelling of linear friction welded high strength steel chains. (Seggau Conference, will be updated)

Chapter 8

Annex

A. Thermo-mechanical properties of 30CrNiMo8

This section gives an overview of the thermo-mechanical properties implemented in DEFORM FEA. Hence, the flow stress curves are illustrated for a range of temperatures between $25°C$ and $1400°C$. For temperatures above 500°C, the shape of the curves start to change due to softening effect, being more pronounced when the temperatures go beyond austenization.

Further thermo-mechanical properties are included, such as Young modulus, Poisson ratio, thermal conductivity, specific density, specific heat, and specific heat capacity; as a function of temperature and all of which calculated using JMatPro.

i. Flow stresses

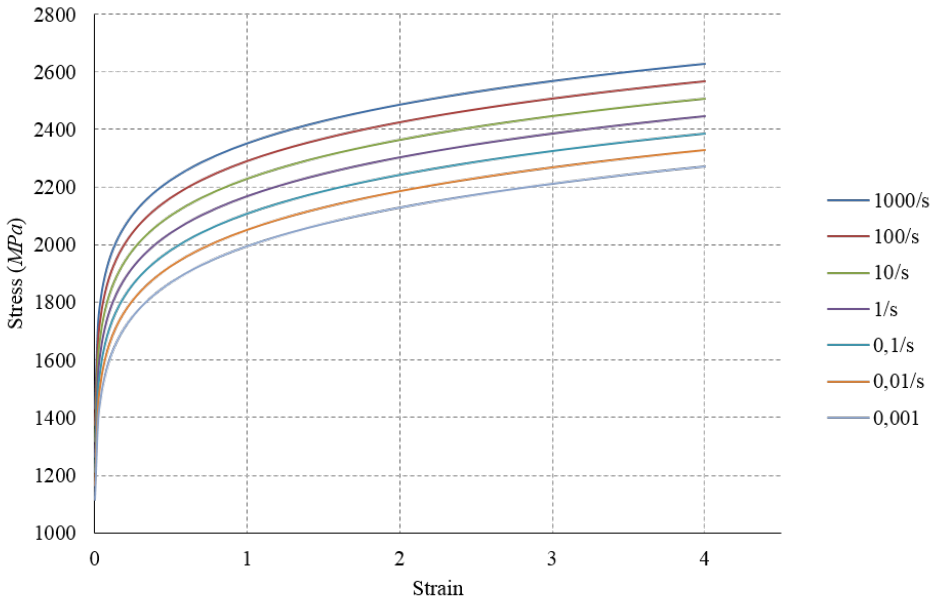

Figure 8.1: Flow stress-strain curves for 30CrNiMo8 at 25°C.

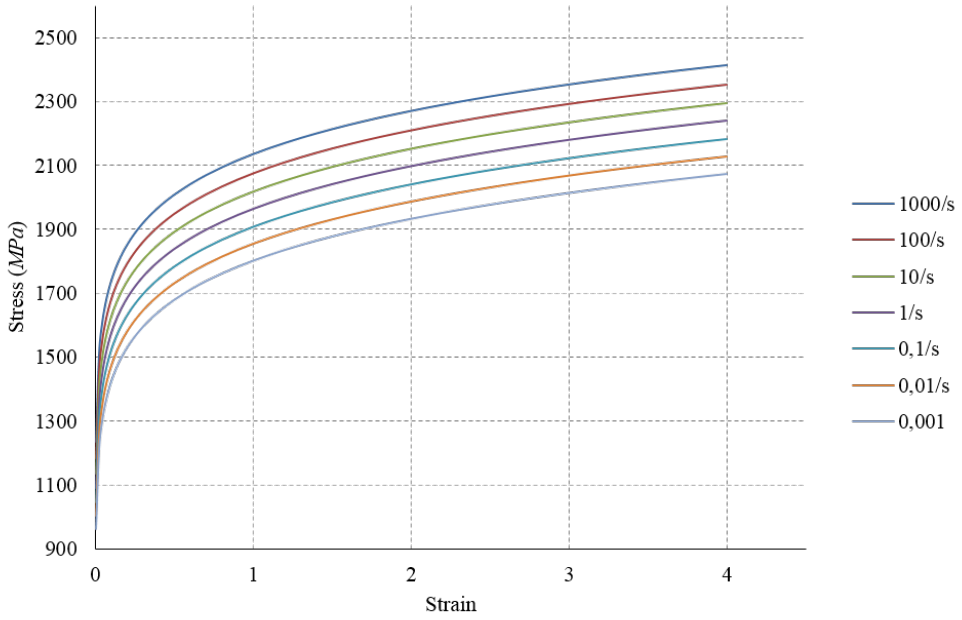

Figure 8.2: Flow stress-strain curves for 30CrNiMo8 at 100°C.

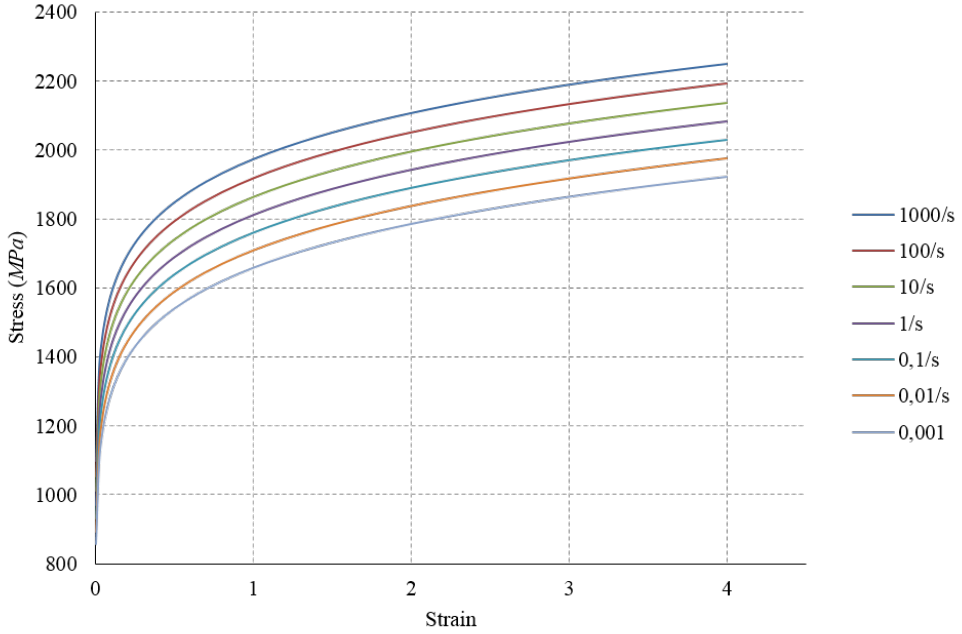

Figure 8.3: Flow stress-strain curves for 30CrNiMo8 at 200°C.

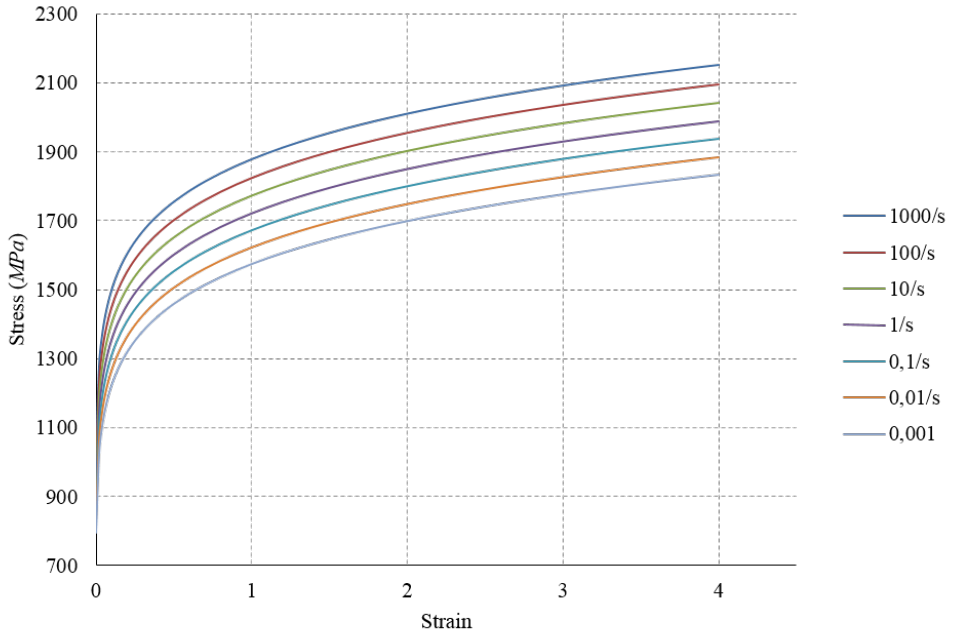

Figure 8.4: Flow stress-strain curves for 30CrNiMo8 at 300°C.

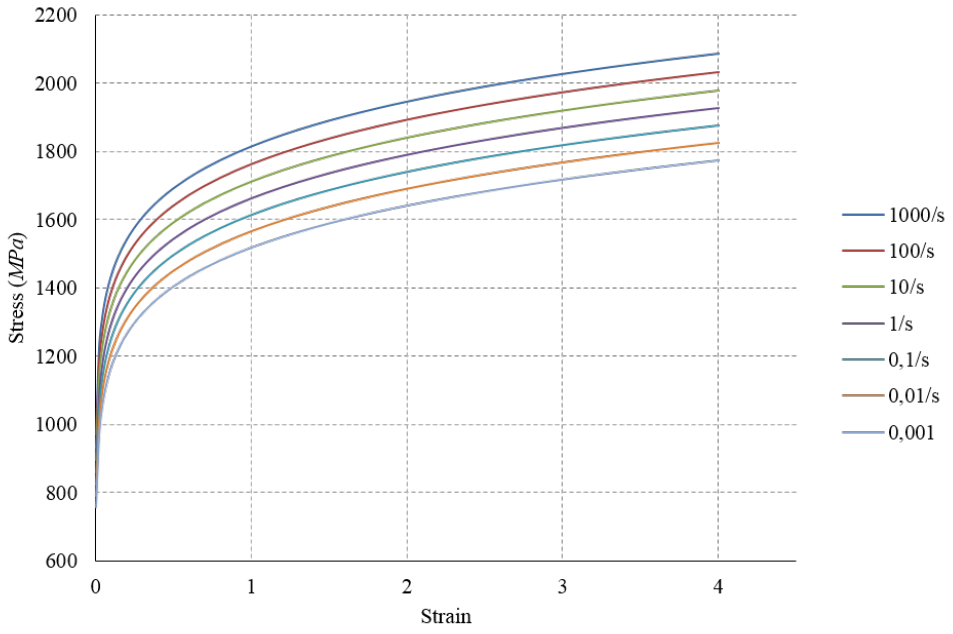

Figure 8.5: Flow stress-strain curves for 30CrNiMo8 at 400°C.

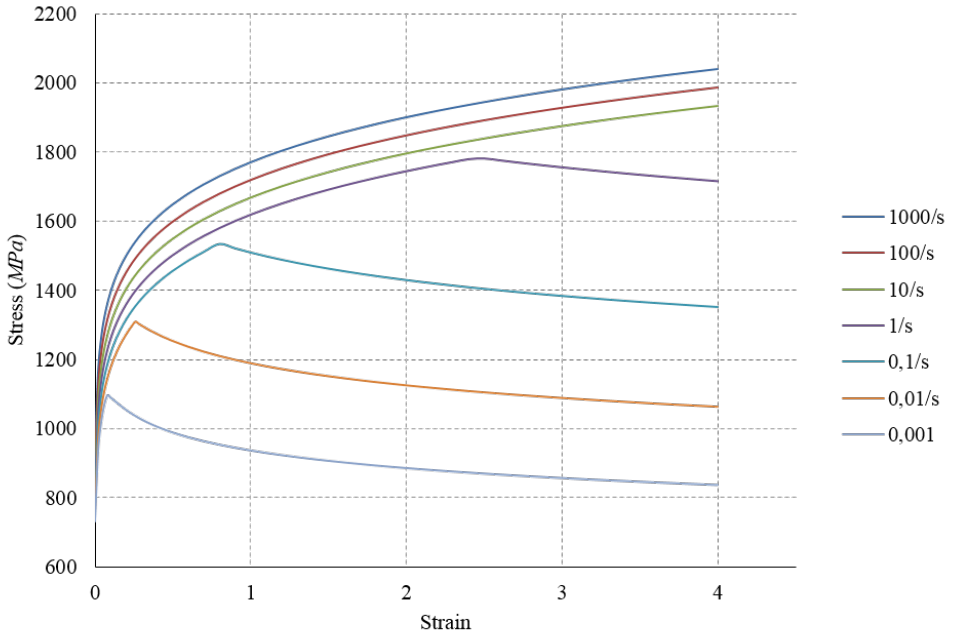

Figure 8.6: Flow stress-strain curves for 30CrNiMo8 at 500°C.

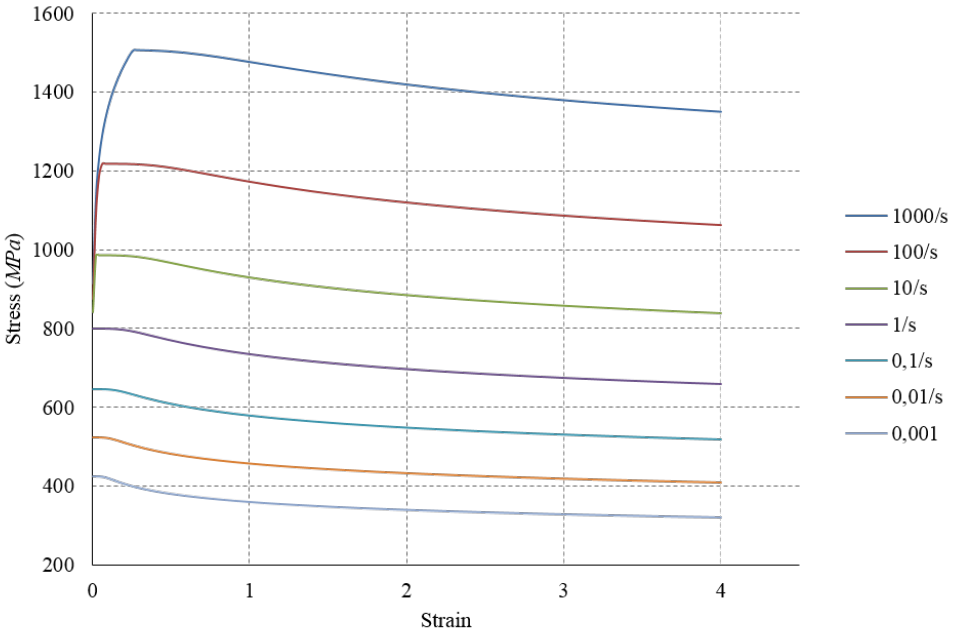

Figure 8.7: Flow stress-strain curves for 30CrNiMo8 at 600°C.

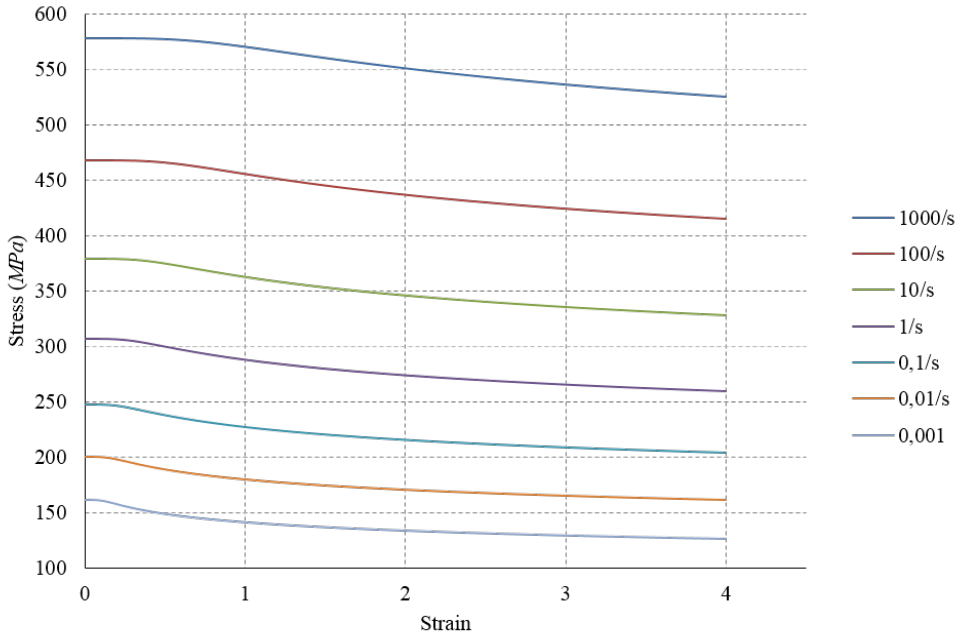

Figure 8.8: Flow stress-strain curves for 30CrNiMo8 at 700°C.

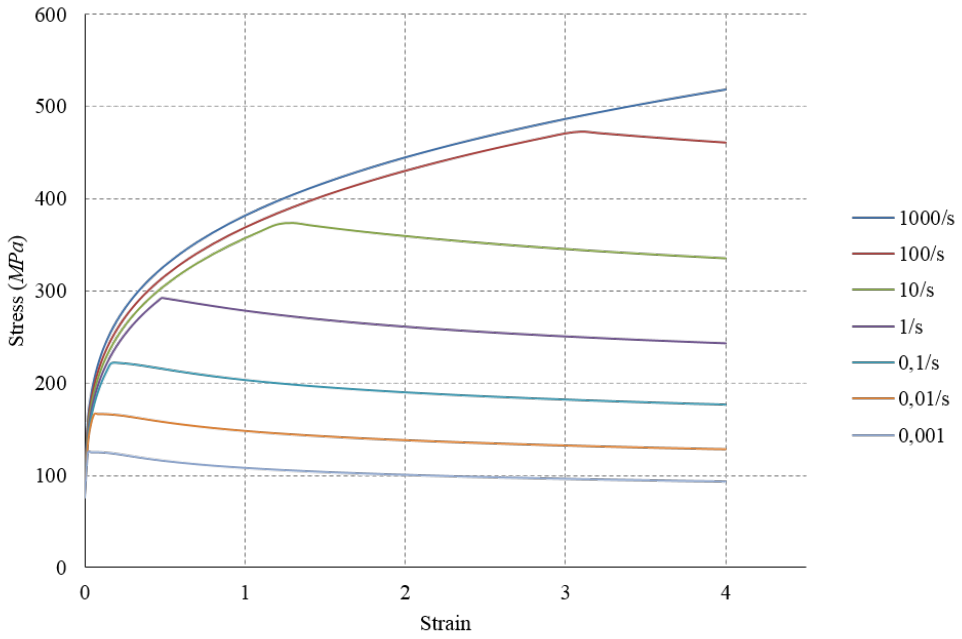

Figure 8.9: Flow stress-strain curves for 30CrNiMo8 at 800°C.

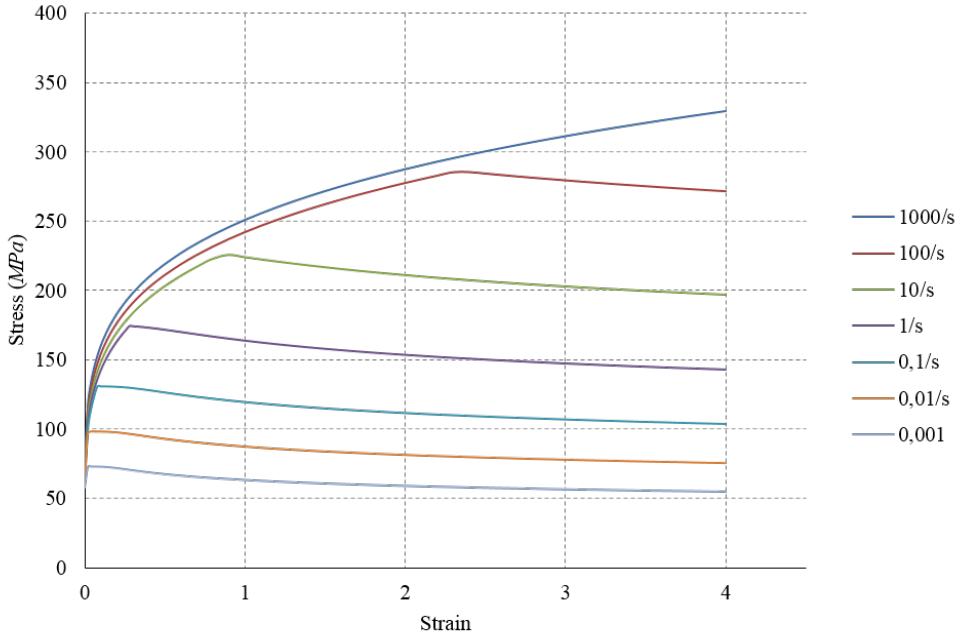

Figure 8.10: Flow stress-strain curves for 30CrNiMo8 at 900°C.

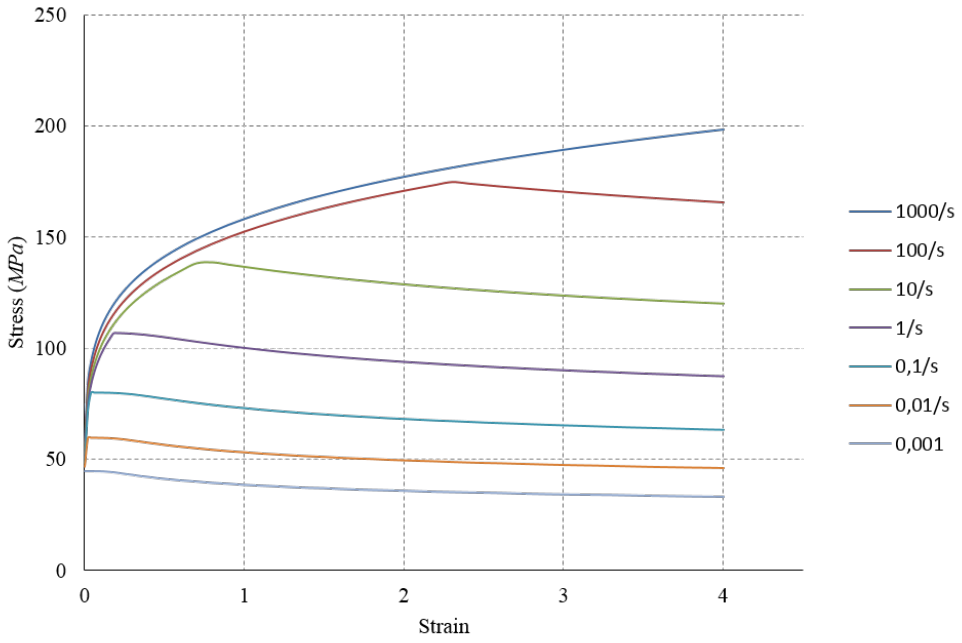

Figure 8.11: Flow stress-strain curves for 30CrNiMo8 at 1000°C.

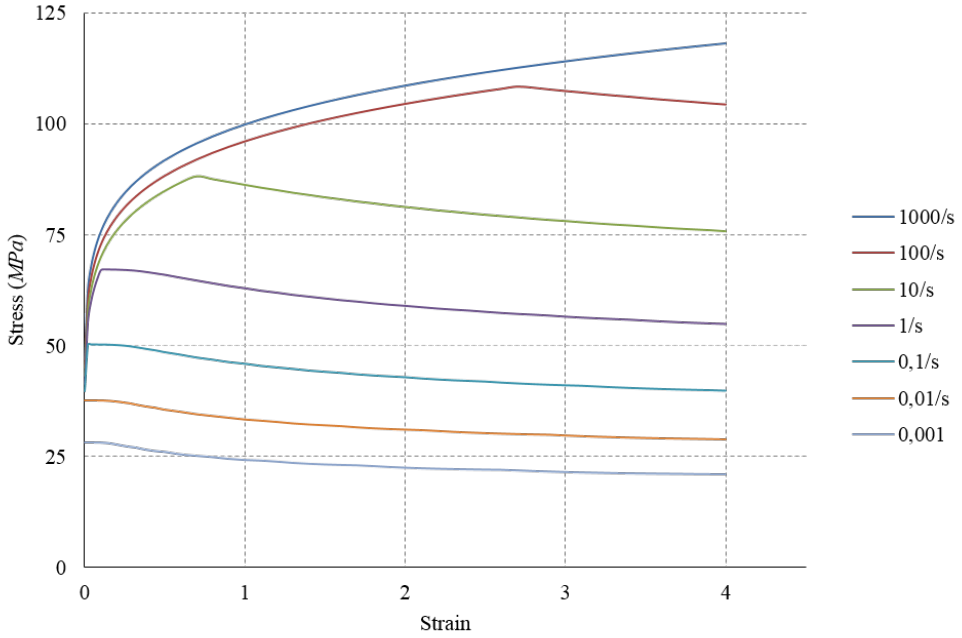

Figure 8.12: Flow stress-strain curves for 30CrNiMo8 at 1100°C.

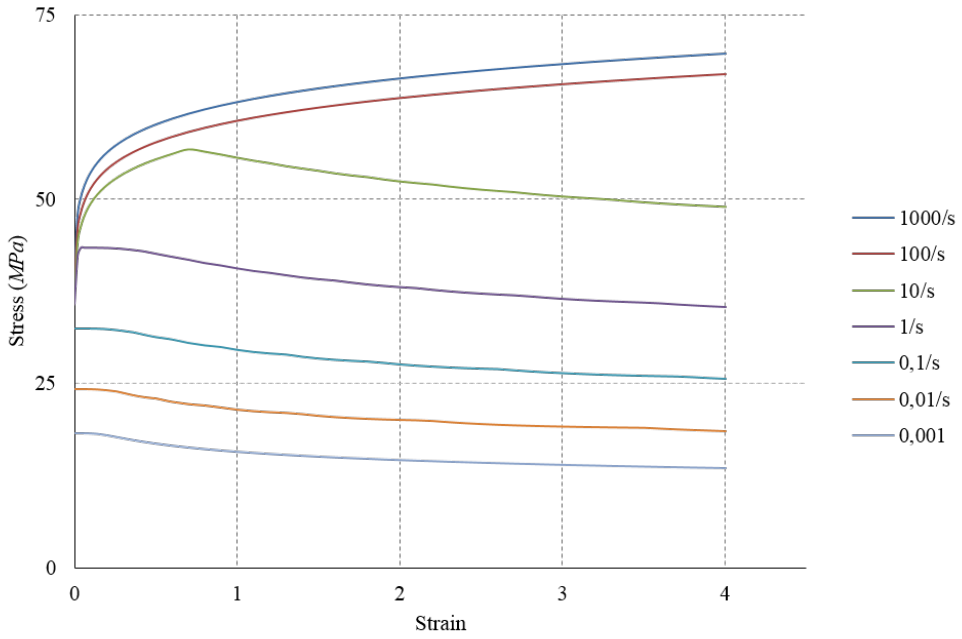

Figure 8.13: Flow stress-strain curves for 30CrNiMo8 at 1200°C.

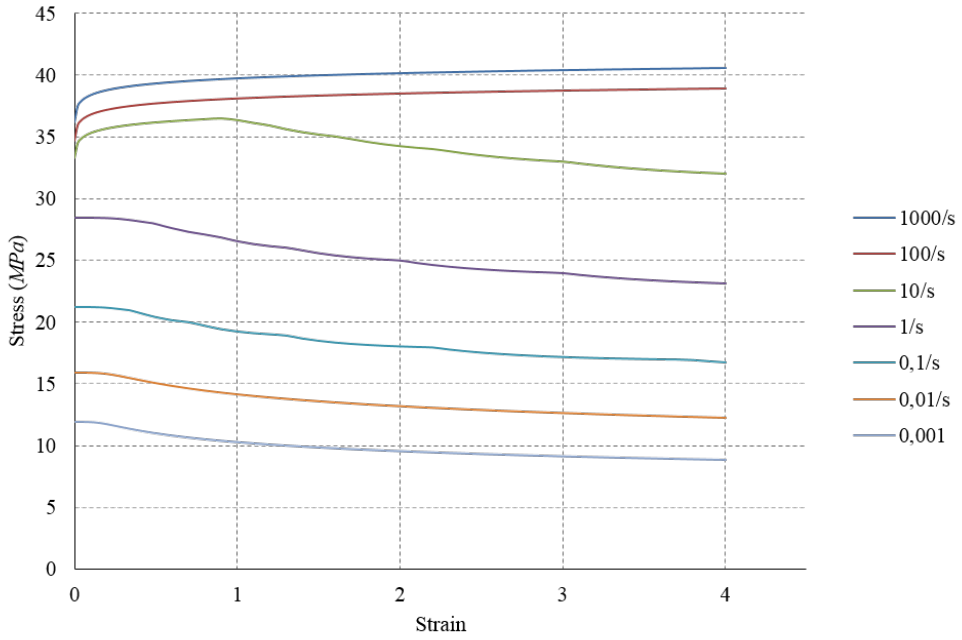

Figure 8.14: Flow stress-strain curves for 30CrNiMo8 at 1300°C.

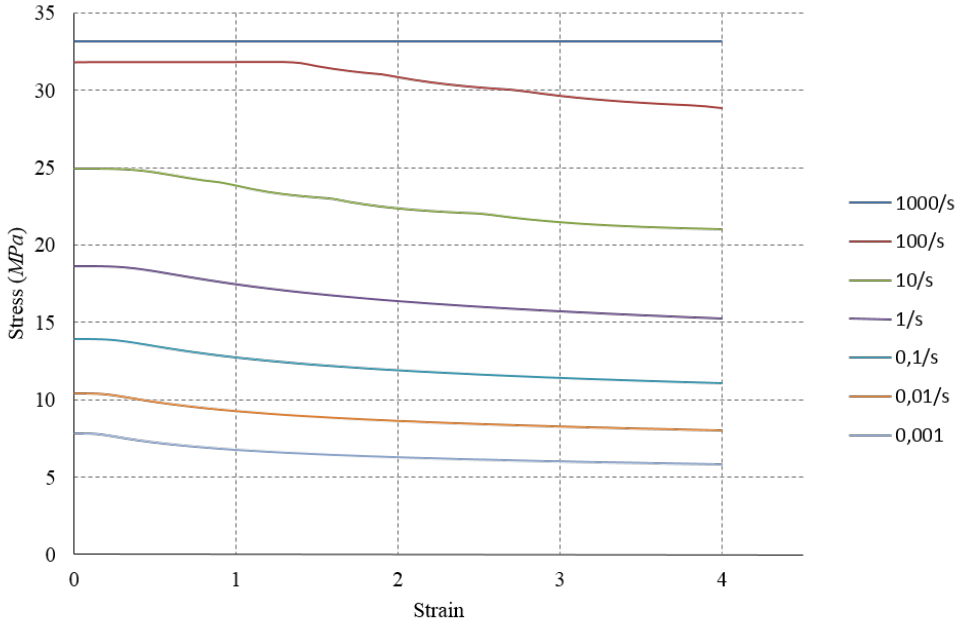

Figure 8.15: Flow stress-strain curves for 30CrNiMo8 at 1400°C.

ii. Young modulus

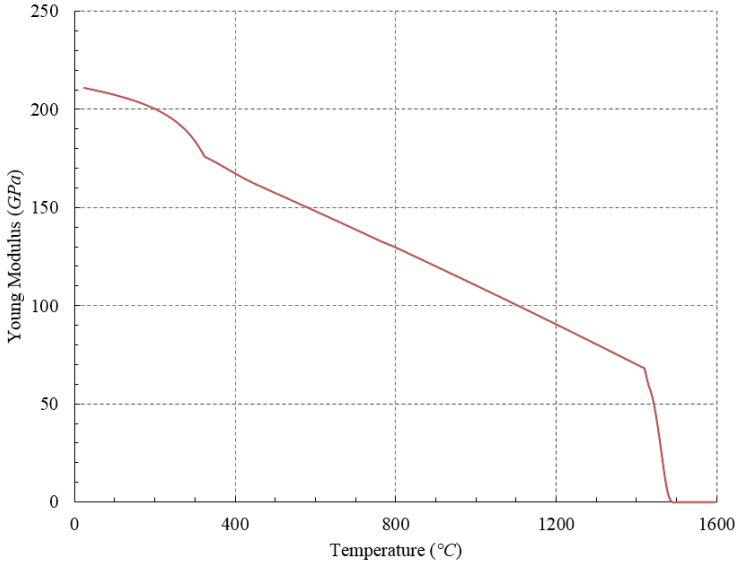

Figure 8.16: Young modulus as a function of temperature.

iii. Poisson ratio

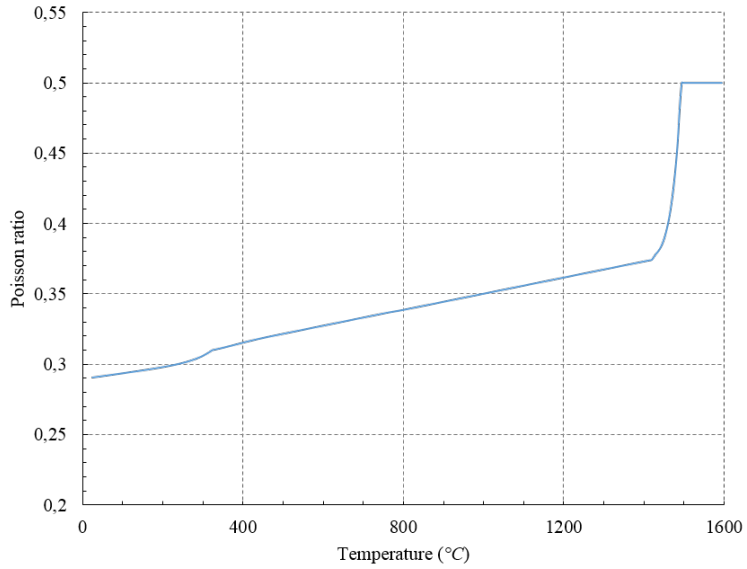

Figure 8.17: Poisson ratio as a function of temperature.

iv. Thermal conductivity

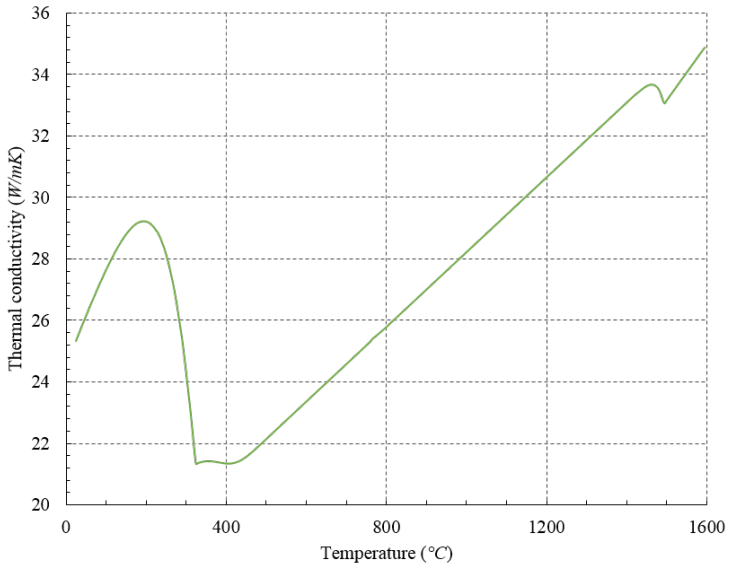

Figure 8.18: Thermal conductivity as a function of temperature.

v. Density

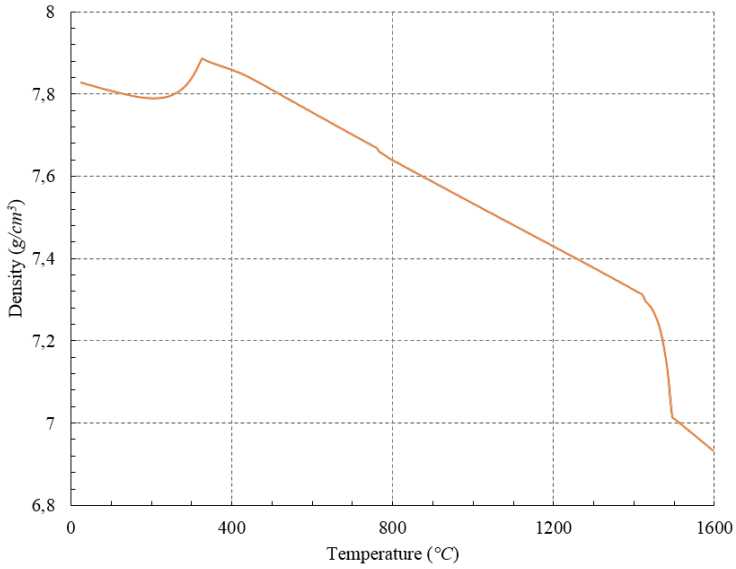

Figure 8.19: Density as a function of temperature

vi. Specific heat

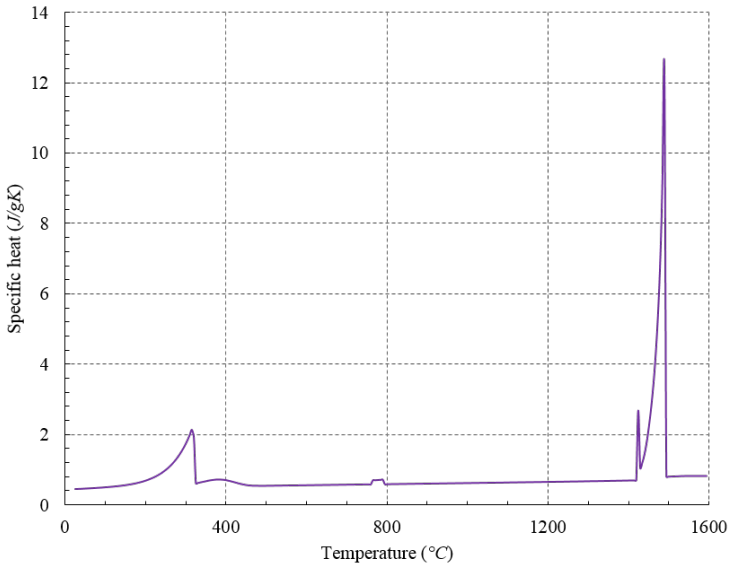

Figure 8.20: Specific heat as a function of temperature

vi. Specific heat

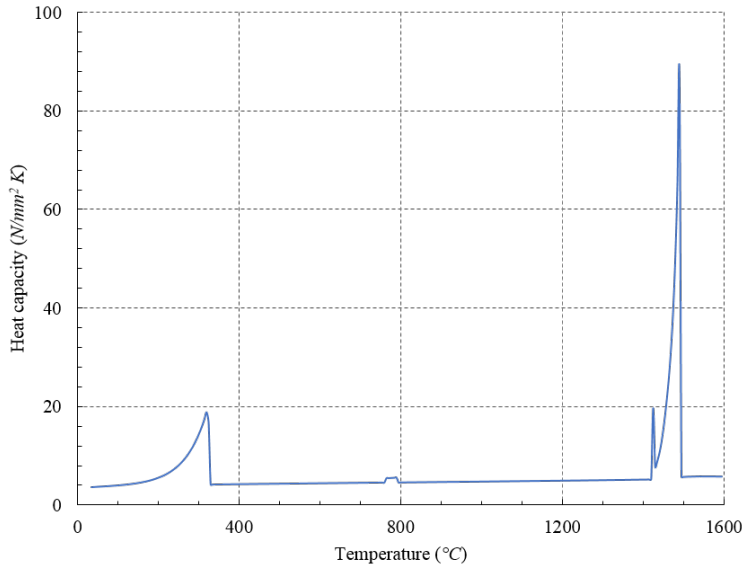

Figure 8.21: Heat capacity as a function of temperature, including transformation enthalpy